4-2-2018

DEVELOPING NANOPORE ELECTROMECHANICAL SENSORS WITH TRANSVERSE ELECTRODES FOR THE STUDY OF NANOPARTICLES/BIOMOLECULES

Mohammadsadegh Beheshti
Louisiana State University and Agricultural and Mechanical College

DEVELOPING NANOPORE ELECTROMECHANICAL SENSORS WITH TRANSVERSE ELECTRODES FOR THE STUDY OF NANOPARTICLES/BIOMOLECULES

A Dissertation

Submitted to the Graduate Faculty of the
Louisiana State University and
Department of Mechanical and Industrial Engineering
in partial fulfillment of the
requirements for the degree of
Doctor of Philosophy

in

The Department of Mechanical & Industrial Engineering

by
Mohammadsadegh Beheshti
B.S., Iran University of Science and Technology, 2009
M.S., Iran University of Science and Technology, 2011
May 2018

Table of Contents

Tables

Figures

Abstract

This study concerns development of a technology of utilizing metallic nanowires for a sensing element in nanofluidic single molecular (nanoparticle) sensors formed in plastic substrates to detect the translocation of single molecules through the nanochannel. We aimed to develop nanofluidic single molecular sensors in plastic substrates due to their scalability towards high through and low cost manufacturing for point-of-care applications. Despite significant research efforts recently on the technologies and applications of nanowires, using individual nanowires as electric sensing element in nanofluidic bioanalytic devices has not been realized yet. This dissertation work tackles several technical challenges involved in this development, which include reduction of nanowire agglomerates in the deposition of individual nanowires on a substrate, large scale alignment/assembly of metallic nanowires, placement of single nanowires on microelectrodes, characterization of electrical conductance of single nanowire, bonding of a cover plate to a substrate with patterned microelectrodes and nanowire electrodes. Overcoming the abovementioned challenges, we finally demonstrated a nanofluidic sensor with an in-plane nanowire electrode in poly(methyl methacrylate) substrates for sensing single biomolecules.

In the first part of this study, we developed the processes for separation and large-scale assembly of individual NiFeCo nanowires grown using an electrodeposition process inside a porous alumina template. A method to fabricate microelectrode patterns on plastic substrates using flexible stencil masks was developed. We studied electrical and magnetic properties of new composite core-shell nanowires by measuring the electrical transport through individual nanowires. The core-shell nanowires were composed of a mechanically stable FeNiCo core and an ultrathin shell of a highly conductive Au gold (FeNiCo-Au nanowires).

In the second part of this study, we simulated the effects of the nanopore geometry on the current drop signal of the translocation through a nanopore via finite element method using

COMSOL. Using the above techniques, we developed for the fabrication and alignment of the microelectrodes and nanowires, we studied the optimum conditions to integrate the transverse nanoelectrode with the nanochannel on plastic substrates. The main challenge was to find the conditions to embed the micro-/nanoelectrodes into the nanochannel substrate as well as the nanochannel cover sheet.

Chapter 1. Introduction

1.1. General introduction

Since the early demonstration of a nanopore by Church group in 1995 to detect individual polymer molecules [1], nanopore sensors have been developed as powerful tools to interrogate signals from single molecules and particles with high-throughput [2]. Nanopore sensors can be fabricated via a combination of established micro and nanomachining techniques and connected to an electronic current measurement system for label free detection of single molecules [3]. The nanopore sensors have been used to study physical properties of DNA [4, 5], RNA [6], protein [7, 8] and single molecules [9, 10]. These studies play a crucial role for various health care purposes such as detecting biomarkers linked to DNA linked to epigenetic diseases [11], detecting disordered proteins to study multicellular functions [12] and detecting the DNA base pairs composition for the study of diseases [13]. In this dissertation, the term "nanoparticle" is used to refer to any single molecules including DNA, RNA, and protein as well as traditional nanoparticles such as Au and Ag nanoparticles. The basic operation of a nanopore sensor is to drive individual molecules through the nanopore by applying a voltage to the electrolytic fluid chambers on either side of the nanopore and to record variations of ionic current along the nanopore or transverse to the nanopore [14].

Current approaches to enhance the nanopore single molecular detection accuracy include using the biological nanopores, changing the nanopore material, using ultrathin (< 1 nm) nanopores and nanopores measuring longitudinal and transverse currents. The biological nanopores have small pore dimensions but they are fragile and limited in terms of the number of times they can be used [13]. In terms of the nanopore material, nanopores formed in silicon nitride coated with a lipid bilayer enhances the mechanical and electrical stability of the transient current measurement. Even though they control the aggregation of the molecules entering the nanopore, the large diameter of the coated nanopore and the high molecules

translocation speed make it difficult to detect small molecules [15]. The ultrathin nanopores in MoS_2 or graphite are very powerful tools to increase the signal-to-noise ratio in transient current measurements for single molecular detection. Beside their complicated fabrication process, the high translocation speed through these nanopores, their lack of temporal resolution (the resolution of signal variations versus time) and high electrical noise limit their application in single molecular detection [16].

Contingent on which method is used, nanopore sensors can be divided into two types: nanopore sensors measuring only the longitudinal ionic current and nanopore sensors measuring both the longitudinal [5, 17, 18] and transverse currents [19-21]. The first type sensors only record ionic current flowing through the electrode pair between two sides of the nanopore (longitudinal electrodes) while the second type sensors also record the current flowing through the second pair of electrodes that are formed transverse to the direction of longitudinal electrode pair (transverse electrodes). According to a recent work on the simultaneous transient current measurements of single molecular translocation with the two types of electrodes [22], the transverse ionic current through the transverse electrodes shows an ionic current spike instead of a current decrease in the longitudinal current by the blockage of the nanopore by the nanoparticle. This might be explained by the capacitator behavior of the transverse nanogap electrodes [22]. The ionic currents from the longitudinal and transverse electrodes provided complimentary information on the molecular translocation and thus the ability of simultaneously measuring ionic current with the longitudinal and transverse electrodes would make it easier to differentiate molecules via the transient current peak variations. The main challenges of current available examples of this nanopore type is the difficulty in aligning the active sensing area of the transverse electrodes and nanopore sensing region, the sensitivity of the transverse electrode to the orientation of the molecule, and high speed of translocation through these nanopores [23].

In addition to differentiate molecules via transient peak variations using nanopores, a new sensing mechanism of detecting and differentiating single molecules via measuring time-of-flight (TOF) of the molecular translocation through two in-plane nanopores was introduced. In order to enable measuring the TOF, two or more in-plane nanopores were integrated into a nanochannel flight tube. The first example of this sensor type consisted of two stacked silicon and silicon nitride nanopores separated with a micron size chamber in which the molecules can be deviated from a straight path between the two nanopores. However, the existence of more than one molecule inside the chamber causes overlap issues in reading signals from the second nanopore. These cause errors in the measurement of the TOF using this sensor [24]. Integration of the nanopores with a nanochannel provides the control over the translocation of the nanoparticle [25] and makes it easier to measure the TOF of the nanoparticle between two nanopores. Thus, in the second example the two nanopores were separated via a nanochannel leading the molecules into a straight path between the two pores. However, the wide nanochannel (~1 μm) cause overlap issues while the sensor is unable to discriminate between the signals from each pore [26].

In order to solve the problems of the current nanopore sensors measuring TOFs of molecules, a two nanopore sensor through a nanochannel flight tube has been developed and demonstrated from my group (Prof. Park Laboratory of Mechanical Engineering, Louisiana State University). The nanochannel flight tube between two in-plane nanopores (or double nanopore-nanochannel) allows nanoparticles to travel between the two nanopores under high electric field. The nanoscale electrokinetic behavior of molecules and the interaction between the molecules and the wall of the nanochannel flight tube allow us to differentiate different molecules via the TOF measurement.

A challenge occurring in the development of the TOF nanosensor is the difficulty in identifying paired current transient peaks from the two in-plane nanopores during the

translocation of single molecules. A proposed solution is the use of another in-plane electrode placed between the two in-plane nanopores, which will allow us to apply different voltages and distinguish the origin of the transient current signals between the two pores separately. This allows a clear separation of the signals from each nanopore. Since the nanoelectrode has to reside inside the nanochannel, a zero voltage difference (hence a constant electric field) will be applied to the molecule at the intersection of the nanoelectrode with the nanochannel. While the molecule is traveling inside the nanochannel flight tube, the constant electric field at this location causes the molecule to drift. Consequently, using a micro or macroscale electrodes between the two nanopores would cause a large drift region inside the flight tube and thus a nanoscale electrode is required for this purpose.

On the other side, the integration of a nanoscale electrode into a nanofluidic device is challenging and needs to overcome many technical hurdles. Depending on the fabrication method, the nanowires based nanoelectrodes are divided into directly grown nanowires on the final device and pre-grown nanowire. The current techniques of the first type (e.g. Electron Beam Induces Deposition (EBID) [27]) allow a high controllability over the alignment of the nanowires on the target substrate however these techniques are high cost, not compatible with several fragile substrates (e.g. plastic), and unable to control the properties of the nanowires similar to the ones of pre-grown nanowires. Even though the pre-grown nanowires provide a facile and high throughput nanowire fabrication and enable one to control and change the nanowire properties, they require separation of individual nanowires and placement and alignment of the separated nanowires on desired locations of a substrate [28]. The high volume alignment of the pre-grown nanowires is low cost and compatible with the substrates of different materials but it is unable to place single nanowires (without the presence of other nanowires) on the target [29]. Conversely, the single nanowire alignment techniques provide a precise control over the translational and rotational alignment of the single nanowires. The

main problem of the current available techniques of this type are incompatibility with the fragile (e.g. plastic) substrates, disability to perform the alignment in ambient conditions (require vacuum or liquid medium) and complexity of the methods [30].

This dissertation work develops technologies relevant to utilization of nanowires as the sensing element in nanofluidic devices. Nanowires grown by electrochemical deposition into nanoscale porous templates such as porous alumina and track-etched polycarbonate membrane are mechanically and electrically more stable than the nanowires formed by various metal deposition methods such as sputtering and e-beam evaporation. The technical challenges include reduction of nanowire agglomerates in the deposition of individual nanowires on a substrate, large scale alignment/assembly of metallic nanowires, placement of single nanowires on microelectrodes, characterization of electrical conductance of single nanowire, bonding of a cover plate to a substrate with patterned microelectrodes and nanowire electrodes. Overcoming the abovementioned challenges, we finally demonstrated a nanofluidic sensor with an in-plane nanowire electrode in poly(methyl methacrylate) substrates for sensing single biomolecules.

This work also aims to develop the nanofluidic sensors in plastic substrates, which is predicated by the availability of scalable nanomanufacturing modalities such as nanoimprint lithography and other molding technologies. Polymer based nanopore device has low dielectric loss factor, noise level, fabrication efficiency and size controllability than the silicon-based devices. High rate production of such devices is a key to use of the developed nanosensors for point-of-care and precision medicine applications. Despite the scalability of plastic nanofluidic sensors, the incompatibility of soft plastic materials with many processing tools makes it very difficult to use the nanowires as electrical sensing elements in the plastic device. Developing technologies to use nanowires for plastic substrates also benefit many other applications where nanoscale stable electrodes are required. Examples include flexible electronics and displays.

1.2. Goals and objectives of this study

The primary goal of this study is to develop technologies needed to utilize nanowires as sensing element in a nanochannel-based single molecular sensor formed in polymer substrate. A testbed device designed to achieve the goal was a time-of-flight (TOF) nanosensor. The schematics of this TOF nanosensor is shown in Figure 1.1. A nanochannel flight tube is integrated with two in-plane nanopores and one additional transverse electrode formed between the two in-plane nanopores. We name this new sensor design a "double nanopore-nanochannel sensor." Two sets of longitudinal ionic currents measured between the transverse electrode and the respective inlet and outlet of the nanochannel device provide a TOF for single nanoparticle translocation. We seek to develop a technology to use pre-grown nanowires by a template method as a means of achieving low cost and high throughput manufacturing of the designed sensor structure.

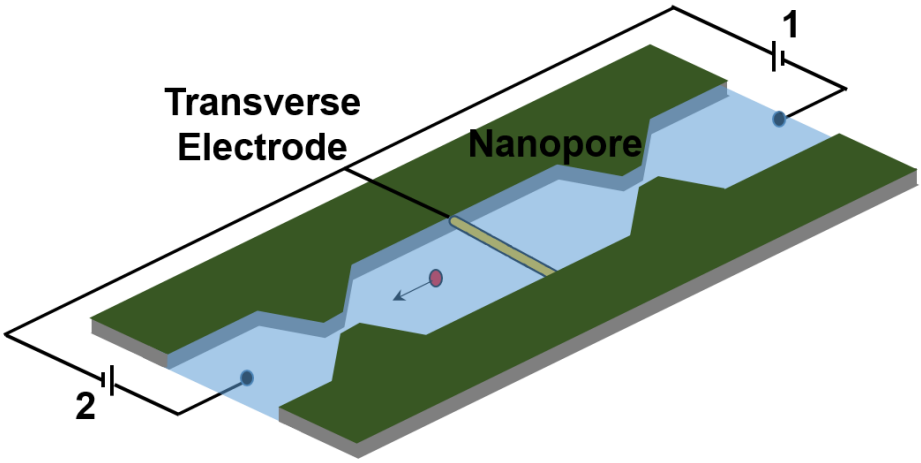

Figure 1.1. Schematics of the double nanopore-nanochannel sensor with transverse electrode

The technical objectives to achieve the goals of this study include:

1) Develop a technology to position and align pre-grown nanowires via a template method into polymer nanochannel fluidic devices;

2) Develop a technology to produce the testbed device in polymer substrate for ToF measurements during the translocation of individual molecules and particles through the nanochannel;
3) Optimize the design of the nanochannel-based single molecular sensors and their operation conditions via numerical simulation of the ionic current for the translocation events. The current drop occurring when a molecular or particle resides in the in-plane nanopore for different designs and operational parameters, such as geometries of the nanopore and nanochannel, ionic concentration, electrical potentials and etc., were simulated.
4) Demonstrate the ToF measurements for individual molecules and particles passing through the nanochannel and study the electrophoretic properties of those molecules and particles.

In continuation of this dissertation, Chapter 2 introduces the literature survey about the fundamentals of the electrokinetics and fabrication of double nanopore-nanochannel sensors with transverse electrodes. Chapter 3 introduces the assembly of the nanowires in parallel patterns controlled by using a handmade electromagnet. Chapter 4 represents the fabrication of microelectrodes to connect with nanowires. In Chapter 5, a technology to place nanowires to a target microelectrode was developed to fabricate the assembled nanoelectrode and the electrical properties of individual metallic nanowires were studied. Chapter 6 extends the study of the nanowires properties to the magnetic nanowires. Chapter 7 provides the finite element simulation of the interrogated transient current signals from the double nanopore-nanochannel sensor and analyzed the effects of the nanopore geometry on the current drop signal from the translocation of a nanoparticle through the nanopore. In Chapter 8 is shown the demonstration of the enclosed testbed device and its operation as nanofluidic device and detection of single molecules. In Chapter 9, the summary of this dissertation work and the perspective future works are given.

Chapter 2. Literature Survey

2.1. Introduction

This study concerns development of a new type of nanofluidic single molecular sensors utilizing time-of-flight (ToF) measurements for the translocation of single molecules and nanoparticles through the nanochannel. The testbed structure consists of a nanochannel, microfluidic networks and transverse electrodes made of pre-grown metallic nanowires. We seek for low cost fabrication technologies of the proposed devices where nanoimprint lithography is a technology to form nanofluidic structures and the ability of aligning and positioning pre-grown nanowires is a key technology to form transverse electrodes. Developing the proposed devices also requires understanding of electrokinetics of ionic solutions and particles in a nanoscale confined structure. Therefore, diverse fields of knowledge are required to develop this new type of single molecular sensors, which includes fundamentals to electrokinetics, synthesis and alignment of nanowires, as well as various micro and nanofabrication techniques. This chapter summarizes the literature survey on those topics. It should be noted that the term "nanoparticles" used in this chapter comprises all the biological single molecules such as DNAs, proteins and mononucleotides in addition to the conventional nanoscale organic/inorganic particles such as Au nanoparticles.

2.2. Nanofluidic single molecular sensors

2.2.1. Nanopore sensing for next generation DNA sequencing

Characterization and quantification of nanoparticles is a vital task for biosensing applications including drug discovery and curing diseases [31]. Subjects including accuracy, reliability and speed are crucial in the advancement of the techniques to study the nanoparticles [32]. The driving motivation for the invention of a fast, reliable and inexpensive technique to study nanoparticles has been the ability to perform DNA sequencing [31, 33]. DNA sequencing is to determine the order of DNA nucleotides and it is used to recognize the characteristics of living cells [34].

The traditional Sanger's sequencing method used DNA synthesis to label the single nucleotides by (dideoxynucleotide triphosphates (ddNTPs)) chain terminators to determine the DNA sequences [35]. Developments in these methods provided broad achievements in DNA barcoding and for the identification of each DNA types including bacterial, fungi and plant [36]. However, they can sequence the samples separately, which does not have enough throughput for the complicated natural samples containing different types of DNA samples. Sequencing the thousands of DNA samples in the environmental samples requires the parallel sequencing ability which is beyond the ability of the traditional methods [36].

Huge efforts have been made to find alternative methods for faster and high throughput DNA sequencing [37-39]. These methods are divided into two main groups: Sequencing by synthesis and nanopore sequencing [34]. The first method uses the ability of DNA polymerase enzyme to label each nucleotide and to read the DNA sequences. This method requires fluorescent labelling for readout the single nucleotides. The main advantage of using fluorescent labelling is the high sensitivity that it offers due to the emission of multiple photons during photobleaching. The problem with this method is that the label should be destroyed to continue the successful reading. In addition, the contamination error of the nucleotides has been addressed in this method. Another disadvantage of this method is that a large label may inhibit the correct reading from the nucleotide. Finally, the reaction between the oxidized fluorescein and other molecules may destroy the structure of the fluorescein which induces additional error in the sequencing [40]. Nanopore sensing has drawn significant interest as a next generation sequencing platform because it provides a label-free, amplification-free and single molecular sensing approach [41]. Several excellent review papers regarding nanopore sensors can be found in [4, 41-45]. The nanopore sensor utilizes the variations of electrical conductance between two sides of a nanopore filled by an electrolyte solution. The blockage during the translocation of a molecule or particle through the nanopore produces the variations (either

drops and increases depending on the experimental conditions) in the electrical conductance, which are used as molecular signatures. Both natural nanopores [46] and synthetic nanopores [47] have been used. The nanopore sensors have demonstrated the ability to identify DNA molecules of different lengths via the magnitude and duration of the blockade current peaks [48].

The main problem in obtaining the sequence information of DNA molecules with nanopore sensors is the high speed of the DNA molecule (~ 1 nucleotide per microsecond) [41] during the translocation through the nanopore which makes it difficult to distinguish the small changes in the ionic current by the presence of different mononucleotides [49]. Various efforts have been given to slow down the translocation of DNA molecules through the nanopore, which includes the incorporation of an enzyme into the nanopore [50-53], end termination of DNA with DNA hairpins and the use of positively charged residues in the nanopore as molecular brakes [54]. Despite such efforts, many challenges remain to be resolved to develop the nanopore sensor for enable sequencing by introducing the large genomic fragments such as DNAs into nanopores.

An alternative strategy to introducing large genomic fragments in nanopore sensing has been proposed, in which large genomic fragments such as DNAs are first cleaved by a highly processive exonuclease, the cleaved nucleotides are successively driven to the nanopore, and the individual nucleotides are detected by their ionic current variations [5]. It has been demonstrated using an aminocyclodextrin-modified α-haemolysin nanopore that the four mononucleotides can be distinguished using ionic current under optimized conditions [55]. The results indicate that a nanopore platform has the ability to decode the various long nucleic acids using a high throughput label free technique.

2.2.2. Nanopore sensing with transverse electrodes

The nanopore sensors with transverse electrodes is a promising platform to detect single nanoparticles by measuring the transverse current [56]. Transverse electrodes are formed perpendicular to the passage of nanoparticles in the plane of the nanopore membrane. The basic idea of the nanopore sensor with transverse electrode is to translocate a nanoparticle inside an ionic solution through the nanopore using the electric field applied to the nanoparticle by the macroscopic (longitudinal) electrodes on either side of the nanopore. This is followed by characterizing the nanoparticle by measuring the current blockage (resistive pulse) with the longitudinal electrodes and transverse nanoelectrodes simultaneously. The pair of nanoelectrodes are called sensing electrodes and this method is called transverse sensing [57].

The advantage of this method is that the motion of the nanoparticle can be stabilized between the transverse electrodes by applying a transverse electric field larger than the one applied by the longitudinal electrodes. This helps to decrease the noise on the current signal to a point that the current variations from the translocation of the nanoparticles are distinguishable from the noise although they still overlap each other [21]. In addition, surface modification of the metal transverse electrodes using a chemical reagent is an approach used to control the nanoparticle translocation speed and increase the signal-to-noise ratio of the transverse electrode with tunneling signal [58]. Another advantage is the control over the coupling between the nanoparticle and transverse electrodes by changing the material of the transverse electrode [59]. However, the ability to differentiate the nanoparticles does not obviously increase by the size of the nanopore or the strength of the transverse electric field. Also using the transverse electrodes does not dramatically change the stability of the ionic current through the nanopore or the properties of the nanoparticle translocation [59].

2.2.3. Double nanopore sensing with transverse electrode

The double nanopore sensor with transverse electrodes consists of two nanopores separated by a micro or nanochannel and transverse electrodes integrated into the nanopores.

The double nanopore sensor can hold the nanoparticle inside the spacing between the two nanopores and controllably release them with a voltage pulse. Another advantage of using the double nanopore sensor is that, since each of the nanopores operates as a separate resistive pulse sensor, the information collected from the translocation of each nanoparticle is doubled. Moreover, the interconnection between the two signals from the two nanopores provides additional information about the dynamics of the nanoparticle translocation. For example, the time required for the nanoparticle to travel between the two nanopores determines the time-of-flight (TOF). TOF is analyzed to identify the mobility, drift and the diffusion of the nanoparticle inside the nanopores during the nanoparticle translocation. However, the deficiency of the double nanopore is the disability to determine the correlation between the two current blockage signals from the translocation of a nanoparticle that moves fast between the two nanopores. Therefore it is hard to distinguish between such nanoparticles or to determine the nanoparticle dynamic information [24, 60].

The double nanopore sensor is also used in trapping and ejection of the nanoparticles. This makes it a flexible analysis and reaction chamber that acts like an artificial cell. Nevertheless, the number of nanoparticles inside the chamber increases linearly during the trapping phase while this number decreases exponentially during the ejection phase. This problem happens because of the interaction of the nanoparticles inside the chamber [61].

2.2.4. Nanopore vs. nanochannel sensors

The nanopore sensors provide an effective method to characterize single molecules including DNA, RNA, proteins, etc. with small amounts of samples and without the requirement for preparation of the sample [62]. In addition, the characterization can be performed with high sensitivity (signal to noise ratio) while there are a large number of contaminants in the sample. However, the pore dimensions should be designed precisely based on the size of the nanoparticle. Thus, the nanopore blockage makes a detectable decrease in the

ionic current during the translocation of nanoparticle. Another disadvantage of the nanopore sensors is the requirement to decrease the speed of the nanoparticle which makes it difficult to differentiate various types of nanoparticles [62].

Nanochannel based bioanalytic devices can be an alternative for the nanopore based devices to detect and characterize the nanoparticles [25]. The fabrication and integration of a nanochannel into the lab-on-chip devices is simpler than the nanopore and it has lower noise level in the translocation experiment. However, the current baseline of the translocation experiment for a nanochannel is higher than the one for a nanopore, which makes it more difficult to detect single nanoparticles with an only nanochannel, based devices.

We would like to use the nanochannel structure because the nanochannel provides the control over the translocation of the nanoparticle [25] and makes it easier to direct the nanoparticle to a vertical nanopore. In addition, the nanochannel between the two nanopore in the double nanopore-nanochannel testbed works as a flight tube for the nanoparticle which makes it easier for the nanoparticle to travel between the two nanopores without being deviated before entering the nanopore.

2.2.5. Fabrication challenges for nanopore and nanochannel sensors with transverse electrodes

The current fabrication methods for drilling the nanopore and nanochannels on silicon based materials (e.g. silicon nitride/silicon oxide) mostly use electron/ion beam lithography and subsequent pore size control with TEM/SEM facilities [63]. These methods can be combined with reactive ion etching and wet etching to fabricate pyramid-shape nanopores down to 20 nm [64]. However, the small pores with the diameters lower than 50 nm contract if a high electron beam intensity (around 10^5 to 10^7 Am^{-2}) is used. Also the pores higher than 80 nm in diameter expand in the presence of the high electron beam intensity [64].

Using the nanopores and nanochannels in silicon-based materials for the translocation of nanoparticles is a high cost and low throughput method. Efforts on using an efficient

fabrication process were done by replicating the nanopore and nanochannel structure into polymer based materials using the standard nanoimprint lithography process [65]. However, to make a closed nanochannel and nanopore structure to introduce fluids is the challenge of using this method. Using the temporary bonding of poly-dimethylsiloxane (PDMS) or thermal bonding between the polymers are the common methods to seal the nanochannel and nanopore [65].

There are a few methods reported in the literature to fabricate nanogap transverse electrodes on a nanopore structure. These methods include photolithography on metal deposited film and electron beam lithography [66]. In the first technique, metal nanogaps as short as 20 nm were achieved. However, this type of tunneling electrodes was unable to detect enough number of events from the translocations through the nanopore. Although the nanogap transverse electrodes fabricated by the second technique show a better functionality than the first technique, the fabrication method is not high throughput and requires well control over the deposition process [66].

2.2.6. Nanoimprint lithography for nanochannel sensors

Nanoimprint lithography to make the nanochannel sensor on poly(methyl methacrylate) (PMMA) is classified into two: 1. UV nanoimprint lithography which replicates the mold pattern into a UV curable resist. 2. Thermal nanoimprint lithography where the mold pattern is transferred into thermoplastic polymers such as PMMA [67]. Both imprinting methods have wide applications in fabricating the high aspect and large area structures including nanofluidics. By using thermal imprinting and thermal bonding process, sealed nanochannels can be achieved for nanofluidic applications. Most molds or stamps for nanoimprint lithography have been fabricated in Si via high-ends nanofabrication tools. However, Si stamps often lead to demolding problems in replicating to the UV curable resist or thermoplastic polymer. One method to reduce the demolding problem is the use of resin stamps. The low Young's modulus

of the resin stamp reduces the demolding force significantly. Examples of resin stamps are Polyurethane acrylate (PUA), tri-propylene-glycol-diacrylate (TPGDA). PUA is a commercial photoresist which has a higher viscosity. However, the TPGDA has good release properties and low viscosity [67].

2.3. Nanowires as sensing element

Nanowires are 1-D structures with nanometer size diameters that reveal distinctive physical properties including high current conductivity, sensitivity and performance. Therefore, nanowires are great candidates for novel sensors and nanoelectrodes [68].

Two main methods to produce metallic nanowires in high throughput include the use of solution chemistry, i.e. a reduction reaction of metallic precursors in the presence of surfactants to achieve anisotropic growth [69-71], and the use of electrodeposition in a porous template such as alumina and track etched polycarbonate to guide the one-dimensional growth [72-74]. The second method is high throughput and has a higher control over the electrical and mechanical properties of the nanowires. However, in order to utilize the pre-grown nanowires via the template method, the template has to be dissolved in the following step and the released nanowires in solution need to be positioned to desired locations of a substrate surface.

There are two main challenges in utilizing pre-grown, individual nanowires as a sensing component for lab-on-chip devices: first, pre-grown nanowires tend to agglomerate in solution after dissolving from their template and, second, the dissolved nanowires take random positions and orientations when deposited on a substrate surface [75].

In this study, we focus on the electromechanical properties of the metallic and magnetic nanowire nanoelectrodes based on their composition and fabricating the transverse nanoelectrodes using pre-grown nanowires, seeking for high throughput fabrication protocols for the sensors. The challenges include selection of the nanowire electrodes optimized composition, precise alignment and placement of the nanowire on a target substrate, produce a

nanogap into the nanowire, and connect the nanowire electrodes to microelectrodes to extract electrical signals from the sensors.

2.3.1. Metallic nanowire electrodes optimized compositions

Metal nanowires are great choices as electrodes for electronic devices such as touch screens and light emitting diodes (LED) because of their high surface to volume ratio and enriched electrons and protons surface scattering [76]. Silver nanowires have ideal electrical properties for display applications such as low resistance to transparency ratio. However, they are highly expensive to be used in large scale [77]. Although copper nanowires have relatively ideal electrical properties and price, they are prone to oxidation and chemical corrosion which can results in degradation of the nanowire conductivity [78].

In order to enhance the electrical and mechanical properties of the abovementioned homogeneous nanowires, core-shell nanowires are introduced. Core-shell nanowires have the ability to incorporate the properties of more than one component and allow various combinations of the core and shell in the nanowires. For example, core-shell Co_3O_4-NiO nanowires have higher structural stability and electrical conductivity than the CoO_x nanowires. While these properties allows them to be used lithium-ion batteries and chemical sensing applications the high surface roughness of the NiO shell is a limitation of these core-shell nanowires [79]. Another example is the core-shell Pd-Pt nanowires that reveal improved morphological and chemical properties because of the higher oxygen reduction reaction than the pure Pd nanowires. Conversely, the mass specific activity of the Pd-Pt nanowries is highly dependent on the Pd nanowire surface treatment before depositing the Pt shell which hinders the fabrication control of the core-shell nanowires properties [80]. The Te-Bi or Te/Bi_2Te_3 nanowires have enhanced thermoelectric properties compared to the pure Bi nanowires in terms of increased Seebeck coefficient and decreased thermal conductivity. However, the lowered

electrical conductivity of the core-shell nanowires results in their reduced thermoelectric power (ZT or figure of merit=0.05) [81].

2.3.2. Magnetic nanowire electrodes optimized compositions

Several critical applications including recording devices, magnetic sensors and magneto-optic devices require magnetic nanowires with enhanced mechanical and electromagnetic properties. Similar for the metallic nanowires, the heterogeneous core-shell nanowires exhibit enhanced functionalities.

Three layer NiFe-Cu-NiFe nanowires with two shells and a core have reduced saturation magnetization than the bulk NiFe nanowires since the shell material decreases the total magnetization of the nanowire. However, the outer layer of the nanowire is vulnerable to oxidation while predicting the electromagnetic behavior of the three-layer nanowire is very complicated [82]. The In_2O_3-NiMnGa core-shell nanowires reveal dislocations in the boundary between the core and shell by inducing a magnetic field which can be used to control various mechanical properties of the nanowires. Additionally, the ferromagnetic shell combined with the antiferromagnetic core controls further unidirectional magnetic anisotropy. High amorphous nature and relatively low ferromagnetic property of the nanowire compared to NiMnGa shell are the downsides of these nanowires [83]. The electromagnetic properties of the core-shell Ag-Fe_3O_4 nanowires can be controlled by either increasing the thickness of the Fe_3O_4 to enhance the ferromagnetic property or increasing the silver core thickness to increase the nanowire electrical conductivity. It is worthwhile to mention that the high price of the silver core together with the high contact resistance of the Ag-Fe_3O_4 nanowires reduce their cost efficiency for commercial electronic applications [84].

2.3.3. Alignment and placement of the nanowires

Integrating the nanowires in a defined orientation and location is a hard task because of the lack of an accurate alignment and placement technique for single nanowires. There have been efforts to placing individual nanowires on designed locations [85-91]. Such efforts can be

categorized into two types: large-scale assembly and single-nanowire manipulation techniques [92].

The large-scale assembly involves the arrangement of a group of nanowires on a large substrate [85-88]. This assembly process requires manipulation and deposition of nanowires. Assembly of nanowires by shear forces is one of the methods in this group [93-95]. This method utilizes the motion of a surface or liquid in opposition to the motion of another surface or liquid to create the shear force. The generated force induces the orientation of the nanowires toward the force direction on the substrate or inside the liquid. An example of this method is using the fluid flow inside a microfluidic channel to create the shear force and align the nanowires [94]. The advantage of this method is the ability to control the number of aligned nanowires with changing the flow rate inside the microfluidics. The drawback of this method is the disability of an accurate control of the alignment and positioning of the nanowires [85-88]. Another method of this group uses the magnetic field to direct magnetic nanowires inside a solution dropped on a substrate [94, 96]. The direction of nanowires is defined by the direction of the magnetic field which assembles the nanowires in the form of a chain structure (head of each connected to the tail of the other). The benefit of using this method is the ability to produce several designs of connected nanowires by using micron level magnets; nevertheless, such magnets require costly fabrication processes. Another disadvantage of this method is that the nanowire should include a material that can be manipulated by the magnetic field [89-91, 97-99].

Single-nanowire manipulation is performed inside an SEM chamber in vacuum condition and is composed of a setup to handle and place the nanowire on a target substrate [92]. Robotic manipulation is one of the methods of this group that consists of pick up and placement processes. In the pick-up process, a tungsten tip (as an end effector) is brought into contact with a nanowire on a carrier substrate. Electron beam deposition of platinum is used to

stiffen the connection between the tip and the nanowire after the contact. Then, the nanowire is picked up and aligned to the target substrate for the placement process. The placement process is achieved either by small structures on the target substrate to receive the nanowire by adhesion force or the deposition of platinum using the electron beam [100-104]. The advantage of this method is the fundamental reproducibility of the process and the ability to make a reliable electrical connection between the nanowire and the target substrate by the metal deposition. However, the problem of this method is the malfunction of the electronic switches after several processes due to the SEM chamber contamination [92]. Another method of this group uses an electrothermal microgripper to pick up the nanowire from the carrier substrate and place it on the target substrate. The pick up process consists of the approach of the mictrogripper to the nanowire, gripping and detachment of the nanowire by applying shear force. The nanowire is then placed on the target substrate by opening the microgripper followed by the deposition of platinum to weld the nanowire to the substrate. This method is capable of detachment of a pre-grown nanowire, handling and placement of the nanowire on a target substrate. However, the challenging alignment of microgripper to the nanowire in three dimensions and the low speed of the alignment process are the downsides of using this method [105, 106].

2.3.4. Nanogap formation in nanowire electrodes

Producing a nanogap in transverse nanowire electrodes especially for the gap size below 5 nm is a challenging task [107]. Some efforts have been given to produce such structures with controlled nanogap spacing [108-112]. Among various methods, the following three approaches to form nanogaps are relevant to this study: mechanical break junction [108, 109], focused ion beam (FIB) [110, 111, 113] and chemical etching [112, 114, 115].

In the mechanical break junction method, a nanowire with indentation is constrained to a flexible substrate [108]. An adjustable fracture occurs at the indentation by bending the

substrate that is controlled by a piezoelectric setup. The process requires low temperature and high vacuum conditions. The advantages of this method are stability and the controllability of the nanogap size (even during the operation) without polluting the gap. The problem with this method is the incompatibility with complicated nanosensor devices due to the limitation of piezoelectric components. Moreover, this method is not suitable for fabricating more than one nanoelectrodes and relatively large gaps [108].

The focused ion beam (FIB) is used as another method to insert a nanogap into the nanowire [110, 111, 113]. A nanogap in the order of 50 nm has been achieved by cutting the nanowire using FIB. The FIB has a minimum diameter of 5-20 nm which makes it suitable to insert nanogaps into the nanowire with high reproducibility and speed without using a mask. The method can be combined with the electron beam lithography to obtain nanogaps in the order of 20 nm [113]. However, the beam diameter is so large that it is difficult to produce nanogaps less than 10 nm [113].

Chemical etching of multisegmented metallic nanowires is another method to insert a nanogap into the nanowire [112, 114, 115]. A multisegmented nanowire is composed of several segments with different materials that are deposited electrochemically into a template. In the deposition process, the length of each segment can be controlled. Therefore, a segment of the nanowire with the size of the target nanogap is fabricated from a sacrificial layer that is removable by the wet chemical etching. The removed segment creates a nanogap into the nanowire with a desired length that is controlled by the electrodeposition process. The benefit of using this method is the ability of mass production (about one billion in an experiment) of multisegmented nanowires with controllable nanogap sizes. The disadvantage of this method is using the chemical etching process that may modify the properties of the materials of the segments near the nanogap [115].

2.3.5. Fabrication of microelectrode

In order to serve as sensing elements, nanowires placed in nanochannel sensors have to be connected to external electrodes. Thus, fabrication of microelectrodes and the connection to the nanowires are important fabrication steps. Microelectrode arrays have been widely used in electric, optical, and biosensing applications due to their superior properties including tiny size, huge current density and small background charging [116-118].

A variety of fabrication protocols have been developed for microelectrodes, which include photolithography techniques [119], electrochemical techniques [120], microcontact printing [121].

This study focuses on fabrication of nanochannel sensors in polymer substrate. Therefore, one prerequisite for the fabrication of microelectrodes is the compatibility with polymer substrate. The fabrication methods for microelectrodes compatible with polymer substrate include photolithography [122, 123] and UV directed electroless plating [124, 125].

In the photolithography, the microelectrode arrays are patterned into a photoresist using the conventional lithography process [123]. This is followed by the deposition of an adhesion layer into the microelectrode arrays to improve the attachment of the electrode layer to the substrate. Finally, the electrode material is deposited and the photoresist is lifted off. Another lithography process can be added to pattern an insulating layer on the fabricated microelectrodes. The main benefit of using this method is the control over the dimension and shape of the microelectrode arrays based on the application requirements. The downside of using such microelectrodes is the high cost of the fabrication process and the limitation in the application of such microelectrodes in electrochemical reactions [123].

The UV directed electroless plating uses the chemical modifications resulted by the UV exposure to a polymer substrate through an arbitrary photomask to incorporate the microelectrode arrays in the substrate [124, 125]. This is followed by a series of chemical

reactions to form the seed particles inside the microeletrode arrays and fabricate the microelectrodes by the electroless plating. The advantages of using this method are the accurate dimensions and favorable electrical properties of the microelectrode arrays. The disadvantage of this method is the weak adhesion of the microelectrodes to the substrate. The annealing helps to improve such problem; however, the annealing temperature is limited for the microelectrodes on the polymer substrates [125].

2.4. Electrokinetics in nanoscale confinement

Electrokinetics refers to the concept of using electric fields to generate motion of ionic fluids and suspended charged particles inside the ionic fluids. The electrokinetics is one of the most favorable methods in driving nanoparticles through nanopores and nanochannels because of the large electric field present inside the constricted regions. Both DC and AC can be used to drive nanoparticles. However, most of nanopore and nanochannel sensing utilizes DC. Therefore, we will focus on the DC electrokinetics, the main phenomena of which include the electrical double layer (EDL), electroosmosis and electrophoresis [126].

2.4.1. Classic theory of electrical double layer

The solid surfaces in the proximity of ionic solution obtain surface charge that in turn causes the surface to attract counterions and repel coions. This results in forming a thin layer mostly consist of counterions in the local area close to the surface that is called Electrical Double Layer (EDL) [126]. Figure 2.1 shows the ionic layers in the EDL.

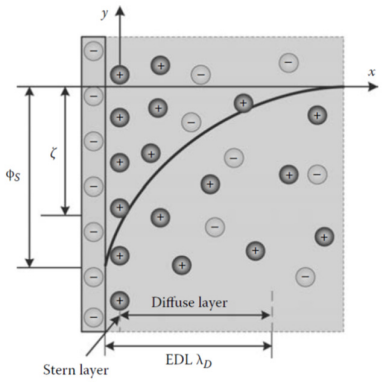

Figure 2.1. Schematics of the ions distribution in the EDL [126, 127]

In this figure, the electric potential of the bulk solution and the surface are ϕ_{bulk} and ϕ_s, respectively. The EDL consists of two layers namely stern and diffuse layers. The Debye length (λ_D) characterizes the EDL thickness. The stern layer is close to the surface and the ions are immobilized in this layer. The layer above the stern layer is the diffuse layer in which the ions move freely. The shear plane separates the stern and diffuse layers. The electric potential difference between the shear plane and the bulk solution is called zeta potential (ζ). The electric potential and ionic flux within the diffuse layer obey the Poisson and Nernst-Plank equations, respectively.

Several methods are designed to control the electrokinetic transport in micro/nanofluidics by tuning the parameters inside the electrical double layer [128-130]. One of these methods uses the applied potential (gate potential) by a field effect transistor (FET) inside the micro/nanochannel walls to control the electrokinetic transport of the nanoparticle inside the ionic fluid by changing the solid/liquid interface potential. The charged surface of the channel walls by the gate potential causes redistribution of ionic concentration inside the channel. The simulation study of these phenomena showed the control over the ionic concentration and zeta potential inside the EDL. However, the ionic concentration and electric potential are considered uniformly distributed along the surface and the particles' motion is not considered in this simulation [131].

2.4.2. Electroosmosis

Applying an electric field to the EDL induces a motion to the ions due to the migration of the counterions toward the electrode with opposite charge parallel to the electric field. This is called elecrtroosmosis and the fluid motion is called electroosmotic flow. The electrokinetic force applied to the ions can be calculated based on the coulomb's law and the fluid motion obeys the Navier-Stokes equation [126]. Several fluid flows with the focus on mixing enhancement [132, 133], local dispersion control [134] and dynamic flow control [135] can be

generated by controlling the gate potential along the EDL. The numerical simulation of the electroosmotic flow along the gate potential on a planar surface showed the variations of the flow velocity by changing the gate potential [136]. Based on this simulation, in the absence of gate potential the electroosmotic flow has a quick growth inside the EDL and has a constant value outside the EDL (in the bulk zone). In such condition, the zeta potential is uniform and the electroosmotic flow is constant along the flow direction. Applying a negative potential to the gate center results in a non-uniform zeta potential and an electroosmotic flow conjugate with the initial electroosmotic flow. Finally, a positive gate potential induces an electroosmotic flow that is reverse to the initial electroosmotic flow near the gated surface. This simulation has the ability to study the uniform and nonuniform zeta potential induced by the gate potential; however, it is unable to simulate the vortices induced by the reverse flow [136].

Another simulation study tries to investigate the effects of electroosmotic flow on the transport of a nanoparticle inside a nanopore [137]. The results of this study shows that a negative gate potential attracts positive ions near the nanopore; therefore, the electroosmotic flow is opposite to the direction of nanoparticle's motion that slows the nanoparticle down. A positive gate potential applies an electroosmotic flow compliant to the direction of nanoparticle's motion. Also, under a certain gate potential, the nanoparticle can be trapped inside the nanopore. The advantage of this simulation is the ability to predict the direction of the induced electroosmotic flow with respect to the nanoparticle's motion. Using the axial symmetry and the neglecting the fluid rotation is the disadvantage of this simulation study [137].

2.4.3. Electrophoresis

The translocation of charged nanoparticles under an external electric field inside an ionic solution is called electrophoresis. In another word, the charged surface of the electroosmosis is converted to mobile for the electrophoresis. The velocity of the nanoparticle

has a linear relationship with both particle's mobility and the external applied electric field. The mobility of the particle under electrophoretic force is calculated from Helmholtz-Smoluchowski law for the small zeta potential and Huckel law for the large zeta potential in the equilibrium of EDL [126]. The electrophoretic force applied from the external electric field in the nanopore axial direction is included in the aforementioned simulation of a nanoparticle inside a nanopore. This simulation is able to calculate the velocity of the nanoparticle regarding the driving electrophoretic force and resistive electroosmotic force. The results show that the negatively charged nanoparticles migrate in the nanopore reverse to the direction of the applied electric field. However the disadvantage of this simulation is neglecting the nanoparticle rotation because of the simplicity purposes [137].

A more complicated simulation study tries to control the nanoparticle dynamics inside a conical nanopore by changing the electroosmotic and electrophoretic forces and applied external pressure on the ionic fluid surrounding a charged nanoparticle [138]. This simulation shows the dependence of the electrophoretic and electroosmotic forces on the nanoparticle and the nanopore charges, respectively. Therefore, the two forces increase with different rates by increasing the external electric field while the pressure remained constant for all simulations. This simulation is successful to calculate the nanoparticle velocity based on the sum of applied forces under low applied external electric fields. However, these results have huge discrepancies from the experimental results at high electric fields. This is because of the disability of the simulation in considering inhomogeneous electric field, nanoparticle-nanopore interaction and nanoparticles diffusion [138].

2.4.4. Simulation of electrokinetic behavior in nanoscale confinement

The physics used to model simulate the electrokinetic behavior in nanopore and nanochannels include the fluid dynamics of water along with the ion transfer of the KCl solution, electrostatic voltage and current of the external electrical circuit connected to the ionic

solution. Equation (4) shows the Navier-Stokes equations in 3D space. The Navier-Stokes equation was used to simulate the fluid (water) flow in nanochannel with low velocities.

$$u\nabla u = \frac{1}{\rho}(-\nabla p + \eta\nabla^2 u - F(\sum_i z_i c_i)\nabla\Phi) \quad (1)$$

In which, u, ρ, ∇, p, η, Φ and F were the velocity vector, density of the fluid (water), gradient vector, pressure of the fluid, viscosity of the fluid, electric potential and Faraday's constant, respectively. In this equation, $\rho \times u\nabla u$ and ∇p represented the inertia term and external pressure applied to the ionic fluid and $\eta\nabla^2 u$ was the force induced by the viscosity of the fluid. In addition, $F(\sum_i z_i c_i)\nabla\Phi$ was the electroosmotic force applied to the fluid in which z_i and c_i were the charge of the species "i" (K or Cl), respectively [138].

Equation (5) represented the Nernst-Plank equations used to simulate the ion transfers in the fluid because of the applied electric field.

$$J_i = (-D_i\nabla c_i - \frac{Fz_i}{R_{MT}T} D_i c_i \nabla\Phi + c_i u) \quad (2)$$

Where J_i and D_i were the ion flux vector and diffusion coefficient of species i. R_{MT} and T were the molar thermal resistance and the absolute temperature of the medium (KCl solution). The three terms on the right side of this equation represented the ionic flux caused by the diffusion, migration and convection of the ions. In addition, J_i, c_i, Φ and u were quantities that depend on the position of the fluid.

Equation (6) showed the last constraint, the Poisson equation.

$$\nabla^2\Phi = -\frac{F}{\varepsilon}\sum_i z_i c_i \quad (3)$$

Where ε was the permittivity or dielectric constant of the KCl solution. The Poisson equation correlates the electric potential profile to the ionic distribution.

Efforts have been made to simulate the effects of the non-uniform surface charge of the nanopore wall on the ionic current for nanopores [139-141]. The results of the simulation show that the non-uniform surface charges influence the concentration of the ions at the tip of the nanopore, which changes the ionic current. This becomes more important when the ionic

concentration decreases. Although this simulation was able to predict the effects of the non-uniform surface charge of the nanopore on the ionic current, it was unable to consider the convective ionic current [139]. Another simulation studies the effect of surface charge of the nanoparticle on its translocation through a cylindrical nanopore [142]. This simulation predicts the effects of non-uniform surface charge of the nanoparticle on the local ionic concentration and electric potential. The results also predict the electrophoretic motion of the nanoparticle based on the non-uniform surface charge of the nanoparticle. Because of the electroosmotic flow surrounding the nanoparticle with non-uniform surface charge, the motion of the nanoparticle mostly becomes independent from the viscous force. The weakness of this simulation is the assumption of momentum, mass and electrostatic transport as almost steady phenomena [142].

Chapter 3. Reduction of Agglomeration of Nanowires

3.1. Introduction

Nanowires are an important device component in lab-on-chip applications. In particular, metallic nanowires have great potential to be used as electrical sensing components for biosensors [31, 143] to convoy the measured electric signals from biomaterials to the macroscale world. The common method to produce metallic nanowires in high throughput is to grow inside a nanopore template using electrodeposition [144]. The template has to be removed from the grown nanowires by dissolving in an etching solution, followed by a separation step by centrifugation. In the next step, the nanowire-dispersed solution is deposited on a substrate surface in order to place individual nanowires at designated locations. For biosensing applications long nanowires are desired from the integration point of view because it will be easier to connect the nanowires to micro to macroscale external electrodes. There are two major problems in achieving long, individual nanowires on a surface: first, a significant portion of long nanowires break during the separation process and, second, nanowires are agglomerated during the separation and deposition processes. Despite the demonstration of placing individual nanowires at designated locations in the literature [145], the problem of nanowire agglomeration in the separation and deposition processes still remained unsolved in most of the practical use of nanowires.

Several approaches have been proposed to reduce the agglomeration problem of nanowires after the electrodeposition process. Intense stirring, shear mixing or sonication [146-148] is one of the methods that uses energy to separate the agglomerated nanowires. This method helps dissolving the nanowires template, however, the nanowires break to shorter lengths while colliding to each other, stirrer blade or the walls of the container. Using a surfactant to maintain the nanowires separated after dissolving their template is another way to solve the problem [147]. Using the surfactant more than the critical micelle concentration

makes the nanowires repel each other and be stable in their solution [149]. Since the agglomeration of nanowires happen because of the high surface tension of water in many cases [150], supercritical CO_2 drying can be used to increase the hydrophobicity and prevent the agglomeration of the nanowires at the same time [151]. Also, a solvent can be used during the growth of the nanowires to increase their hydrophobicity. This will prevent the growth and agglomeration of the nanowires at the same time [152]. However, all of the abovementioned methods only slightly reduce the nanowire agglomerates and thus it is still needed to develop additional methods to further reduce this problem.

In this chapter, we present a new method to reduce the agglomeration of nanowires during their deposition on a surface. This method utilizes an intermediate membrane coated on the substrate where individual nanowires are deposited. Instead of depositing nanowire solution on the substrate directly, the solution is deposited on the intermediate membrane, which will act as a filter for nanowire agglomerates. During the lift-off of the intermediate membrane, individual nanowires are re-suspended from the membrane surface and deposited on the underlying substrate while a majority of nanowire agglomerates remain on the membrane surface. Consequently, the fraction of individual nanowires to nanowire agglomerates increases compared to the case without using the intermediate membrane.

3.2. Experiment

3.2.1. Fabrication of nanowires

Electrodeposited NiFeCo nanowires were fabricated by growing them in an alumina template of 0.5 µm diameter. Details on the electrodeposition process can be found in our previous work [153]. The target length of nanowires during electrodeposition was 30 µm. After the growth of the nanowires, the alumina template was soaked in 2 M NaOH solution within a shake couvette. The couvette was then shaken to enhance dissolution of the alumina template from the grown nanowires. The solution was decanted and the nanowires were rinsed with

NaOH, water and ethanol three times. Sonication was not used in our process in order to reduce the breakage of nanowires.

3.2.2. Fabrication of the substrates

Si was used as a target substrate on which nanowires were deposited. For the preparation of the intermediate membrane, a double resist layer was coated on the Si substrate (1.5 cm × 1.5 cm.): first, a 1 μm thick dextran layer which serves a sacrificial layer and then a 2.47 μm thick polyurethane acrylate (PUA) layer as the membrane layer. On the membrane surface, we formed parallel grooves with the width of 1.4 μm and period of 2.71 μm via nanoimprint lithography. The microscale grooves were initially intended for capturing individual nanowires over nanowire agglomerates in order to increase their separation efficiency but due to the random orientation of the deposited nanowires the capture of individual nanowires by microscale grooves did not seen to work.

3.2.3. Deposition of the nanowires

For the deposition of nanowires, a sample of 10 μL was taken from the bottom part of the couvette and dispensed on the Si surface (as reference) or on the intermediate membrane formed on the Si substrate. A same couvette with a constant density of nanowires was used for all samples to maintain the number density of nanowires in the deposited drops. In order to study the effect of the tilt angle on the separation of individual nanowires, the substrate was tilted when we deposited the nanowire solution on the substrate. The tilt angle was defined an angle formed between the substrate surface and the horizontal axis. Six different angles were selected and each substrate was oriented with a certain angle during the deposition of nanowires. After the deposition, the membranes were detached by dissolving the underlying dextran sacrificial layer in DI water. After drying the sample, the samples were inspected first by optical microscopy and some samples were selected for scanning electron microscopy. A majority of nanowires are ~ 30 μm long, as determined by scanning electron microscopy after depositing on a bland Si substrate. However, nanowires significantly shorter and longer than

30 µm were also observed. Short nanowires resulted from the breakage of nanowires during the removal of the alumina template while long nanowires were formed by oxidation in the presence of NaOH solution. Figure 3.1 shows schematics for the process of utilizing an intermediate membrane in the deposition of individual nanowires on the Si substrate to reduce nanowire agglomerates.

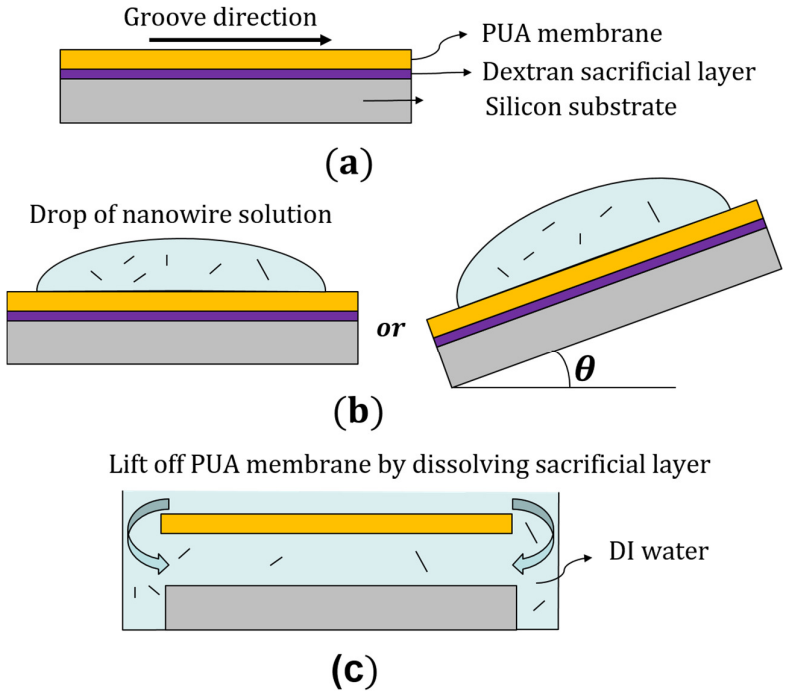

Figure 3.1. Schematic diagram of the process of utilizing an intermediate membrane in the deposition of individual nanowires to reduce nanowire agglomerates. (a) Si substrate coated with a dextran sacrificial layer and a PUA intermediate membrane layer, (b) deposition of a drop of nanowire solution on the intermediate membrane surface (the substrates were tilted in direction of the grooves), and (c) lift-off the intermediate membrane by dissolving the sacrificial layer in DI water.

3.3. Results and discussion

3.3.1. Microscopic observations

Figure 3.2 (a) shows an optical micrograph for the nanowires deposited on a blank Si surface without a tilt angle.

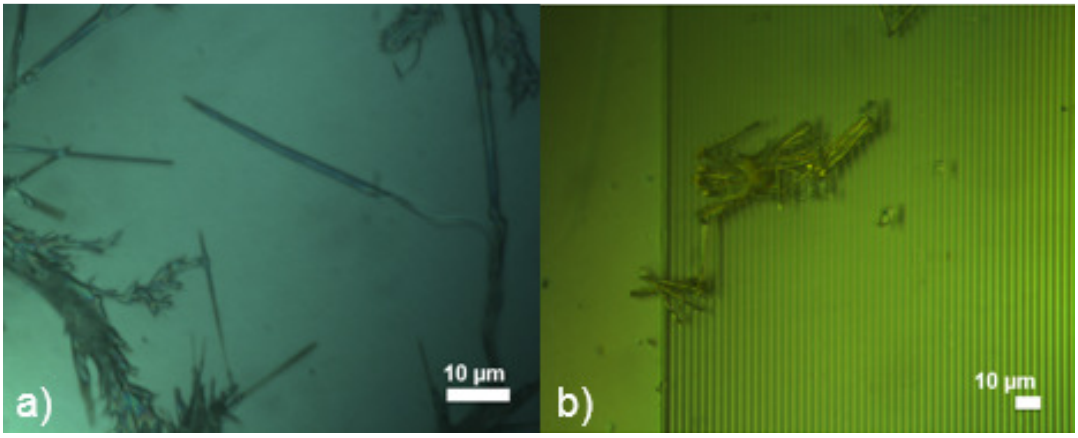

Figure 3.2. Optical micrographs for nanowires deposited on the (a) blank Si surface (reference substrate equal to a membrane without grooves) b) an intermediate membrane coated on Si substrate.

Agglomerated nanowires are clearly visible, which are caused mainly by the following two reasons: (1) large surface tension of nanowire surfaces that attract to each other and (2) incomplete removal of the Au layer used as seed layer for the electrodeposition of nanowires so that nanowires are still attached to the residual Au layer. Such nanowire agglomerates were found over the entire surface while individual single nanowires were seen sporadically, which indicates that our process using gentle shaking is not effective in dissolving the alumina template and separating individual nanowires. Figure 3.2 (b) shows an optical micrograph for the nanowires deposited on the intermediate membrane coated on Si substrate without a tilt angle prior to the detachment of the intermediate membrane. The image is similar to that shown in Figure 3.2 (a), which indicates that nanowire agglomerates are formed irrespective of the substrate used for deposition.

Figure 3.3 (a) shows an optical micrograph and Figure 3.3 (b) shows a scanning electron micrograph for single nanowires found on the Si surface after removing the intermediate membrane by dissolving the dextran sacrificial layer in DI water.

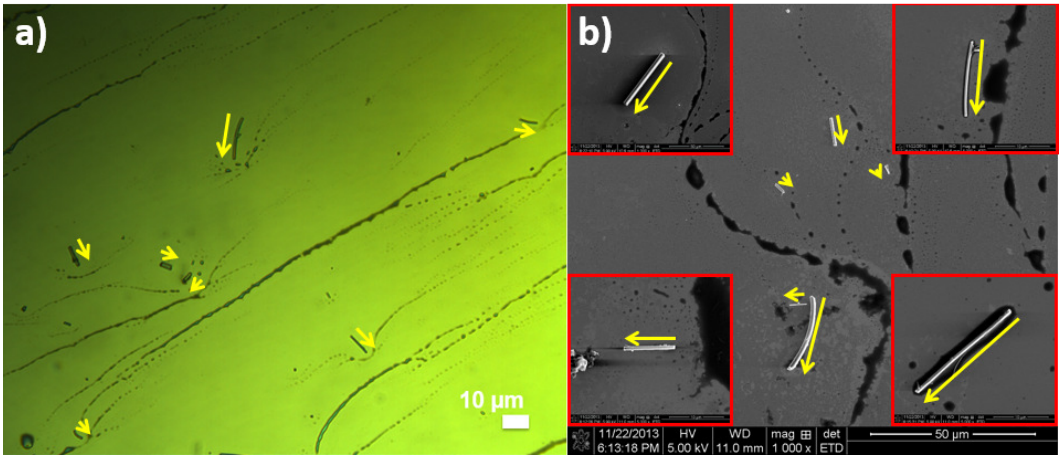

Figure 3.3. a) Optical micrograph b) Scanning electron micrographs of single nanowires deposited on Si substrate after dissolving the intermediate membrane in DI water. Nanowires are highlighted by arrows. Four insets show nanowires in different areas of the substrate.

Four insets in the figure shows nanowires found in different locations of the same substrate. Overall, the nanowire agglomerates seen in Figure 3.2 were rarely observed on the Si surface. This behavior can be explained by the fact that individual nanowires were re-suspended during removal of the intermediate membrane and deposited on the underlying Si surface while most of the nanowire agglomerates remained on the intermediate membrane surface. Thus, the intermediate membrane from one side acted as a filter to screen the nanowire agglomerates from reaching to the underlying Si surface and from the other side acted as a separator to help disconnecting the single nanowires before reaching to the substrate. Since the tilted membrane acted as a filter and separator and the underlying substrate was used only to hold the membrane, this substrate could be replaced by another substrate. The results indicate that, in the deposition of pre-grown nanowire solution on a substrate surface, using an intermediate membrane layer can help achieving predominantly single nanowires on the surface. It should be mentioned that this improvement was sacrificed by the decrease in the total number of nanowires deposited on the substrate. For a horizontal substrate with 0° tilt angle, the number of agglomerated nanowires observed in the 3×3 mm^2 surface area were 22 after the deposition on the membrane while this number decreased to 4 after removing the

membrane. This is because, in the process of removing the intermediate membrane layer, the substrate was put in a petri dish containing DI water and thus the concentration of nanowires re-suspended in the water solution became significantly low. The studies on the number density of single nanowires for bio sensing applications [25, 154] shows the direct effects of number density of nanowires on the sensitivity of the bio sensing device (e.g. field-effect transistors (FETs)). These studies showed that using a higher number (seven instead of one) of bridging nanowires (which might be agglomerated nanowires) for FETs can reduce the sensitivity of the device by the order of five. Despite the reduction of the number of nanowires deposited, the method that we developed in this work can be a useful particularly in cases that the presence of nanowire agglomerates on a substrate surface in the nanowire deposition step prohibits proceeding to the subsequent fabrication steps in the preparation of nanowire-based biosensing devices. We can also employ methods to increase the number of nanowires deposited, such as use of high concentration nanowire solution and a small volume of DI water for removing the intermediate membrane.

3.3.2. Statistics

After demonstrating the concept that the intermediate membrane can reduce the nanowire agglomerates, we systematically studied the effect of the slope of the intermediate membrane in the deposition step on the number of single nanowires found on the Si surface after lifting off the membrane. For this study, we hypothesized that short nanowires deposited on the membrane may slide a longer distance on the membrane surface by gravity over long nanowires or nanowire agglomerates and thus there will be more short nanowires in the peripheral region of the droplet of the nanowire solution. Thus, upon lift-off of the intermediate membrane, a larger number of short, single nanowires will be transferred to the underlying Si surface. Note that in our nanowire solution there are nanowires of different lengths due to the breakage of nanowires or oxidation in the solution processing of removing the alumina

template after nanowire growth. Figure 3.4 shows the number of nanowires deposited on the underlying Si surface as a function of the tilt angle between the substrate and horizontal axis when depositing nanowire solution on the intermediate membrane.

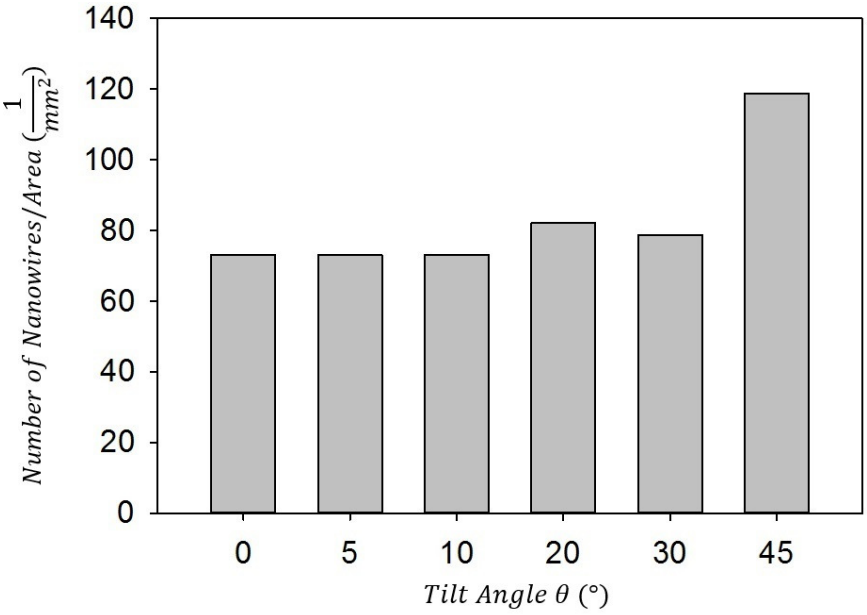

Figure 3.4. The number of nanowires deposited on the underlying Si surface as a function of the tilt angle between the substrate and horizontal axis when depositing nanowire solution on the intermediate membrane.

For counting the number of nanowires, we took optical micrographs for the surface area of 0.117×0.117 mm^2 in the center part for each sample and count the number of entire nanowires within the surface area. This area was under the part of the membrane which had grooves before the removal of the membrane. For the tilt angle other than 45°, the number of nanowires deposited per area of the Si surface did not increase. However, at the tilt angle of 45°, the number of single nanowires increases more than 70% relative to that for the other tilt angles.

Figure 3.5 (a) presents the number of nanowires for various length groups. The number of nanowires with the length between 5 and 10 μm was the greatest irrespective of the tilt angle used.

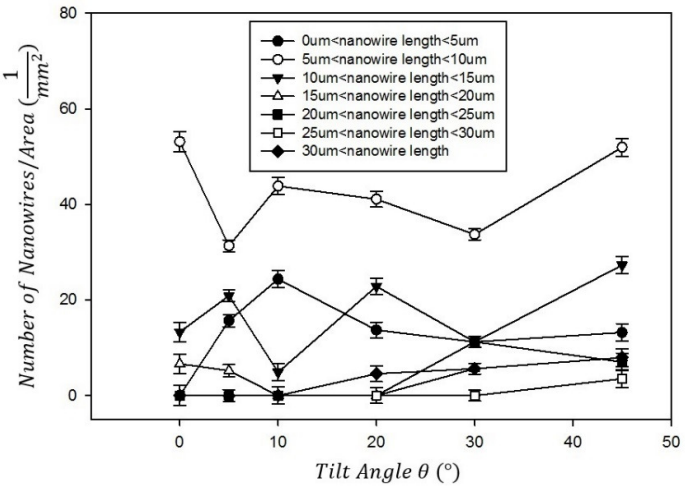

(a)

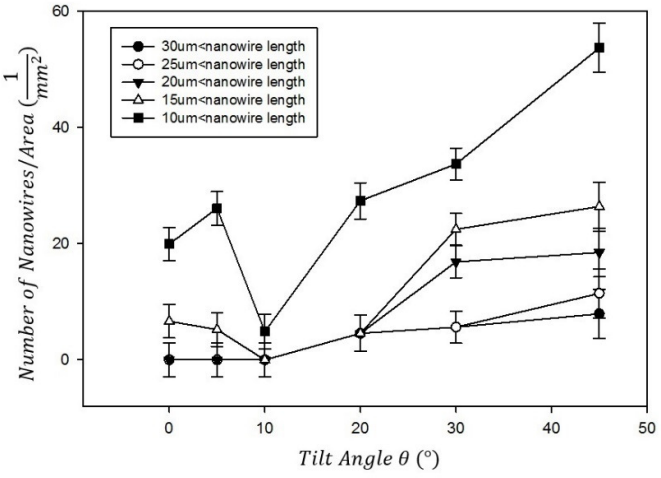

(b)

Figure 3.5. (a) The number of nanowires (NW) (a) in different length groups and (b) cumulative above a certain critical length, which were deposited on the Si surface after lift-off of the intermediate membrane layer as a function of tilt angle between the substrate surface and horizontal axis.

The nanowires with the length of 0 – 5 μm were less frequently observed than that for 5- 10 μm, which can be attributed to the difficulty in the breakage of initially 30 μm long nanowires to very short ones. On the other hand, the frequency of finding nanowires longer than 10 μm on the Si surface was significantly lower for all the tilt angles. We re-plotted Figure 3.5 (a) for the cumulative number of nanowires above a certain critical length, which is shown in Figure 3.5 (b). As the tilt angle increased, the cumulative number of single nanowires above each critical nanowire length increased with the tilt angle. However, the extent to the increase

was greatest with the shortest critical length while the increase was the least for nanowires with the length of 30 μm and above. Long nanowires have higher surface area over the short nanowires, which increases the total adhesion force either between nanowires and the surface of the membrane or between different nanowires. Therefore, long nanowires can slide over the membrane surface only the tilt angle exceeds to a certain value while short nanowires can slides at all tilt angles. This makes the separation process of the longer nanowires harder than the shorter nanowires. Considering that the nanowire agglomerates exert even larger adhesion to the surface than even long nanowires, it can be deduced that nanowire agglomerates will mostly remain on the membrane surface during the lift-off process. Consequently, the membrane will act as filter for the nanowire agglomerates.

3.4. Conclusion

We developed a method to reduce nanowire agglomerates in depositing pre-grown nanowires on Si substrate. Nanowire solution was deposited on an intermediate membrane layer coated on the Si substrate on which nanowires needed to be deposited. Upon lifting-off the intermediate membrane in DI water, single nanowires were re-suspended and deposited on the underlying Si substrate while a majority of nanowire agglomerates remained on the membrane surface. By tiling the substrate with the intermediate membrane in depositing nanowire solution, we found that the sliding of long nanowires over the membrane surface is more difficult, requiring a larger tilt angle over short nanowires. This corroborates the hypothesis that most of nanowire agglomerates will remain on the intermediate membrane surface during the lift-off process.

We study a new method for the large-scale assembly of magnetic nanowires in the next chapter. This method aligns single nanowires on a patterned substrate by using the electromagnetic and mechanical forces. The aligned nanowires will be used for the final alignment and placement of the transverse nanoelectrodes.

Chapter 4. High Precision Nanowires Alignment Into Plastic Substrates

4.1. Introduction

Ferromagnetic nanowires have an inherently larger remnant magnetization compared to nanoparticles due to their high aspect ratio shape, that permits its use in low field environments for cell manipulation [155, 156]. In circuits, Ni nanowires have been used in a tunable stop-band notch filter [157], and they hold promise in the field of microfluidics, as an actuation element for micro-valves, pumps, and mixers [158]. As metal electrodes for electrochemical detection in miniature devices, typically noble metal nanowires (e.g., Pt, Au, Ag) have been used, as comprehensively reviewed by Gencoglu and Minerick [159]. There is not only a need to find a less expensive replacement, but transition elements that are ferromagnetic also provide the added benefit to magnetically manipulate the nanowires into a device [160-163].

Ji et al. [164] recently reviewed the methods to generate interconnects of nanowires in devices, that includes a two-step process where the nanowire is aligned and then pinned to remain in place. Efforts to align and position template-grown nanowires can be classified into three types depending on the forces used to control the orientation of the nanowires: forces by fluid flow, field forces, and surface forces (or surface patterns). In the first type, preferential orientation of nanowires was induced via either evaporation of the solvent [165-167], spontaneous spreading/wetting/flow of the nanowire solution [168-173] or brushing of the nanowire solution [174]. Alignment of the nanowires on an area as large as 4 cm^2 have been demonstrated by using spontaneous spreading of the droplets of the nanowire solution [169]. Drawbacks of using fluid flow included the high average misalignment angle (typically more than 20°) of the nanowires [169] and the difficulty in apply a uniform capillary or shear force to the nanowires [75]. Also, the large shear force upon brushing led to the deformation or breaking of the nanowires [174]. In the second type, either optical [175-177], electric [178-

182] or magnetic [89, 183, 184] field force was used to control the orientation of nanowires. An optical tweezer could align nanowires into arbitrary patterns generated by computer aided design. However, this method is limited to a small scale assembly of nanowires [177]. The applied electric or magnetic fields between two large electrodes or magnets could align a large number of nanowires suspended in fluid. Beside the presence of a misalignment, chaining of more than one nanowires inside the electric [181] or magnetic field [89] was observed, in particular when a high concentration of nanowire solution was used. The last type of alignment techniques employs surface forces via chemical [184-188], topological surface patterns [189], and shear force induced by surface [190, 191], to assemble nanowires within specific locations of the substrate. These techniques overall show a low ratio of aligned nanowires when they are not combined with other techniques [186, 192]. A successful example in this type of alignment techniques is the use of strain release on highly stretchable substrates where an accurate alignment of nanowires on a flexible substrate as large as 2 inch × 6 inch was achieved [193]. However, this method requires high elasticity of the substrate as well as application of large forces between the elastic substrate and the nanowires, which significantly limits the applicability of this method.

High precision and large scale alignment of nanowires has been achieved by combining more than one of the alignment techniques mentioned above. Examples include alignment using the sites of patterned microscale electrodes [194] or nanoscale magnet arrays templates [90] (and magnetic trapping using microscale magnet arrays [155]) and nanoscale topographical grooves patterns combined with capillary force [195]. The first two examples demonstrated a micron level precision, but they required complicated low throughput fabrication processes for microelectrodes or micro/nanomagnet arrays [90, 155, 194]. The method combining surface chemical patterns with capillary force showed that short nanowires with the length less than 100 nm can be positioned within the chemically-patterned trenches

with high angular as well as location accuracies [195]. However, the applicability of this method for nanowires longer than several microns needs to be further studied, which would make it easier to connect the aligned nanowires to external micro to macroscale electrodes.

The pre-grown nanowire mentioned in the first chapter are suspended (and partially agglomerated) in a solution after the dissolution of their template before being used as nanoelectrodes. Thus, they need to be aligned and dried separately on a desired substrate to be prepared for the subsequent connection to external electrodes or placement on the final nanochannel-nanopores device. In this chapter, a new method is presented that combines a magnetic field force with topological microscale grooves to control and achieve high precision alignment of magnetic nanowires with various lengths. Although individually both methods have been demonstrated in the literature, [196-201] the combined effect can significantly improve the alignment accuracy for nanowires. To differentiate this method with others, it is referred to as pattern electromagnetic alignment (PEA).

4.2. Experimental

4.2.1. Nanowires fabrication and preparation

FeNiCo composite nanowires were pulsed electrodeposited in a nanoporous alumina template with 0.2 μm diameter pores and up to 30 μm in length. Details on the electrodeposition process can be found in [202]. After the electrodeposition, the alumina template was dissolved with a 2 M NaOH solution overnight. The dissolved nanowires were then rinsed with water and ethanol three times. After dissolving the alumina template, the nanowires were kept in ethanol. Adding the surfactant could help reducing the aggregation of the nanowires, but based on our observations, there were still a significant amount of aggregated nanowires even in the presence of surfactant, especially at large nanowires concentrations [203]. Some nanowires were broken during the preparation process, so that the nanowires had different lengths. An aliquot of 10 μL of the nanowire solution was used for each experiment.

4.2.2. Substrate preparation for electromagnetic and PEA

A schematic of the process steps is shown in Figure 4.1. Blank Si substrates for the electromagnetic alignment were squares of 1.5 cm × 1.5 cm (Figure 4.1a), and since the reorientation of the nanowires were affected by parameters (e.g. stochastic surface and fluid flow forces) other than the deterministic magnetic field force, the nanowires easily deviated from the direction of magnetic field line after the evaporation of the solvent. Groove-patterned substrates for the PEA were fabricated via nanoimprint lithography into a double layer of 1 μm dextran and 2.5 μm polyurethane acrylate (PUA) coated on the Si substrates. The width of the grooves was 1.4 μm and their period was 2.71 μm (Figure 4.1b). The patterned area was a 3 mm × 3 mm square in the center of the substrate in order to enhance alignment of the nanowires.

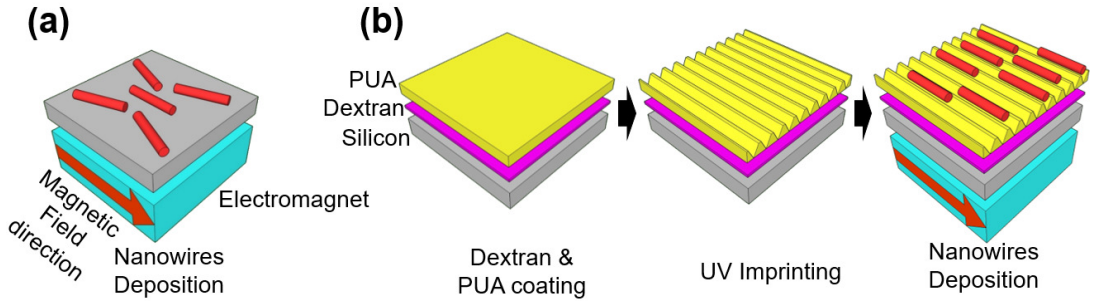

Figure 4.1. Schematic steps for (a) electromagnetic alignment (nanowires deposited onto blank silicon substrates) and (b) PEA on a microscale grooved surface formed by UV nanoimprint lithography ino a double resist layer of dextran and PUA.

4.2.3. Electromagnetic and PEA

The electromagnetic alignment and PEA of magnetic nanowires were performed in separate experiments to determine the accuracy of the alignment versus applied magnetic field strength, using both the blank substrate for the electromagnetic alignment (Figure 4.1a) and the patterned substrate for the PEA (Figure 4.1b), with identical conditions. Four samples were prepared and analyzed for both electromagnetic alignment and PEA experiments at each applied magnetic field strength.

A nanowire solution was dispensed on the substrate while the substrate was placed on the electromagnet. The magnetic field was then induced by the electromagnet which was connected to a (BK 1735 DC) power supply. The current was constant during each experiment.

4.2.4. Inspection and characterization

A 3 mm × 3 mm square in the middle for each sample was inspected by optical microscopy and scanning electron microscopy (SEM). This area corresponds to the patterned area for the PEA samples. The deviation angle (θ_D) and the length of the nanowires (l) were measured manually from the optical micrographs. The deviation angle was defined as the angle between the nanowire direction and the direction of the magnetic field lines (or the direction of the grooves). The lengths and angles of nanowires were measured with a computer desktop ruler using optical micrographs taken with a 40X objective. Prior to using this method, the lengths of three nanowires determined using scanning electron micrographs were compared with those measured by optical micrographs. The lengths determined by optical micrographs were consistently larger by 0.7 ± 0.2 μm. Thus, overall measurement error in the determination of individual nanowires is less than 1 μm. For the nanowire deviation angles, the measurement error was estimated to be ~ 2°.

4.3. Results

The nanowire diameter size had a large variation, 270-580 nm, due to both the irregularity of the AAO template and also due to the subsequent treatment in NaOH that is used to dissolve the membrane. The NaOH promotes the formation of oxide, as expected from Pourbaix [204], and with the formation of an oxide the diameter size increases owing to the larger specific volume compared to the metallic counterparts. Figure 4.2(a) and (b) presents SEM images of the nanowires in group and individually, respectively. Not only is there a distribution of diameter size but also length. The different lengths are used to advantage here

and their alignment accuracy are correlated with ranges of wire lengths: 0-10 μm, 11-20 μm, and 21-30 μm (i.e. $0 < l \leq 10$ μm, $10 < l \leq 20$ μm, and $20 < l \leq 30$ μm, respectively).

The detailed distribution of lengths of all the nanowires used is shown in Figure S1 of the Supporting Information. In the analysis of alignment accuracy, the nanowire lengths were grouped with the following ranges for better observation of the general trend: 0-10 μm, 11-20 μm, and 21-30 μm (i.e. $0 < l \leq 10$ μm, $10 < l \leq 20$ μm, and $20 < l \leq 30$ μm, respectively).

The diameter of nanowires cannot be determined accurately with optical micrographs due to its resolution limitation. However, SEM images of selected nanowires showed that the diameter is in the range of 250 – 580 nm.

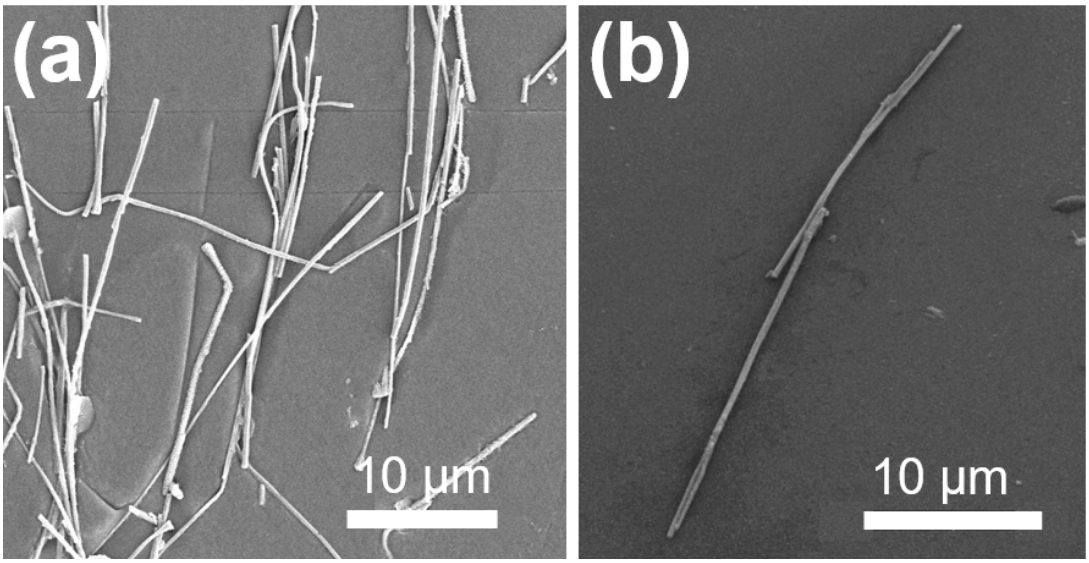

Figure 4.2. SEM images of FeNiCo nanowires in (a) group and (b) individually after they are released from the AAO membrane.

4.3.1. Electromagnetic alignment and PEA

Figure 4.3 and 4.4 show micrographs of nanowire alignment after the ethanol from the nanowire solution have evaporated. In Figure 4.3, only the electromagnetic alignment was used and in Figure 4.4 the combined PEA method was employed. The applied magnetic field in both cases was 70 Oe. The image in the center of each figure corresponds to an optical micrograph showing an overview of the substrate. The nanowires in the optical micrograph for the

electromagnetic alignment (Figure 4.3), are circled with red lines as a guide. The large spot on the sample in Figure 4.3 corresponds to impurities remaining after evaporation of solvent. In Figure 4.4, the nanowires aligned by PEA method appear longer due to head-to-tail connections to each other. Such head-to-tail alignment of nanowires have been observed when field forces were used [89, 181]. In the PEA case, this behavior may be related to the modulation of the magnetic field strength at the surface, leading to an increase in the probability for more than one nanowires to encounter each other within a single groove. The SEM images in Figure 4.3 and 4.4 show examples of individual nanowires found on the substrate. The direction of the magnetic field lines is parallel to the y direction for both alignment methods. The orientation of nanowires was determined using the optical micrographs. Overall, most of nanowires for both alignment methods show preferential directions along the magnetic field lines. However, for the electromagnetic alignment one can still observe nanowires with orientations far away from the magnetic field lines (marked by the yellow numbers 5-8). On the other hand, most nanowires are aligned along both the field lines and the groove direction for the PEA.

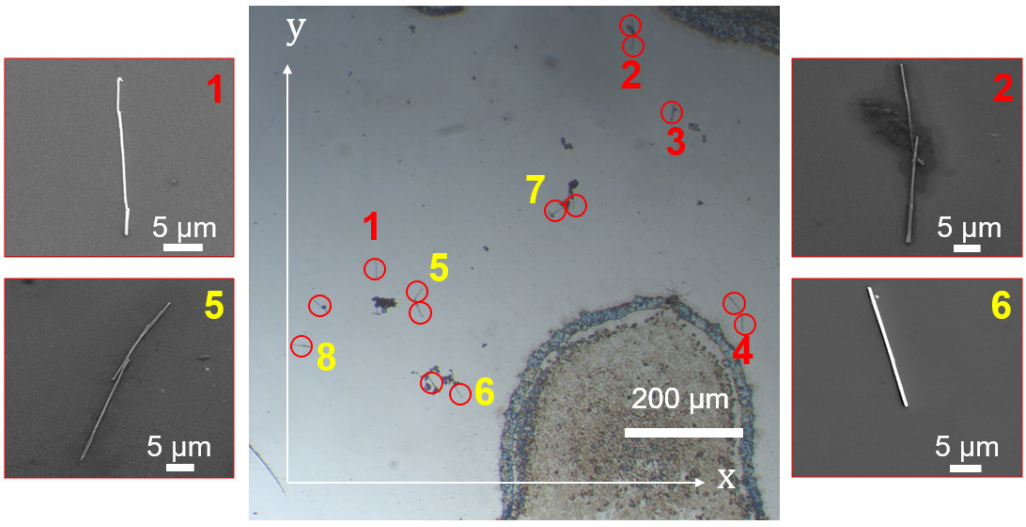

Figure 4.3. An optical micrograph (center) and SEM micrographs (right and left) of FeNiCo nanowires using electromagnetic alignment on Si substrates at a magnetic field strength of 70 Oe. The numbers in the SEM image corresponds to the very same nanowire marked (in red, (1-4) in the optical micrograph. The nanowires marked with the yellow numbers (5-8) were oriented far away from the magnetic field lines. The applied magnetic field lines are parallel to the y direction in the optical micrograph. Individual nanowires in the optical micrograph are circled for clarity.

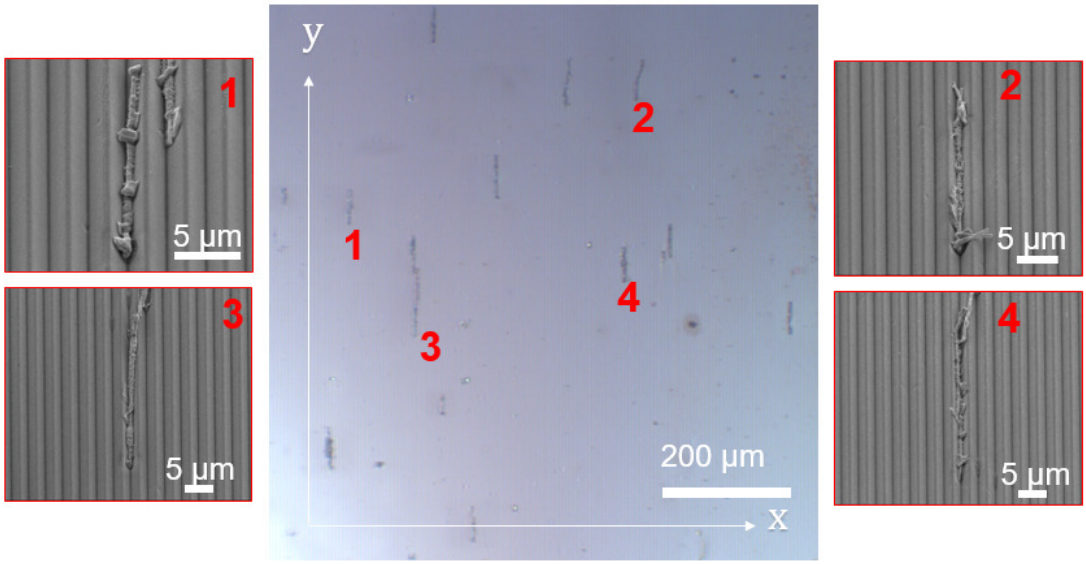

Figure 4.4. An optical micrograph (center) and SEM micrographs (right and left) of FeNiCo nanowires using PEA on the microgrooves formed in a double resist layer of dextran and PUA on Si substrates at a magnetic field strength of 70 Oe. The numbers in the SEM image corresponds to the very same nanowire marked in red, (1-4) in the optical micrograph. The applied magnetic field lines are parallel to the y direction in the optical micrograph.

4.3.2. Statistical analysis

In order to quantitatively determine the accuracy of the alignment, statistics were determined by measuring the deviation angle (θ_D) from the direction of the magnetic field line for all the nanowires found in a square area of the 3 mm × 3 mm in the middle of each substrate (which corresponds to the pattern area for the PEA). We plotted the normalized angular distribution diagrams of nanowires versus applied magnetic field strength from 0 to 90 Oe. For each applied magnetic field strength and nanowire length group, the number of nanowires within a certain deviation angle group was divided by the total number of nanowires found in the same sample area. The error bars were determined as one standard deviation of the normalized values of the four samples of each distribution. Statistics were determined for different groups of the nanowire length of 0-10 µm, 10-20 µm and 20-30 µm. As representative results, Figure 4.5 (a) and (b) shows the statistical diagrams for the nanowire length of 0-10 µm for the electromagnetic alignment and PEA methods, respectively. The results of the

alignment on samples without an applied magnetic field (i.e, 0 Oe), but with patterned groove alignment is compare to the PEA results. For quantitative analysis, the deviation of aligned nanowires from the direction of the magnetic field lines was determined as well as the full width at half maximum (FWHM) value from each fitted Gaussian curve. Also, the percentage of the total number of nanowires with a deviation angle less than 5° from the direction of the field lines was calculated. The summary of these two values and their corresponding standard deviations as well as the total number of individual nanowires found for a certain group of nanowire length are presented in Table 4.1 and 4.2 Overall, the FWHM value of the fitted Gaussian curve decreases as the magnetic field strength increases for both alignment methods, which indicates that more nanowires are aligned close to the direction of the field line with the magnetic field strength. The FWHM value decreases consistently from 180° without magnetic field (randomly oriented) to 15 ± 1° at 90 Oe for the PEA. For the electromagnetic alignment, on the other hand, the FWHM value decreases only to 32 ± 11° at the same magnetic field, which is more than two times greater than that for the PEA. Also, the percentage of the nanowires with less than 5° deviation angles for the PEA is more than four time higher than the electromagnetic alignment at all the applied magnetic field strengths except for 0 Oe.

Figure 4.6(a) and (b) show the angular distribution diagrams of the nanowires for the three length groups of 0-10 μm, 10-20 μm and 20-30 μm at a magnetic field strength of 90 Oe for the electromagnetic alignment and PEA, respectively. For PEA, the FWHM value slightly decreases from 17 ± 3° for long nanowires of the 20-30 μm length group to 15 ± 1° for short nanowires of the 0-10 μm length group by ~ 10%. However, this value fluctuates between 24 ± 4° and 44 ± 9° for the nanowires with different lengths for electromagnetic alignment. For each group of magnetic field strength and nanowire length, the percentage of nanowires with less than 5° deviation angle is higher in the PEA (above 40% for all of the length ranges) than that in the electromagnetic alignment. Overall, the alignment accuracy of shorter nanowires

was higher than that for longer nanowires for the PEA. One of the main mechanism of this trend is the dynamics of the shorter nanowires suspended inside the solution under an applied magnetic field. Ignoring the nanowire-surface interaction, the rotational velocity of nanowires can be modeled by balancing the magnetic and hydrodynamic forces applied to a nanowire [205, 206]. The results show that the rotational velocity of shorter nanowires is higher than that of the longer nanowires [205, 206]. Thus, at all applied field strengths shorter nanowires require a shorter rotation time than the longer nanowires to align with the direction of the magnetic field line before approaching and attached to the bottom substrate. This mechanism results in a better alignment accuracy for shorter nanowires than longer ones. Also for both longer and shorter nanowires, the efficiency of the PEA is higher than the electromagnetic alignment at the high (90 Oe) applied magnetic field strengths.

Figure 4.7(a) and (b) show 3-dimentional (3-D) graphs of the FWHM values for applied magnetic field strengths (0-90 Oe) and nanowire length groups for the electromagnetic alignment and PEA, respectively. The 3-D graph clearly shows the general trend of increasing the alignment accuracy (or decreasing the FWHM values) with increasing the magnetic field strength and with decreasing the length of nanowires. Another important to note is that more systematic trends are seen for the PEA compared to those for the electromagnetic alignment. This can be attributed to the fact that, while the process for nanowires to approach the flat substrate surface and the re-orientation during solvent evaporation is stochastic, the surface groove patterns in the PEA add deterministic characteristics during both nanowire deposition and solvent evaporation processes. This leads to the decrease in the FWHM values for the PEA.

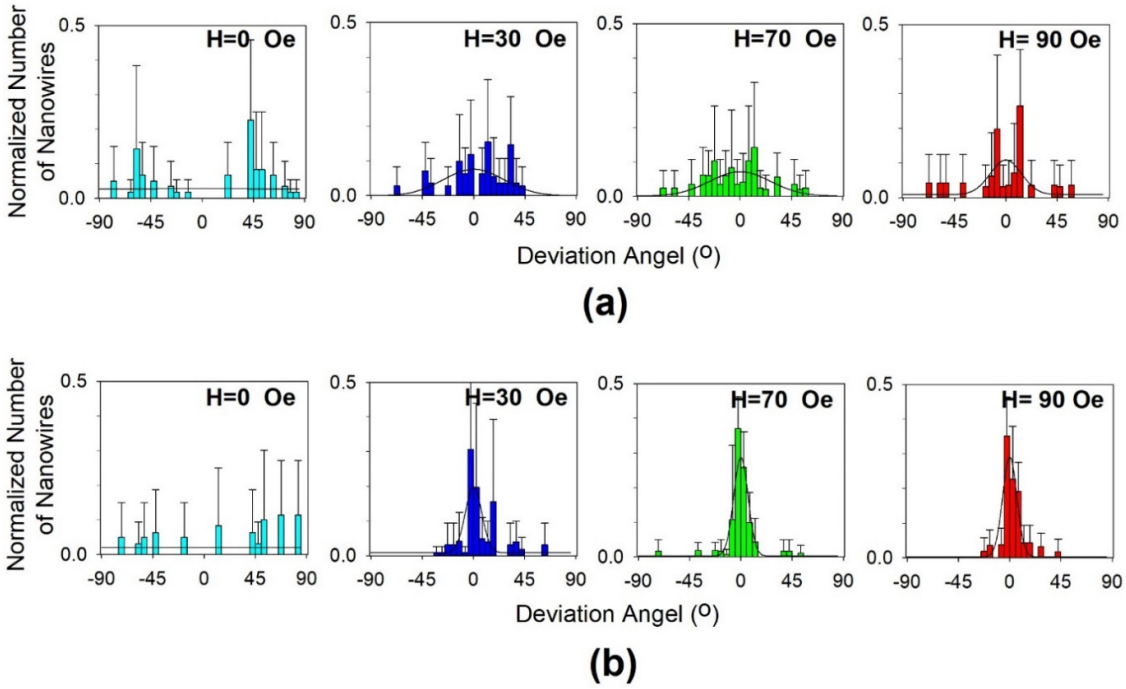

Figure 4.5. Normalized number of nanowires for the nanowire length group of 0-10 µm as a function of the deviation angle for different magnetic field strengths for (a) electromagnetic alignment and (b) PEA methods. For each angular distribution diagram, the corresponding fitted Gaussian curve is included.

Table 4.1. The full width at half maximum (FWHM) values and the standard deviations obtained by the Gaussian curve fitting from the angular distribution diagrams for different magnetic field strengths and nanowire length groups for both electromagnetic alignment and PEA. Also included in [ ] are the total number of nanowires for each group of magnetic field strength and nanowire length.

FWHM	Nanowires Length (µm) \ Magnetic Field Strength (Oe)	0	10	30	50	70	90
Electro-magnetic alignment	0-10	180 ± 95 [24]	180 ± 94 [12]	63 ± 19 [26]	54 ± 19 [18]	63 ± 16 [35]	32 ± 11 [23]
	10-20	180 ± 94 [22]	93 ± 51 [15]	60 ± 16 [52]	38 ± 8 [40]	24 ± 4 [42]	44 ± 9 [41]
	20-30	180 ± 95 [76]	139 ± 68 [86]	32 ± 5 [123]	39 ± 7 [95]	25 ± 4 [91]	24 ± 4 [94]
PEA	0-10	180 ± 96 [16]	63 ± 42 [12]	17 ± 4 [44]	15 ± 3 [32]	15 ± 2 [78]	15 ± 1 [56]
	10-20	180 ± 93 [61]	67 ± 19 [68]	22 ± 4 [76]	17 ± 2 [71]	17 ± 2 [77]	17 ± 2 [76]
	20-30	180 ± 94 [105]	96 ± 48 [98]	28 ± 7 [90]	18 ± 5 [99]	17 ± 2 [146]	17 ± 3 [144]

Table 4.2. The percentages of the number of nanowires with the deviation angles less than 5° and their standard deviations obtained from the angular distribution diagrams for different magnetic field strengths and nanowire length groups for both electromagnetic alignment and PEA.

Percentage for $\lvert\theta D\rvert < 5°$	Nanowires Length (μm) \ Magnetic Field Strength (Oe)	0	10	30	50	70	90
Electro-magnetic alignment	0-10	0 ± 0	5 ± 10	12 ± 16	7 ± 8	8 ± 16	7 ± 13
	10-20	3 ± 6	17 ± 33	7 ± 6	20 ± 7	27 ± 14	13 ± 13
	20-30	1 ± 3	9 ± 5	16 ± 12	19 ± 13	30 ± 14	39 ± 22
PEA	0-10	0 ± 0	11 ± 13	50 ± 64	41 ± 30	63 ± 20	58 ± 27
	10-20	7 ± 9	20 ± 23	31 ± 27	35 ± 26	49 ± 13	52 ± 17
	20-30	3 ± 3	19 ± 15	23 ± 14	27 ± 9	40 ± 13	41 ± 8

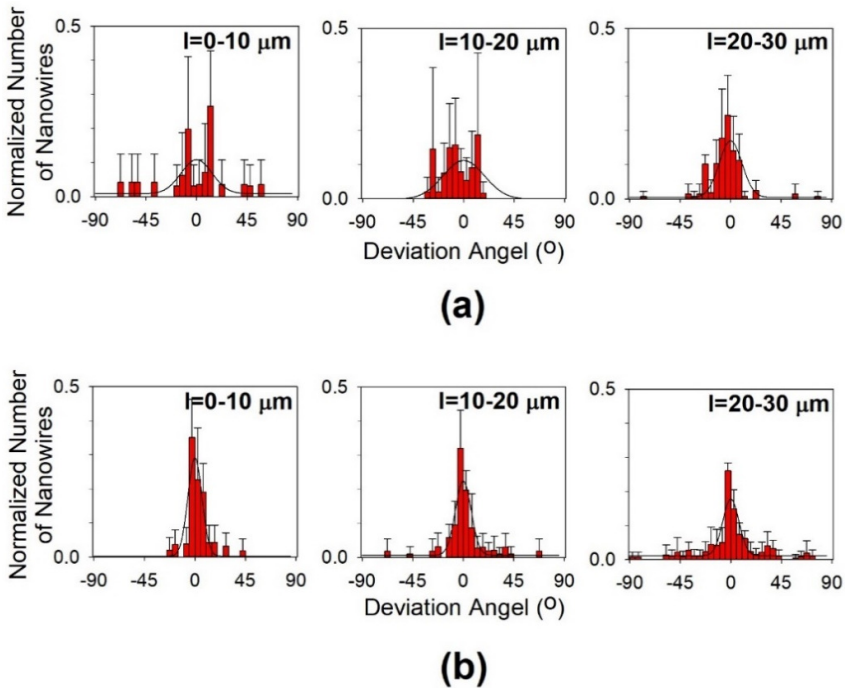

Figure 4.6. Normalized number of nanowires at a magnetic field strength 90 Oe as a function of deviation angle for different nanowire length groups for (a) electromagnetic alignment and (b) PEA methods. For each angular distribution diagram, the corresponding fitted Gaussian curve is included.

4.4. Discussion

The positioning of magnetic nanowires on a substrate surface is a two-step process: in the first step nanowires in suspension rotate towards the direction of the magnetic field line, which is concurrent with the process to approach to the surface via surface-nanowire

interaction. The forces exerted by a surface on a depositing nanowire broadly consist of adhesion and friction, both of which depend on the material properties such as surface energies and Young's moduli, and the interfacial properties such as the friction coefficient and the contract area [207]. The presence of surface grooves changes the interfacial properties and makes adhesion and friction anisotropic. When a nanowire is deposited into the trench of a microgroove, the effective contact area may increase depending on the location of the nanowire in the trench, leading to an increase in both adhesion and friction. In addition, the geometric interlocking significantly increases the friction in the direction perpendicular to the groove, which increases pinning of the nanowire against any shear force such as evaporation of the solvent [169]. This effect becomes more significant as the depth of the groove increases. On the other hand, when a nanowire is deposited on the protrusion of a microgroove, the effective contact area may decrease, leading to a decrease in adhesion and friction. It is worthwhile to mention the effect of the microchannel depth on the alignment accuracy. For a given magnetic field strength, there would be a critical depth of the microchannel. Above this critical depth, the pinning of nanowires in the microchannel trench is so large that nanowires once deposited in the trench of the microchannel cannot escape upon external force such as capillary force and evaporation of solvent. In this regime, the alignment accuracy will not change with the depth of the microchannel. On the other hand, when the depth is below the critical depth, nanowires in the microchannel trench can escape upon external force, resulting in a decrease in the alignment accuracy. In this regime, the alignment accuracy may depend on the depth of microchannels. The depth of the microchannel used to align nanowires should be determined in consideration of the design of the final device as well as compatibility of the subsequent manufacturing process steps.

The deposited nanowires may experience re-orientation during evaporation of the solvent. Using different solvents will modify (1) the time for nanowires to rotate upon

application of electromagnetic field, (2) the time for nanowires to reach the substrate surface, (3) the time for solvent evaporation, and (4) the magnitude of shear force applied during evaporation of solvent. However, the average nanowire rotation time by the electromagnetic field used in this study is in the order of tens of milliseconds (based on the **Figure S5**), significantly shorter than the time for nanowires to reach the surface and the time for solvent evaporation which are in the order of minutes. Thus, the effect of solvent on the nanowire rotation is negligible. The different shear force applied by different solvents upon evaporation may affect reorientation of nanowires, which will vary the alignment accuracy depending on the depth of the grooves. It should also be noted that the main reason to select ethanol as the solvent for these nanowires was to prevent any further oxidation before the nanowires final assembly. The effect of the viscosity of solvent would be negligible in PEA. The main mechanism to align nanowires in this study is the magnetic field with the support of surface patterns, which help pin the nanowires along the groove direction after the nanowires approach the surface. Increasing the viscosity of the nanowire solution will result in an increase in the nanowire rotation time by the electromagnetic field because of the elevated resistive hydraulic force, especially for longer nanowires. This will adversely affect both electromagnetic alignment and PEA.

The results indicate that the PEA is a highly powerful technique which systematically aligns individual nanowires of various lengths with higher accuracy compared to only electromagnetic alignment or only groove pattern alignment. The PEA technique can be used to place not only nanowires, but also nanotubes or other magnetic particulates. The less than perfect 100 % alignment accuary presented here demonstrates the challenge in alignment when the nanomaterial is not homogenous. Nanowires with more uniform feature sizes would be expected have higher alignment accuracy and less alignment distribution and thus larger FWHM values. This technique can also be applied to curved substrates in combination with

the technology to produce micro/nanoscale patterns on curved substrate for flexible electronics. The PEA technique can also be used in diverse applications such as large scale parallel nanowires for optoelectronics on glass [208] and silicon [209, 210] substrates, and high performance transistors on silicon based substrates [211, 212].

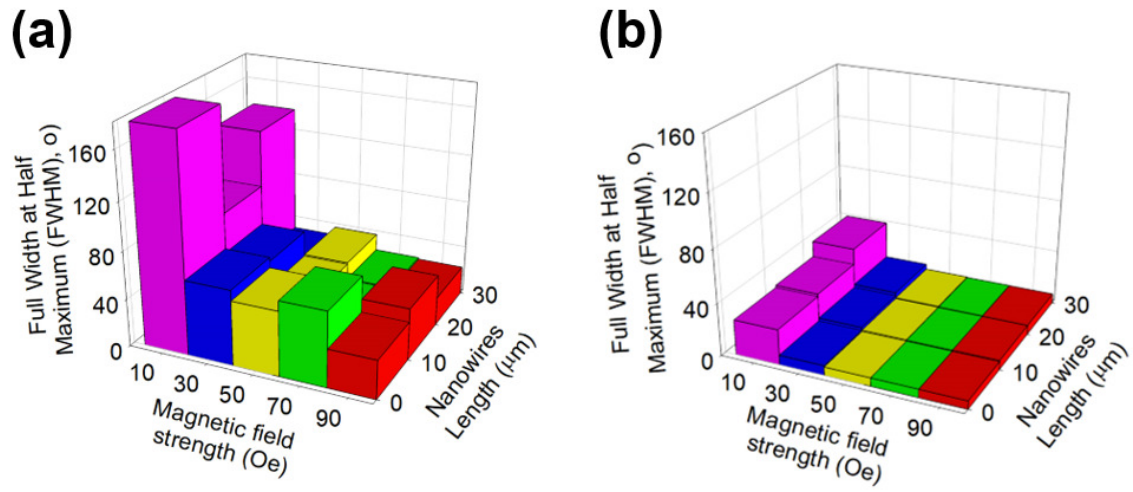

Figure 4.7. 3-D graphs for FWHM values versus applied magnetic field strength and nanowires length group for the (a) electromagnetic alignment and (b) PEA.

4.5. Conclusion

A new alignment method (PEA) is presented that combines electromagnetic alignment with microscale surface groove patterns to realize large scale, high precision alignment of magnetic nanowires. Compared to only an electromagnetic alignment, or only a grooved pattern alignment, the PEA of FeNiCo nanowires demonstrated a systematic enhancement of the alignment accuracy, the percentage of the nanowires having less than a 5° deviation angle from the direction of the magnetic field lines for the PEA remained above 40% at the highest applied magnetic field. For both the PEA and electromagnetic only alignment methods, the alignment accuracy increased with increasing the magnetic field strength and decreasing the nanowire length. The PEA that is developed in this work has the potential to be impletemented in processed to build sensing elements with pre-grown magnetic nanowires.

Chapter 5. Fabrication Of A Microelectrode Pattern Compatible With Plastic Substrates

5.1. Introduction

The field of flexible electronics has been dramatically expanding in a variety of new applications such as wearable electronics and bendable cell phones. Also, flexible electronics have potential to be used in portable biomedical devices. In flexible electronics, electrical components such as metallic electrodes are formed on thin, flexible plastic or elastic and their electrical properties should remain unchanged upon deformation [213]. Depending on applications and materials, the fabrication technique for the electrodes should be compatible with non-flat or highly curved substrates. Among a variety of fabrication protocols that have been developed for microelectrodes, only few of these techniques are compatible with the fabrication of microelectrode arrays on polymer substrates which are mostly known as transparent, biocompatible and flexible materials [214-216]. For instance, by using photolithography or chemical techniques, one can produce microelectrode patterns with the smallest features down to 50 μm [214-216]. However, the high baking temperatures and the solvents used in photolithography and chemical techniques are not compatible with most of the polymer substrates. The stencil mask technique is an easy method to implement and have the potential to be used on unconventional substrates of different materials and surface geometry. However, the main challenge of using stencil masks on non-flat substrates is blurring. The primary reason of blurring is the presence of a gap between the substrate and the stencil mask due to the curvature on the stencil/substrate, stress on the stencil or other topographies on the substrate surface [217]. In particular, when stencil masks are formed in hard materials e.g. Si_3N_4 or SiO_2 on Si substrate, as is the case for most nanoscale stencil masks, it is hard to avoid the presence of the gap [218]. One of the most effective approaches to reduce the blurring issue is using a stencil mask made in a compliant membrane, so that the stencil mask can conform and have contact with the curved substrate compared to the hard stencil masks [219]. Cantilever

assisted compliant membranes is an alternative flexible stencil mask which has the ability to attach to different shapes of the substrate to reduce the gap distance between the stencil and substrate thus decreases the blurring. But because of mesa structures in compliant membranes that move with respect to each other, these membranes have different thicknesses at the different locations of the membrane. Also these membranes need complicated fabrication process and additional characterization of cantilever beams deformation which make the entire process with high demand [220]. Stencil masks in polyimide films are another example of compliant membranes with high resistance to heat and chemicals. However, the high thickness of the available commercial polyimide films (7-15 μm) makes the fabrication of small patterns difficult on these films due to the problems of isotropic etching of the membranes with high aspect ratio feature size [221]. Transparency, flexibility and neutrality of polydimethylsiloxane (PDMS) membranes to chemicals make them great stencil membrane candidates while the blade removal to open their aperture and difficulty in inserting small scale apertures are the main challenges of PDMS stencils [219]. The stencil membranes made inside photoresists have the pattern ability in large area and can produce patterns on flat and curved substrates. For the large patterned areas with high in plane aspect ratio of the patterns, it is very difficult to transfer the membrane to the target substrate without damaging the membrane. Also the alignment of the membrane is very difficult due to the fragility of the membrane especially with lower thickness [222]. Overall, the current polymer stencil masks reported on SU8 [223], PDMS [224] and parylene-C [225] materials were limited to a thickness more than 10 μm with large minimum pattern dimensions of 100 μm [225] or fragile thin membranes of 0.5 μm thickness on polystyrene [226] and PMMA [227] with low flexibility and limited to small areas of less than 1 mm × 1 mm [227] and small maximum hole length (less than 100 μm).

In order to connect the nanowire electrode on the nanochannel-nanopore device to the outside electronics, micron size electrodes on plastic substrate are required, therefore they do

not overlap with micro-/nanofluidics. To fabricate microelectrodes on micro-/nanochannel substrate, compliant stencil masks with reduced blurring effects and low risk of stencil fracture or damage are required. In this chapter, we developed a new method of handling and manipulating stencil masks made in a thin SU8 membranes (down to 2 μm) and small feature size (5 μm minimum) with large patterned area (~1.5 cm × 1.5 cm) and large maximum hole length (0.8 cm). We addressed the main challenge in the current polymer stencil mask technologies that is the difficulty in handling and manipulating thin and large area polymer stencil membranes with multiscale features. Using this technique, we also studied the effect of the thickness of the polymer stencil mask on the conformal contact of the membrane to highly curved substrates and the patternability of metallic electrodes using the stencil masks.

5.2. Experimental

Figure 5.1 shows the process steps to fabricate the membrane by photolithography on SU8 resist over a thin layer (250 nm) of water soluble resist (Dextran) over silicon wafer. A solution of 10% Dextran was spin coated (3000 rpm) on a blank silicon wafer that was exposed to oxygen plasma for 3 min to enhance the hydrophilicity of the wafer. Then, an SU8 layer was spin coated (Figure 5.1 (a)) and patterned ((Figure 5.1 (b)) by UV lithography on the Dextran layer. The geometry of the electrode patterns and their dimensions on the photomask were shown in the Figure 5.2. A piece of thermal release tape (TRT) (Nitto Denko, No3198MS) was used to transfer the membrane to a thin (flat and curved) PMMA substrate (0.3 mm thick) before (Figure 5.1 (c)) and after (Figure 5.1 (d)) dissolution of Dextran in water. Figure 5.1 (e1, f1, g1) and Figure 5.1 (e2, f2, g2) show the placement of the membrane on the substrate, detachment of the thermal release tape from the membrane by heating (to 110°C) and a thin (~50 nm) platinum deposition and membrane lift-off on flat and bent substrates, respectively. The heat for separating the TRT from the membranes was provided by a hot plate and a hot air gun for the flat and bent substrates, respectively. The TRT works as a supporting structure to

hold the fragile parts of the membrane that were more prone to move or break specially for the thinner membranes. Two variables (i.e. stencil membrane thickness and curvature of the substrate) were considered to study the consistency of the technique in microelectrodes fabrication. Two samples were prepared by the process shown in Figure 5.1 for each of the two SU8 membrane thicknesses of 15 µm and 2 µm on flat and bent substrates to investigate the properties of the electrodes fabricated using thick and thin membranes.

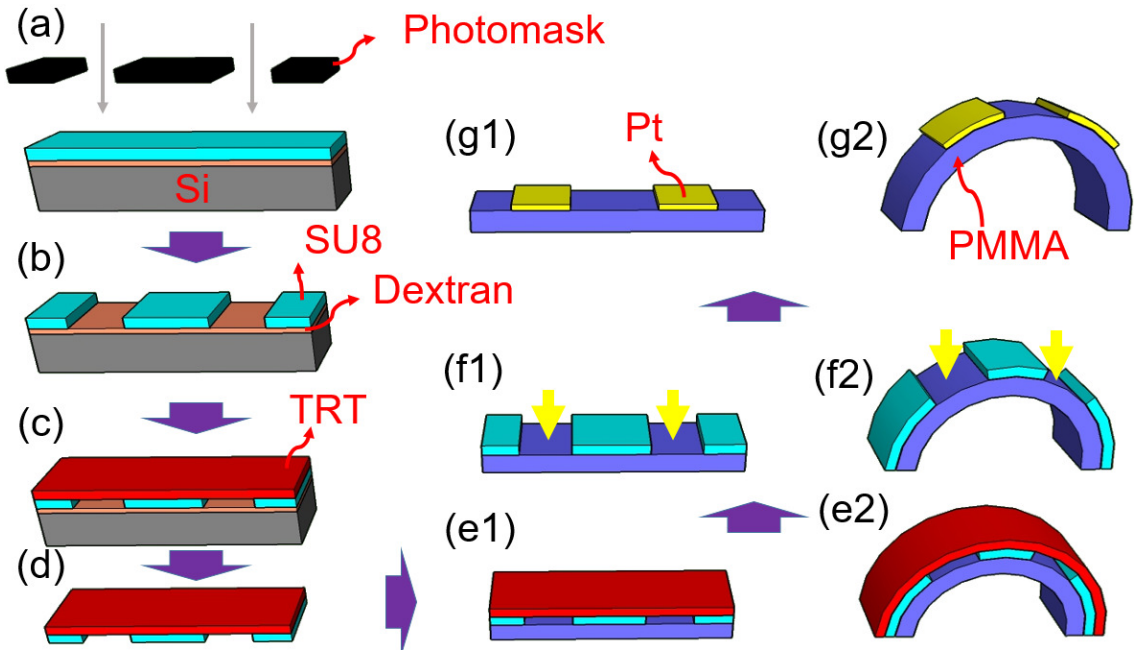

Figure 5.1. Fabrication flow after coating the Dextran and SU8 layers on the silicon wafer including (a, b) patterning the SU8 membrane by photolithography, (c) attachment of the TRT to the membrane, (d) dissolution of the Dextran, (e) placement of the membrane on (e1) flat or (e2) curved substrates, (f1, f2) detachment of the TRT and platinum deposition on the flat and curved substrates and (g1, g2) lift-off the membrane.

5.3. Results and discussion

Figure 5.3 shows the schematics showing a comparison when stencil masks made in thick (a) and thin (b) membranes on both flat and curved substrates. An inverse proportional relationship between the flexibility (compliance) of the stencil membrane and the gap distance between the membrane and the substrate is previously reported [219]. A thin membrane has a better compliance and hence a lower gap distance with both flat and curved substrates than the thick membrane. Since the membrane gap distance with the substrate is proportional with the

blurring [217], the thin membrane is more able than the thick membrane to reduce the blurring effects from the electrode patterns on both flat and curved substrates. Less blurring corresponds with higher consistency of the electrode patterns. On the other side, the low adhesion of the thick membrane to the highly curved substrates makes it unstable while using as stencil masks over curved substrates.

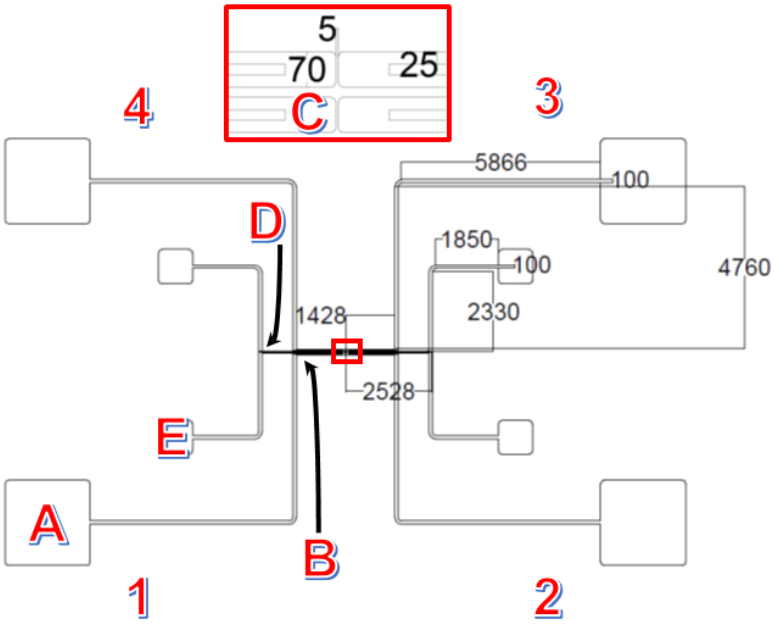

Figure 5.2. Dimensions of the electrode patterns on the photomask.

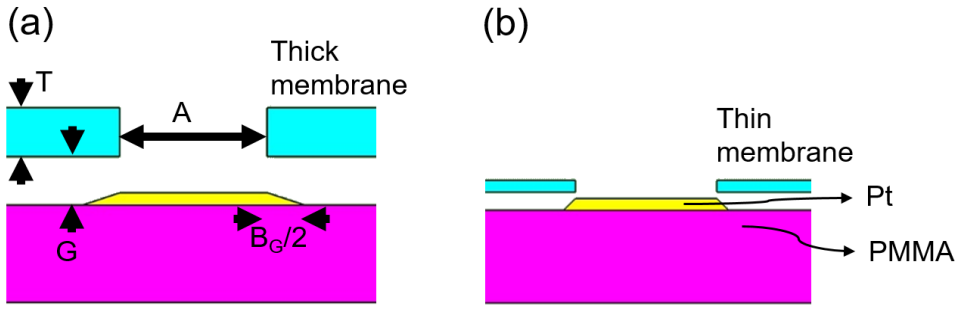

Figure 5.3. Stencil masks made in thick (a) and thin (b) membranes on flat substrates. The stencil aperture width (A), blurring due to the geometry (B_G) and gap distance between the membrane stencil and substrate (G) were shown.

Figure 5.4 shows the optical micrographs of the membranes (a-c), the deposited electrodes after lift-off (d-f), and the big pictures of the thin membrane (g) and the electrode fabricated by the thin membrane (h) on the curved substrate. Using Figures 5.4 (a-c), the stencil

aperture width (A) was measured for different thicknesses of the membrane (T) for all of the samples. Likewise, the blurring due to the geometry plus by the stencil aperture width ($A+B_G$) was measured from the Figure 5.4 (d-f). Thus, we could calculate the blurring due to the geometry (B_G) for each sample by subtracting the two previously measured data. Having A and B_G we were able to calculate the gap distance between the membrane stencil and substrate (G) using the equation (1) [217]:

$$G = \frac{B_G D}{S} \tag{1}$$

If S>>A and D, G >> T, in which, S is the source diameter and D is the distance between the sputter machine source and the substrate [217].

Figure 5.4(a) and Figure 5.4(b) present the thick membrane (T=15 µm) and the corresponding sputtered electrodes via the thick membrane on a flat substrate. The high edge roughness of the thick membrane and corresponding electrodes can be correlated to the photolithography limitations (that is the UV light deviation through the thicker photoresist layers) for the thick photoresist layers and higher blurring. In addition to the high edge roughness of the thick membrane, the applied normal bending stress to the membrane during the transfer process using the TRT (Figure 5.1 (d)) caused a rupture in one of the two fragile ~5 µm bridge parts of the membrane. The low adhesion of the thick membrane to the curved substrates, prevented us to fabricate the electrodes on the curved substrates using the thick membranes. Figure 5.4(b) and Figure 5.4(e) show the thin membrane (T= 2 µm) and the resulting sputtered electrode on the flat substrate. Based on the optical micrographs, the thin membrane evidently had a lower edge roughness as well as a lower applied normal bending stress during the membrane transfer process using the TRT in comparing to the thick membrane. In contrast with the thick membrane, the thin membrane could conform and attach well to the curved substrates before the sputtering process. Figure 5.4(g) shows the thin membrane (T= 2 µm) on a curved substrate with 1 cm radius of curvature before the platinum

deposition. The optical micrograph showed a proper adhesion of the several areas of the membrane to the PMMA substrate. Figure 5.4(h) shows the micro electrodes on the same substrate after the platinum deposition and lift-off. Our observation from the optical micrographs showed the high precision of the patterns transferred from the thin membrane to the highly curved substrates. Electrodes from thin membranes had significantly lower edge roughness (partially due to less blurring) and no rupture due to tensile stress similar to the ones from thick membranes during the transfer using TRT. The thin membrane made consistent electrode patterns on flat and curved substrates while the thick membranes could not stable on (or adhere to) the curved substrates.

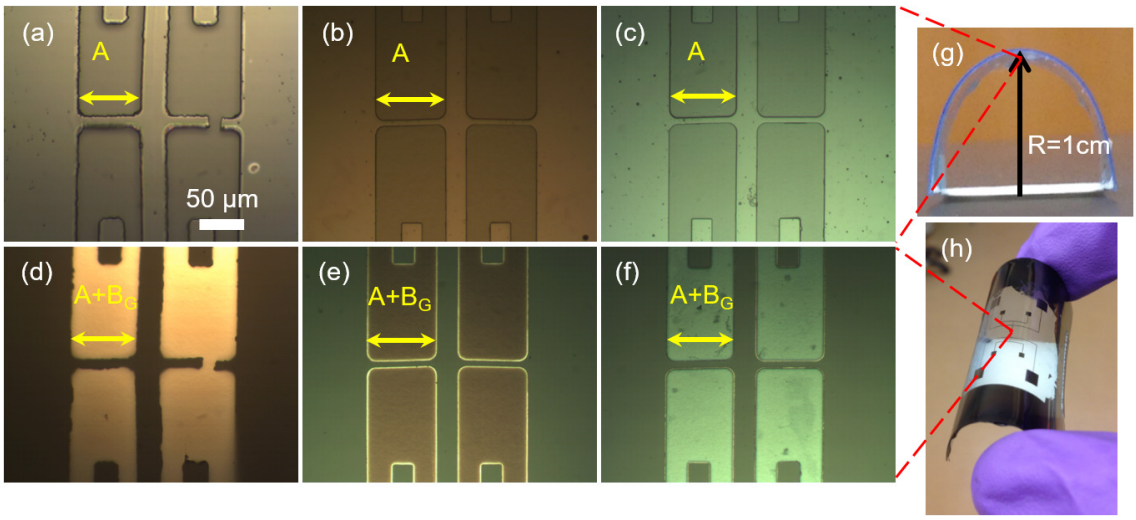

Figure 5.4. Optical micrographs of the (a-c) membrane and (d-f) their corresponding electrodes after the Pt deposition and lift-off for the (a) thick membrane on flat substrate, thin membrane on (b) flat and (c) curved substrates and (c, f, i) their corresponding sputtered electrodes. (g) is the big picture of the thin membrane and (h) electrodes on the curved substrate after deposition and lift-off.

In order to study the blurring issue, we calculated the blurring due to the geometry (B_G) using the gap distance between the membrane stencil and substrate (G) values from the Equation (1). The sputter source diameter was (S=59 mm) for both flat and curved substrates while the distance between the source and flat substrate was (D=39 mm) and the one for the top area of the curved substrate (where shown in Figure 5.4(h) and used for the calculations) was (D=29 mm). Table 5.1 shows the summary of the B_G and calculated G from the equation

(1), for the four electrodes on the two samples fabricated by the thick and thin membranes on the flat and curved substrates. Overall, the values of blurring (B_G) as well as the distance between the thin membrane and the substrate (G) for the flat and curved substrates were close to each other and remained below 1 μm on the whole patterned areas. In contrast, the blurring value of the electrodes made by the thick membrane was ~5 μm close to the smallest feature transferred to the stencil membranes by photolithography. Also, the gap distance between the thick stencil membrane and the substrate was above 3 μm. The high gap distance between the thick stencil membrane and the substrate prevented the proper adhesion thus the usage of these membranes on the curved substrate.

Table 5.1. Summary of the statistics of the measured BG and calculated G of all four electrodes of the two samples used for the thick membrane on the flat substrates and the thin membrane on the flat and curved substrates

	B_G (μm)		G (μm)	
	Flat	Curved	Flat	Curved
Thick membrane	4.9 ± 0.5	N/A	3.3 ± 0.3	N/A
Thin membrane	0.8 ± 0.3	0.9 ± 0.4	0.5 ± 0.2	0.6 ± 0.4

In order to determine the electrical properties of the fabricated electrodes made by the thin membrane on flat and curved substrates, we measured the electrical resistance of the four electrodes of the two samples for the flat and bent substrates. Table 5.2 shows the summary of these data. The resistance values of the flat electrodes were close to the ones for the curved electrodes (~15% different). This showed the fidelity of this technique to fabricate electrodes with consistent electrical properties on highly curved electronics. The higher standard deviation of the bent substrates (9.3 vs 2.6 kΩ) could be correlated with the several distances that the bent substrates have from the sputtering machine source on the different locations of the substrates. This also resulted in the higher standard deviation of the blurring and the gap

distance for the curved substrates (G) in comparison with the flat substrates. In order to better study the effect of gap distance (G) on the resistance (R) of the microelectrode one can use the equation (2):

$$R = \frac{\rho L}{t \times (A + B_G)} \quad (2)$$

In which, L, t, A and B_G represent the length, thickness, width and blurring of the microelectrodes and ρ represents the resistivity of the sputtered Pt. Equation (3) can be used to find the relationship between the G and R by simplifying the Equations (1) and (2):

$$R = \frac{\rho L D}{t \times (AD + GS)} \quad (3)$$

In order to find the deviation of the resistance of the microelectrodes on the curved substrates compared to the one on flat substrates, we defined the electrodes resistance deviation factor (α) from the equation (4):

$$\alpha = 100 \times (1 - \frac{R_C}{R_F}) \quad (4)$$

In which, R_F and R_C are the resistance of the microelectrodes on flat and curved substrates, respectively. Using the equation (3), the equation (4) could be simplified to find the electrodes resistance deviation factor (α) in terms of the gap distance (G) form the equation (5):

$$\alpha = 100 \times (1 - \frac{AD + G_F S}{AD + G_C S}) \quad (4)$$

Table 5.3. shows the results of the resistance measured and calculated deviation factor from the equation (4) on flat and curved substrates for the samples from thin membranes. For the calculated value, since the widths of the electrodes were not constant, an average value (A=62 μm) was used for these calculations. Overall, the resistance deviation factor due to blurring for the thin membrane remained below 15%. This shows the consistency of the method in fabricating microelectrodes on flat and curved substrates with similar electrical resistance.

Table 5.2. Electrical conductance and resistance of all four electrodes of the two samples used for the thin membrane on flat and curved substrates.

	G (μm)		R (kΩ)		α (%)	
	Flat	Curved	Flat	Curved	Geometry (formula)	Measured
Thin membrane	0.5 ± 0.2	0.6 ± 0.4	73.1 ± 2.6	62.4 ± 9.3	1	15

5.4. Conclusions

A novel technique is introduced to fabricate highly consistent (less than 1 μm blurring at different locations) electrodes on curved substrates that employs flexible polymer stencil masks. Comparing to the previous techniques to use the polymer stencil masks for the electrode fabrication, this technique has the ability to transfer thin membranes (down to 2 μm) having large patterned area (1.5 cm × 1.5 cm), long through holes (0.8 cm) and small minimum feature sizes (5 μm) which are more difficult to transfer because of their high planar aspect ratios. The technique also reduced the blurring on flat substrates more than 80% by using thin stencil membranes instead of thick ones. The consistency of the method (above 85%) in fabricating electrodes on flat and curved substrates was demonstrated using thin stencil membranes. In summary, the technique presented in this study can be implemented in the electronic fabrication process on highly unconventional and curved substrates with high precision.

Chapter 6. Placement Of Single Nanowires On Microelectrodes In Target Plastic Substrate

6.1. Introduction

Characterizing electrical properties of individual metal nanowires is a key to the development of the nanowire electrodes based flexible transparent electronics [228]. Therefore, alignment and integration of single nanowires into external electrodes formed on plastic substrates is required [229]. Techniques to align single nanowire for electrical transport measurements are divided into laser [229, 230], nanomanipulator [231, 232] and microchip [233] techniques. The optical methods are non-destructive and compatible with various setup configurations. However, they mostly have a maximum resolution limitation depending on the light wavelength they use and they also require prefabricated electrical contacts integrated with the nanowire [230]. Nanomanipulators connected to tungsten and nichrome tips have the ability to measure the nanowires resistivity within their fabrication template which preserve the nanowire from oxidation or damage. The nanowire diameter has to be larger than the tip size and it should be accessible to the tip while the small contact between the nanowire and the tip increases the contact resistance [232]. Microchips with micro/nanoscale electrodes can measure the electrical properties of the nanowires with the diameter scales down to few nanometers. Thus, they are used as the most reliable method to measure the electrical properties of the nanowires beside their complicated fabrication process [234].

The main three approaches to fabricate contacts to nanowires using microchips are as follows: The first group disperses the nanowires on an insulating substrate and then makes the metallic contacts using photolithography [234], focused ion beam (FIB) [235] or electron beam lithography (EBL) [236]. In this way, the nanowire alignment is not required, however, the contacts should be aligned with the dispersed single nanowires [237-241]. The fabricated microchip cannot be reused with this method, and the nanowire as well as the substrate (especially polymer) might be damaged during the electrodes fabrication (etching, heating,

etc.) processes [242]. Also the spatial spread of metal (platinum) should be controlled to prevent making a metallic halo or even a shortcut between the two metal contacts [238]. The second group uses the electrofluidic alignment of nanowires on prefabricated metal contacts. The advantage of using this method is producing metal-nanowire contacts without implementing complicated nanowire/contact alignment processes. The necessity to employ microfluidics with the electric alignment and a post process (e.g. annealing or metal deposition, etc.) to increase the metal-nanowire contact are the obstacles of this group [243-245]. The last group use nanomanipulators usually used inside scanning electron microscope (SEM) in vacuum to pick and place single nanowires on prefabricated metal electrodes. In this way, high precision alignment can be employed although the complicated pick and place of the nanowire is usually combined with the cutting or shortening of the nanowire and an additional metal deposition is required using the FIB to enhance the electrode-nanowire contact. Thus, high control over the deposition process is required while the ions (e.g. Ga) in this process can induce impurity, damage or roughness to the nanowires surface [238, 246].

In order to place a nanowire on the nanochannel flight tube mentioned in the first chapter and connect it to an electrode pair, a single nanowire alignment and placement technique into the target nanochannel on plastic substrates is required. Not only the technique has to be compatible with plastic substrates (containing micro-/nanochannel features) and place the nanowires in dry medium but the placement accuracy is also important. In this chapter, we developed a precise alignment, transfer and electrical measurement technique of single nanowires on prefabricated metallic microelectrodes on flexible and transparent poly methyl methacrylate (PMMA) substrates. Optical microscope-based observation and alignment in ambient conditions and reusability of the microchips for connecting to different nanowires makes the process low cost and high throughput. Also, the thermal transfer of the nanowires

ensures the full contact between the nanowire and metal electrodes and enables the fabrication of mechanically/electrically stable and embedded nanowire-microelectrode based electronics.

6.2. Experimental

6.2.1. Nanowires fabrication and electromagnetic alignment

FeNiCo composite nanowires were pulsed electrodeposited in a nanoporous alumina template with 0.2 μm diameter pores and up to 30 μm in length. The nanowires were separated by dissolving their alumina template in a 2 M NaOH solution overnight and rinsing with water and ethanol three times. Electromagnetic alignment was used to deposit and align the nanowires on blank PMMA substrates to improve separation and reorientation of the single nanowires on a dry medium before using them for the next steps. A 7.5 cm × 3 cm × 1 cm steel core ($\mu = 4\pi \times 10^{-7}$ H/m, L = 7.5cm, M_s = 1,708,658 Wb/m^2) was used to make an electromagnet. Here, μ, L, and M_s represent permittivity of the vacuum, coiled length of the electromagnet and spontaneous magnetization of the electromagnet's core material, respectively. A tinned copper wire was used to make the number of coils around the core (N = 71). A magnetic field strength of 70 Oe was used to align the nanowires disposed of a 10 μL nanowire solution from the bottom of the couvette on blank PMMA (2.5×2.5 cm) substrates.

6.2.2. Fabrication of nanochannel on plastic substrate

A nanochannel with ~200 nm diameter and two nanopores ~20 nm diameter was milled on a silicon substrate using Focused Ion Beam (FIB) in my group. The nanochannel patterns from the silicon substrate were copied into Poly Urethane Acrylate (PUA) on Polycarbonates (PC) substrates using Ultraviolet (UV) lithography and then copied from the PUA molds into Poly methyl methacrylate (PMMA) substrates using Nano Imprint Lithography (NIL, Obducat).

6.2.3. Single nanowires alignment and placement

Figure 6.1 shows the schematics of the alignment process steps of single nanowire on the nanochannel substrate. After the electromagnetic alignment shown in Figure 6.1(a, b),

contact between the PMMA and a PDMS substrates was used to transfer the nanowires to the PDMS substrate shown in Figure 6.1(c). Repeating this process further using new PDMS substrates helps avoid the nanowires agglomerates or the residual template particles in the nanowires solution. Figure 6.1(d) shows a single nanowire selected on the PDMS substrate to align with the nanochannel shown in the Figure 6.1(e). Figure 6.1(f) shows next step in which the nanowire and nanochannel were aligned using an optical microscope-based alignment setup. Then, the two PDMS and PMMA substrates were pressed while applying temperature to the PMMA substrate to transfer the nanowire from the PDMS substrate to the nanochannel on PMMA substrate. Figure 6.1(g) shows the schematics of this process done by nanoimprint lithography (Obducat NIL) at 100°C, 45 bar for 5 minutes and demolding at 70°C. After separation of the PDMS substrate in the last step shown in Figure 6.1(h), the placed single nanowires were inspected by an optical microscope to obtain the alignment accuracy.

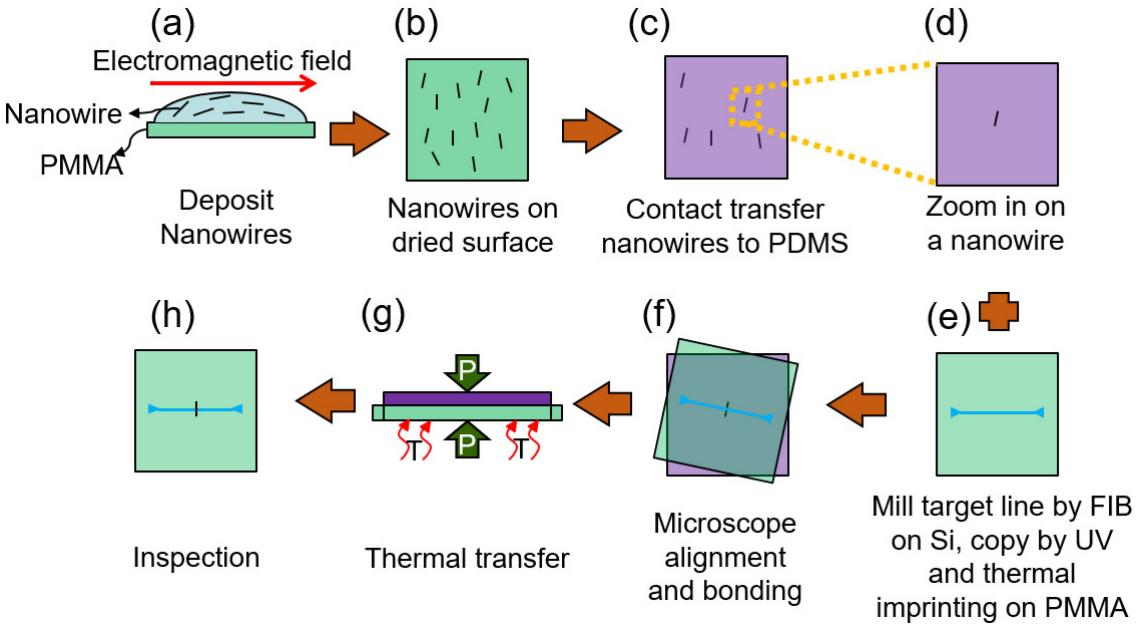

Figure 6.1. Single nanowire alignment process flow (a) electromagnetic alignment, (b) nanowires on the dried surface after the electromagnetic alignment, (c) nanowires transferred to PDMS substrate, (d) selected nanowire on the PDMS substrate, (e) nanochannel on PMMA substrate, (f) the alignment between the nanowire and nanochannel, (g) thermal transfer of the nanowire to the PMMA substrate and (h) removal of the PDMS substrate and inspection.

6.2.4. Single nanowire alignment setup and methods

An optical microscope-based nanowire alignment setup was built for the experiments to allow a high accuracy alignment of single nanowires in ambient conditions. Figure 6.2 (a, b) show the schematics of the alignment setup and the alignment steps, respectively. The alignment setup consists of a long distance (1 cm, 40X) objective Nikon microscope, a micro-positioning stage (miniature XYZ positioner) [247] and a holder. The micro-positioning stage consisted of a stationary stage and a moving stage controlled by three piezo driven step motors in the three (xyz) directions. The stationary stage was installed on the microscope stage which moves only in z direction. The moving stage held position without power and it had a travel distance of up to 10 mm with the resolution of 10 nm driven by a USB controller CF30. A steel rotary disc with 10 mm in diameter was attached to the top surface of the moving stage to add the rotation freedom to the substrate on the moving stage. The holder substrate was a 76 mm×76 mm flat Teflon plate with 2 mm thickness having a 50mm × 25mm through hole. The holder could be installed and removed from the microscope stage which moved in xyz directions. Two PMMA stands made 6 mm space between the microscope moving stage in xyz directions and the holder bottom surface.

Figure 6.2 (b-e) show the schematics of the process steps to align a nanowire over a PDMS substrate carried by the moving stage of the positioner with the nanochannel on a PMMA substrate carried by the holder. The transparent nanochannel PMMA substrate allowed the observation of the nanowire on the PDMS substrate during the alignment while the PDMS substrate enabled a temporary PMMA-PDMS bonding after the alignment and before the thermal transfer of the nanowire to the electrode on PMMA substrate. In the first step of the alignment, a single nanowire on the PDMS substrate was brought to the focus of the microscope lens manually by changing the position of the substrate using the positioner moving stage. Putting the nanowire close to the center of the microscope view simplified finding the nanowire

in the next steps. In the second step, the electrode substrate was placed on the holder while the electrodes faced to the nanowire and the two features were aligned by repetitively focusing on the nanowire and electrodes and moving the microscope and micro-positioner moving stages. After that, the nanowire and the electrode substrates were brought into contact with each other by elevating the positioner moving stage in the third step. A proper alignment was achieved by repeating the second and third steps. In the last step, the holder was removed and the PMMA and PDMS substrates were temporarily bonded by slightly pressing the two substrates between the microscope lens (or nosepiece) and micro-positioner moving stage.

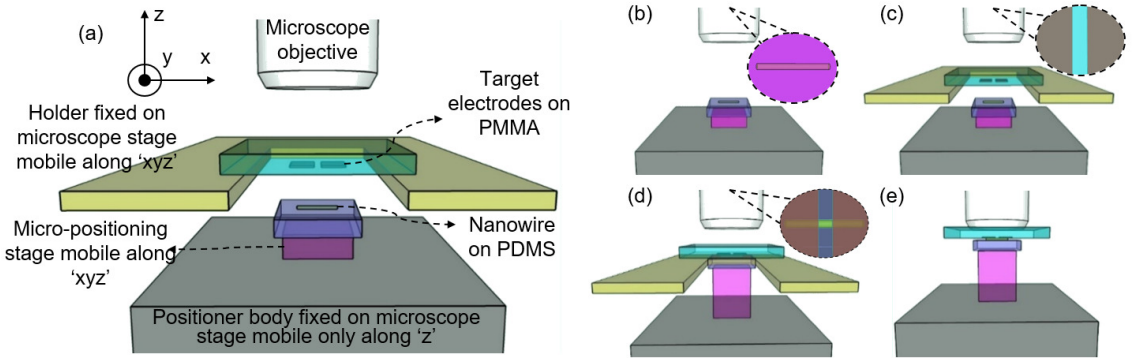

Figure 6.2. Schematics of the microscope alignment (a) setup, (b) zoom on the nanowire, (c) zoom on the nanochannel, (d) zoom on the nanowire after putting on the nanochannel and (e) gently press the two substrates between the microscope head and positioner moving stage.

6.3. Results and discussion

6.3.1. Nanowire alignment

The microscope alignment setup and the optical micrographs of a nanowire and a nanochannel during the alignment are shown in Figure 6.3 (a-d). (a) shows the alignment setup consisting of the top substrate on the holder over the microscope stage and bottom substrate with the rotary disc on the positioner moving stage. Figures 6.3(b-d) show a nanowire and a nanochannel optical micrographs at the microscope alignment stages shown in the Figure 6.2. The nanowire and nanochannel positions (or relative positions) were highlighted by red ovals and yellow lines in these figures. Figure 6.3(b) shows the nanowire on PDMS substrate placed on the positioner moving stage. Since the nanochannel substrate was located between the

microscope objective and the nanowire, the image is not fully clear. The micrograph of the nanochannel from the back side of the substrate is shown in the Figure 6.3(c). Figures 6.3(b, c) show the nanowire and nanochannel before bonding and Figure 6.3(d) shows the nanowire and nanochannel in contact with each other after bonding (gently pressing) the two substrates. From the optical micrograph shown in Figure 6.3(b), one could barely identify whether this is one nanowire or two nanowires attached to each other. Also, the visibility of the nanowire in the Figure 6.3(d) was low after bonding the two substrates. Using a higher resolution long distance objective and looking at the nanowires through the PDMS substrate after the bonding could be the possible solution for the first and second problems.

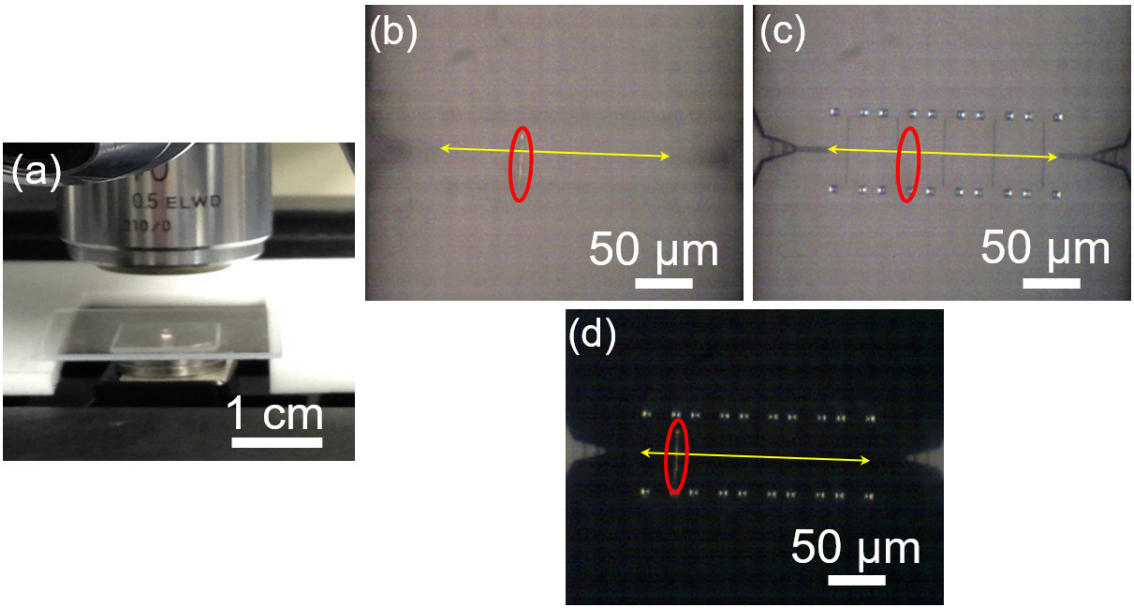

Figure 6.3. (a) microscope alignment setup and optical micrographs of (b) an FeNiCo nanowire on PDMS (bottom) substrate, (c) nanochannel on (top) PMMA substrate and (d) the nanowire and nanochannel after temporary bonding between the PDMS and PMMA substrates.

6.3.2. Nanowires alignment accuracy

The accuracy of the nanowires placement was measured from twelve nanowires aligned using the technique explained in the Figure 6.4. Figure 6.4 shows the schematics of the a perfect and an imperfect nanowire alignment (a) and two sample nanowires with rotational (b) and translational (c) misalignments. In the Figure 6.4(a) a perfect alignment was defined as the nanowire center on the nanochannel and 90° angle between the nanowire and the nanochannel

directions. Thus, assuming the nanowire length (L_N), and the angle between the nanowire and nanochannel (θ) and distance of the nanowire center from the nanochannel (d), the translational and rotational misalignments were defined by (d) and (90-θ), respectively. The translational misalignment can be defined by (d/ (LN/2)) ×100 in percent of the total length of the nanowire. The translational and rotational misalignments calculated for twelve nanowire samples were 3.9 µm ± 2.8 µm and 3.3º ± 2.9º, respectively. The translational misalignments of 25% of the nanowires were below 1µm and 33.33% of the nanowires had no rotational misalignment, which make this technique a viable alternative for the submicron alignment of the nanowire.

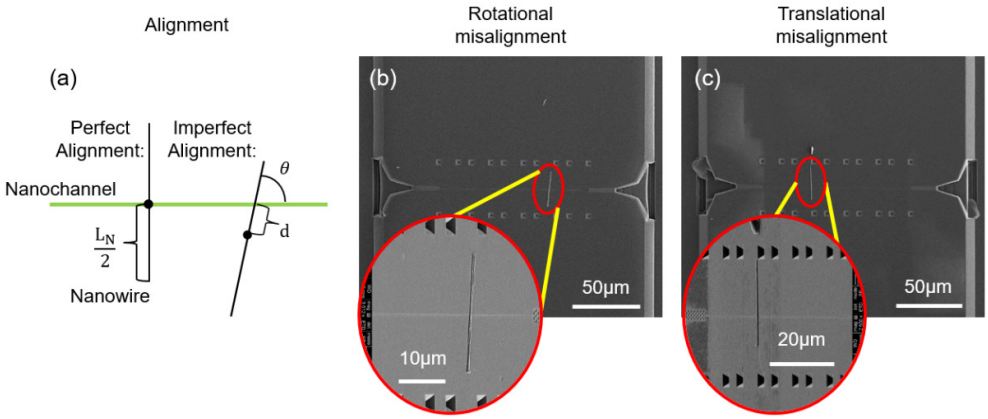

Figure 6.4. (a) Schematics of the perfect and imperfect alignment definition, (b) Scanning Electron Microscope (SEM) image of a nanowire transferred with rotational misalignment and (c) SEM image of a nanowire transferred with translational misalignment. The insets show the magnified images of the nanowires at the intersection with the nanochannel.

6.3.3. Optimizing nanowires transfer rate vs temperature

In order to determine the proper temperature for the thermal bonding process shown in Figure 6.1(g), we studied the success rate of the aligned transfer of the nanowires to the nanochannel at four different temperatures. Figure 6.5 shows the results of this study for four temperature groups in which three samples were used. The imprinting pressure and time were 35 bar and 5 min for all samples. At 70ºC no nanowire was transferred to the target nanochannel and at 80ºC the transfer was successful only for one sample out of four trials. At 90ºC and 110ºC the aligned nanowire was transferred to the target nanochannel for all samples. However, at 110ºC, where the PMMA substrate passed the glass transition temperature, the nanochannel

was deformed. Therefore, the 90ºC was selected as the suitable temperature for the thermal transfer process without damaging the nanochannel structure.

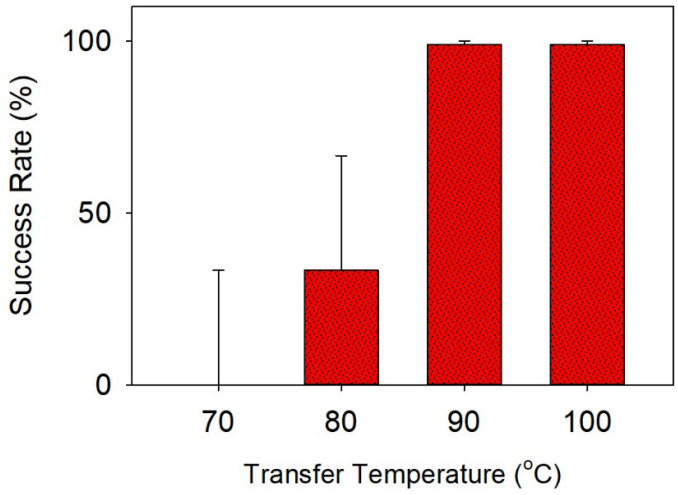

Figure 6.5. The success rate (ratio of the number of nanowires transferred to the total number of nanowires) of the thermal transfer at different transfer temperatures.

6.3.4. Transferred nanowire and nanochannel configuration

Figure 6.6(a, b) and their insets show the magnified SEM images of the top and side views of an aligned nanowire which was transferred to the nanochannel substrate with the thermal imprinting conditions of 90ºC, 35 bar and 5 min. The images show that the nanowire consisted of more than one nanowire attached to each other from sides and tails. Also, they show that the placement technique pressed a 600 nm diameter nanowire ~44 nm into the nanochannel. Therefore, it can be used to fabricate nanowire based partially embedded nanoelectrodes. From the SEM images observations, the nanochannel had no deformation during the thermal transfer that is required for the fabrication of the nanoelectrode integrated with the nanofludics.

6.4. Conclusion

A facile technique to align and place single nanowires from a source substrate to a nanoscale feature on plastic substrates with micron level accuracy was introduced. Compared to the alignment methods in the literature in SEM chambers that required automated

manipulators and vacuum conditions [238, 246], this technique performed the alignment in ambient conditions providing the ability to observe the nanochannel and nanowire in each step during the alignment. Using this technique, the average translational and rotational misalignments of the nanowires were less than 4 µm and 4°, respectively. Submicron translational alignment accuracy for 25% of the nanowires and perfect rotational alignment for 33.33% of the nanowires was observed using this technique. The transfer success rate of the nanowire increased by increasing the temperature. However, using high temperatures could damage the nanochannel features on the target substrates. This technique has the potential to integrate nanoelectrodes with the nanofluidic structures on plastic substrates with high throughput.

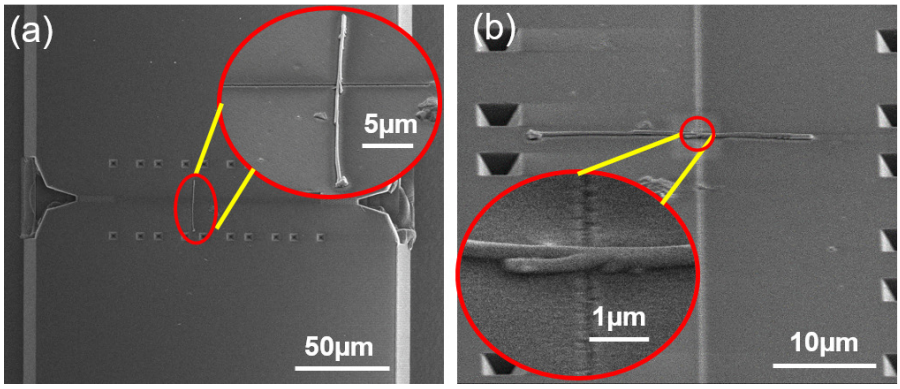

Figure 6.6. SEM images of the nanowire-nanochannel configurations from (a) top and (b) side views. Insets show the magnified images of the nanowire at the intersection with the nanochannel.

Chapter 7. Control Of Electrical Properties Via Single Core-Shell Nanowires

7.1. Introduction

Transparent and flexible electronics are the crucial elements of smart phones/glass, touch screens, liquid crystal display (LCD), organic light-emitting diodes (OLED) and transparent electrodes [248, 249]. Indium Tin Oxide (ITO), a conventional material used as transparent conductor, is a fragile and expensive material with restricted resources [250]. Other alternatives such as conducting polymers [251], carbon nanotubes (CNTs) [252] and graphene [253] which provide higher mechanical flexibility and durability, are not capable of carrying high currents and similar performance to those of ITO [228]. Metal nanowires which can be divided into homogenous and heterogeneous nanowires based on their material structure, are great alternatives to the above mentioned transparent conductors because of their high performance (electrical conductivity, mechanical strength, oxidation/corrosion tolerance, etc.) [254] and transfer rate controllability to the final device substrate [228]. Among the homogenous nanowires, silver nanowires have excellent flexibility as well as electrical and optical properties [255, 256] but they are limited to low availability, high cost [228] and low controllability over the mechanical strength [257]. On the other side, copper nanowires are more available and less expensive than the silver nanowires among the homogenous nanowires [258, 259]. While their electrical conductivity is only 6% less than silver nanowires [254], the main disadvantage of using the copper nanowires is their high oxidation and corrosion potential which leads to elevated electrical resistance [260]. Heterogeneous or core-shell nanowires can provide the benefits of more than one homogenous nanowire material and reveal unique properties to solve the drawbacks of the homogenous nanowires [79]. For example, silver core silver-palladium shell nanowires have higher mechanical strength than the one of silver nanowires which makes the nanowire more resistant to breakage or bending. While the length of the current nanowires of this type is still limited to 20 µm, their core material mostly (92.2%)

consists of silver which makes their price as high as the homogenous silver nanowires [261]. Another example of core shell nanowires is copper-graphene nanowires which are more resistant to oxidation and their electrical properties are superior to those of copper nanowires. The high synthesis temperature of the graphene using thermal chemical vapor deposition limits the fabrication process of these nanowires to low temperature chemical vapor deposition but the core shell nanowire still oxidizes with a lower rate (9% increased resistivity in a month) [262]. Copper-aluminum doped zinc oxide (AZO) core-shell nanowires use a conformal metal oxide coating (AZO) using atomic layer deposition (ALD). Although the conformal coating enhances the nanowires tolerance against oxidation, the electrical resistance of the assembled nanowires device increases by 18% at higher temperatures. Also the mechanical strength of these nanowires was not improved by the coating thus deformed and connected nanowires were observed [263]. As the last example of core-shell nanowires, the copper-copper nickel core-shell nanowires has the highest endurance against oxidation than the above copper core nanowire examples. The complicated solution based processes including the electroless plating and dip coating as well as the nanowires length limitation to 20 μm are the downsides of these nanowires [260].

The nanowires used as transverse nanoelectrodes for the nanochannel-nanopores device explained in the first chapter should have enough mechanical strength (hardness) and controllable electrical resistance to control the total resistance of the sensing circuits of the final device. Thus, a core-shell nanowire with a mechanically strong core and a highly conductive and chemically stable shell is required. In this chapter, we introduced a novel iron-nickel-cobalt-gold (FeNiCo-Au) core-shell nanowire with high mechanical strength and electrical transport properties. While the iron-nickel-cobalt core maintains the high mechanical strength of the iron, nickel and cobalt alloys (around two times higher than the one for the highly conductive materials e.g. gold, silver and copper), the gold shell provides a high electrical

conductivity (ITO level performance [228]) and endurance against oxidation and corrosion. Thus, the iron nickel cobalt nanowire with gold shell is one of the best choices to fabricate long and mechanically stable nanowires with high electrical conductivity. More importantly, the resistivity calculation of the shell segment of the new core-shell nanowires introduces an efficient method to measure the electrical resistivity of very thin (or different thicknesses) metal shells on these nanowires. The significance of such measurement determining the electrical properties of the gold coated nanowires and at the same time dependence of the metallic nanowires electrical [264-266] and mechanical [267-270] properties on their diameter and the very challenging processes of fabrication, manipulation and resistivity measurement of very thin nanowires (less than 10 nm diameter).

7.2. Experimental

7.2.1. FeNiCo and FeNiCo-Au nanowires fabrication and preparation

Two sets of FeNiCo and two sets of FeNiCo-Au nanowires were fabricated for these experiments. The first group were fabricated for the initial electrical characterization of the core-shell nanowires while the second group were aimed toward finding the optimized conditions of the Au deposition on the core-shell nanowires. Figure 7.1 (a-c) show the schematics of the process steps to fabricate the FeNiCo and FeNiCo-Au nanowires. An oxide layer was formed and thickened over the FeNiCo nanowires when they were exposed to NaOH solution and air before electrical measurements. Likewise, an oxide layer was initiated on the FeNiCo nanowires before coating the gold shell. Therefore, the thickness of the oxide layer between the FeNiCo core and gold shell was presumably less than the one on the FeNiCo nanowires before the electrical measurement.

The first group of FeNiCo composite nanowires with 0.2 μm diameter and up to 40 μm length were fabricated by pulse electrodeposition and grown in a porous alumina template. Details of the electrodeposition process can be found in [271]. After the electrodeposition, the alumina template was dissolved by soaking the template in 2 M NaOH solution within a

couvette overnight. The nanowires were then rinsed with NaOH, water and ethanol three times. After dissolving the alumina template, the nanowires were kept in ethanol to prevent oxidation. Some of the nanowires were broken during the preparation process, so that the nanowires had different lengths. For the FeNiCo-Au core-shell nanowires the same procedure was followed by removing the ethanol, soaking the nanowires in a 1:3 gold to DI water solution and centrifuge at 3000 rpm for 3 minutes. The gold solution was removed, and the nanowires were kept in ethanol afterwards.

The second group of FeNiCo nanowires were fabricated in alumina template with the pore diameter of 200 nm in which the nanowires were grown up to 60 μm length using DC electrodeposition (V= -1.19 V) in an electrolyte solution (containing 0.72 M $NiSO_4$, 0.155 M $FeSO_4$, 0.005 M $CoSO_4$, 0.5 M H_3BO_3, 0.011 M $C_6H_8O_6$, 0.001 M Sodium lauryl sulfate (SLS)) for around 6800s. Based on XRD data, the FeNiCo nanowires prepared in this way include (68±3% Fe, 29±2% Ni and 3±0.1% Co) in their structure. Figure 7.1(c) shows the nanowires after the dissolution of their alumina template in 2 M NaOH overnight followed by additional rinsing in NaOH, water and ethanol for three times. Like the first group, because of the presence of the oxygen molecules in the NaOH etchant solution, a thin layer of oxide was grown on the FeNiCo nanowires after dissolution of their template. However, we refer to FeNiCo-Oxide core-shell nanowires as pure FeNiCo nanowires in the continue of the chapter. It should be mentioned that removal of the oxide layer from the FeNiCo nanowires was almost an impossible task because of the difficulties of the etching control of the oxide layer by the common etchants (e.g. HF based or chloride-based etchants). The FeNiCo nanowires were coated with Au shell after dipping in 0.01 M $KAuCl_4$ solution for which the pH was controlled by adding HCl. For these experiments, the pH of the solution and the dipping time were variables to find the optimum Au coating conditions that will be explained in the continue of this chapter.

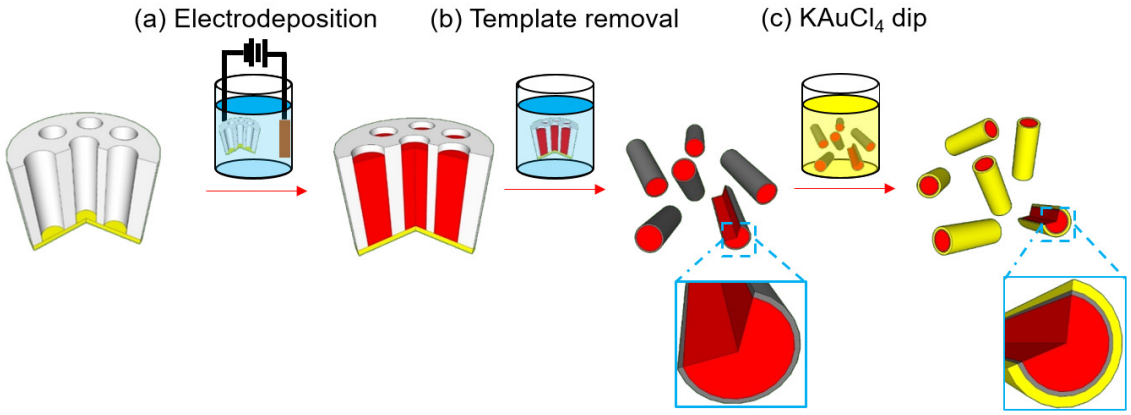

Figure 7.1. The fabrication flow of FeNiCo-Au nanowires starting with (a) gold sputtered alumina porous membrane, then electrodeposition into the membrane which produces (b) FeNiCo nanowire inside the membrane pores. Removal of the membrane by NaOH provides the (c) separated FeNiCo nanowires with thin oxide layer with a zoomed in cross section inset followed by dipping the separated nanowires in $KAuCl_4$ which fabricates the (d) FeNiCo-Au nanowires with a zoomed in cross section inset.

7.2.2. Microelectrodes fabrication on plastic substrates

We used stencil lithography by the polymer masks to fabricate microelectrode arrays on the PMMA substrates. This allowed a facile fabrication of microelectrodes on PMMA substrate without damaging the substrates (e.g. changing the transparency of the PMMA). Figure 6.1 of the supporting information shows the schematics and the corresponding optical images of the process. A membrane was fabricated by photolithography on SU8 resist over a thin layer (250 nm) of water soluble resist (Dextran) over silicon wafer. A piece of thermal release tape (Nitto Denko, No3198MS) was used to transfer the membrane to a PMMA substrate after dissolution of Dextran in water. The thermal release tape was detached from the membrane by heating followed by a thin (~50 nm) platinum deposition and membrane lift-off.

7.2.3. Single nanowire electrical transport measurement

The schematics of the electrical transport measurement process steps of single nanowire beginning from the electromagnetic alignment of nanowires on PMMA substrates are shown in Figure 7.2. Figure 7.2(a) shows the electromagnetic alignment of the nanowires on a blank substrate followed by drying their ethanol solution shown in the Figure 7.2(b). Figure 7.2(c)

shows the nanowires on PMMA substrate contact transferred to a PDMS substrates. This process helps to avoid the dusts and nanowires agglomerates (from the nanowires solution) on the PMMA substrate and achieve more single nanowires on the PDMS substrate. Figure 7.2(d) shows a single nanowire on the PDMS substrate selected to align on the microelectrodes on the PMMA substrate shown in the Figure 7.2(e). In the next step shown in the Figure 7.2(f), the nanowire and the nanochannel were aligned using the microscope alignment. Then, the nanowire was thermally transferred from the PDMS substrate to the electrodes on PMMA substrate by nanoimprint lithography (Obducat NIL) at 100°C, 45 bar for 5 minutes and demolding at 70°C shown in the Figure 7.2(g). Figure 7.2(h) shows the voltammetry of the nanowire-electrodes on the PMMA substrate obtained by connecting the electrodes contact pads (shown in the Figure 6.3(h)) to the working electrodes of a DY2300 series potentiostat connected to a desktop computer. Four nanowires samples from FeNiCo and FeNiCo-Au (from each set) nanowires fabricated by different conditions were chosen for these electrical measurements.

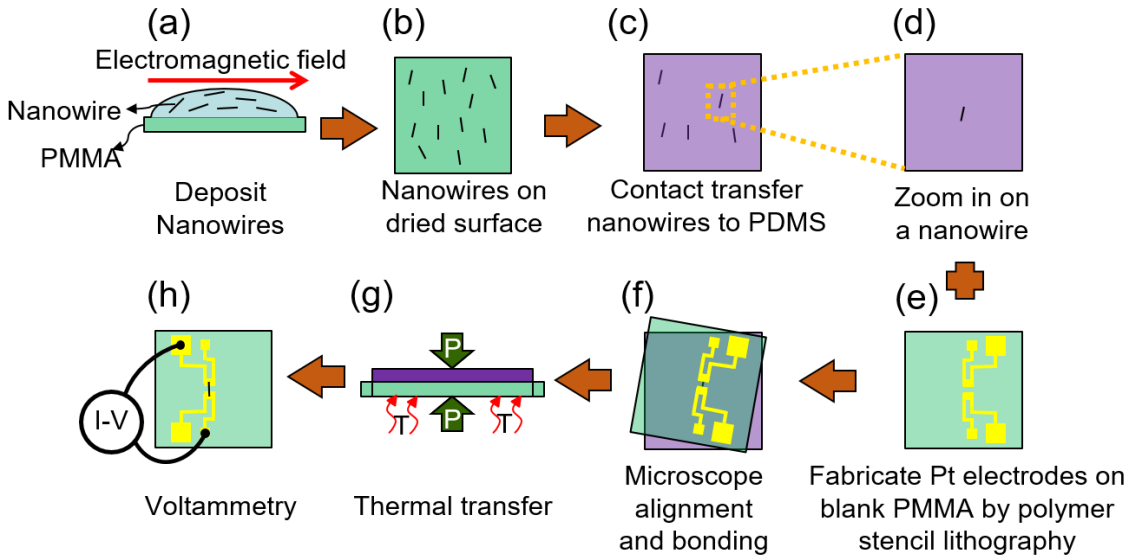

Figure 7.2. The schematics of the electrical transport measurement process steps of a single nanowire

7.2.4. Nanowires thermal transfer method

Figure 7.3 shows the schematics of the thermal transfer of a single nanowire before (a) and after (b) transfer to platinum electrodes on the PMMA substrate and the SEM images of the transferred single FeNiCo (c) and FeNiCo-Au (d) nanowires. The insets in the Figures 7.3 (c, d) show the magnified images of the contact region of the nanowires with the microelectrodes. Figures 7.3(c, d) show that both FeNiCo and FeNiCo-Au nanowires partially bent and fixed into the PMMA or electrode substrate by applying high pressure and temperature close to the one of the PMMA glass transition. This reduced the effects of contact resistance [272] and ensured the proper contact between the nanowires and microelectrodes. Partially bending the nanowires on the electrode substrates using ultrasonic techniques were reported in the literature to enhance the electrical contact between the carbon nanotubes and electrodes [273]. Thus, the thermal transfer ensures an electrically and mechanically stable contact between the single nanowire and metal electrodes on PMMA while measuring the electrical transport through the single nanowires. This property of the thermal transfer technique is very important for the nanosensor applications.

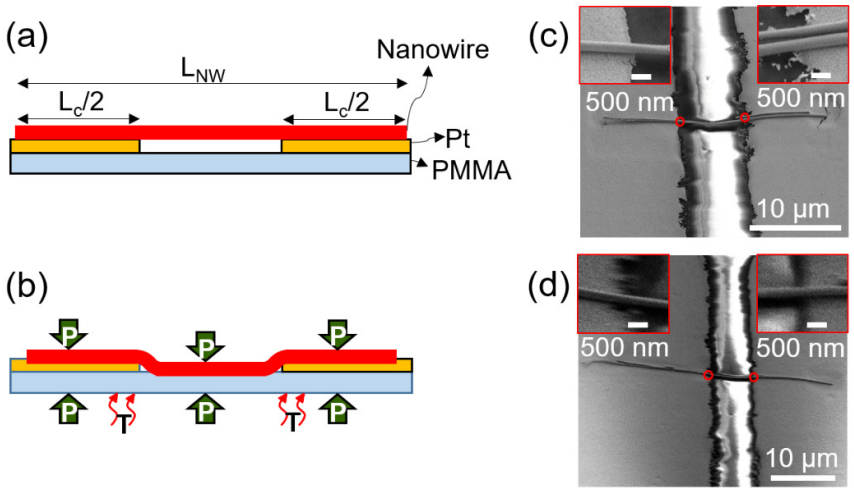

Figure 7.3. Schematics of the (a) FeNiCo and FeNiCo-Au nanowires and (b) thermal transfer of a single nanowire to platinum electrodes on a PMMA substrate.

7.3. Results and discussion

7.3.1. Nanowires 2-probe resistance measurement methodology

In order to measure the electrical transport through each nanowire composition (FeNiCo and FeNiCo-Au) with different fabrication condition, four nanowire samples from the same condition were connected to different microelectrode arrays on PMMA substrates. The electrical measurements were performed for each sample before and after connecting the nanowire. Figure 7.4 shows the (a) schematics and (b) equivalent circuit of an electrode pair (ABCDE1, ABCDE2) on PMMA connected to a nanowire (blue line). The contact pads (A1, A2, E1, E2) shown in Figure 7.4 (a) were used to connect the microelectrodes to the working electrodes of the potentiostat and measure the electrical voltammetry of the electrodes and the nanowire. An applied voltage from –0.5V to 0.5 with the resolution of 10^{-9}V was applied while the current was recorded for each measurement. Each measurement was repeated four times by connecting and disconnecting the working electrodes to contact pads to calculate the experiment errors from the voltammetry measurements. In the Figure 7.4(b), R represents the electrical resistance of each circuit, R_{NW_2P} is the 2-probe (2P) measured resistance of the nanowires using the microelectrodes of Figure 7.4 (a) which can be calculated from the equation (1):

$$R_{NW\_2P} = R_{NW} + 2R_C \quad (1)$$

In which, R_c is the contact resistance between the nanowire and the microelectrodes and can be derived from the equation (2) based on the transmission line model (TLM) [273]:

$$R_C = L_T R_S \operatorname{cotanh} (L/L_T)/(L_W) \quad (2)$$

In which, L_T represents the contact transfer length, R_S is the sheet resistance of the metal underneath the nanowire. L and L_W are the length and width of the nanowire contacts with the electrodes. Together with the nanowires thermal transfer method, the higher ratio of the nanowire contact length with the electrodes to the nanowire total length ($100\times L/L_{NW}>60\%$) reduced the effects of the contact resistance to a minimum value [274, 275].

Using the equations (3), we performed four measurements to calculate the nanowires 2-probe resistance:

$$V_{Ai\text{-}Ej} / I_{Ai\text{-}Ej} = R_{Ai\text{-}Ej}$$
$$R_{Ai\text{-}Ej} = R_{ABCi} + R_{CDEj} + (R_{NW\_2P} \text{ (if } i \neq j)), \quad i, j = 1,2 \tag{3}$$

In which, $V_{Ai\text{-}Ej}$ and $I_{Ai\text{-}Ej}$ is the voltage and corresponding current read from the voltammetry results between electrode contact pads Ai and Ej. The resistance between the Ai and Ej contact pads is shown by $R_{Ai\text{-}Ej}$. The resistance of the segments ABCi and CDEj of the electrodes are shown by R_{ABCi} and R_{CDEj}, respectively. In the equations (3), the resistance of the nanowire (R_{NW}) presented only if $i \neq j$. By simplifying these equations, one could calculate the resistance of the nanowire using four measurements from the equation (4):

$$R_{NW\_2P} = V_{A1\text{-}E2} / I_{A1\text{-}E2} + V_{A2\text{-}E1} / I_{A2\text{-}E1} - V_{A1\text{-}E1} / I_{A1\text{-}E1} - V_{A2\text{-}E2} / I_{A2\text{-}E2} \tag{4}$$

Using equation (4) allowed us to eliminate the effects of electrodes resistances and their defects from the measured 2-probe resistance of the nanowires.

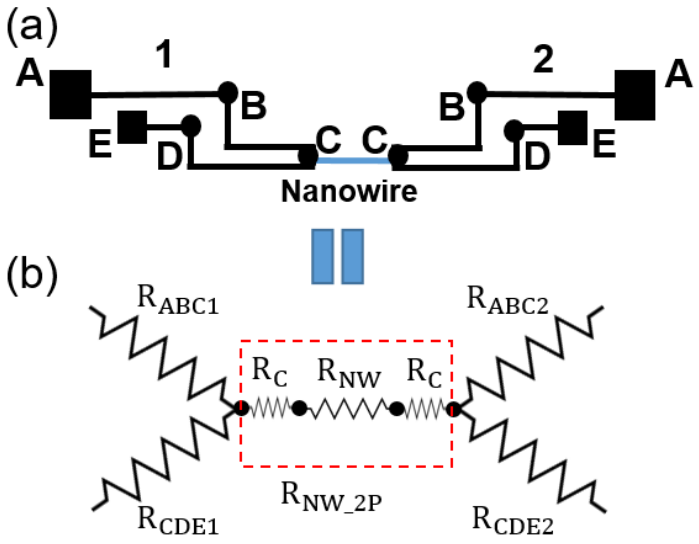

Figure 7.4. (a) Schematic configuration of an electrode pair (ABCDE1, ABCDE2) and the connected nanowire (blue line) and (b) their equivalent resistance circuit.

7.3.2. First group nanowires 2-probe resistance and errors

The resistance R_{NW_2P} of the first group of FeNiCo-Au and FeNiCo nanowires were calculated from the equation (4). Table 6.1 shows the summary of the geometries and 2-probe resistance of the individual nanowire samples of this group. The nanowires geometry errors (e.g. diameter and lengths) were measured from the SEM images and the 2-probe resistance errors were driven from the several measurements of the same nanowire 2-probe resistance. The contact lengths of the nanowires with the electrodes and their percentages to the nanowires total length were reported in this table. Sample 1 and 4 of FeNiCo-Au nanowires consisted two parallel attached nanowires which were considered as parallel resistors in the calculations. Overall, the geometry errors of the nanowires diameter and length between the two electrodes remained below 5% and 7% and the measured 2-probe resistance errors were below 1% for all samples except for the outlier. Also, the contact length percentage of the nanowires which remained above 75% for most of the samples and 60% for all of them guaranteed the minimal contact resistance effects on the measured 2-probe resistance based on the transmission line model (TLM) for nanowires and one dimensional metallic contacts [274-277].

7.3.3. First group FeNiCo nanowires equivalent resistivity and errors

For the nanowires with diameters over 100 nm the electrons flow is more homogenous that the nanowires with thinner diameters, thus their resistivity can be calculated similar to the resistivity of the bulk materials [278]. Similar calculation was used for the FeNiCo nanowires used here since their diameters were above 150 nm. Thus, the equivalent resistivity of each FeNiCo (containing oxide) nanowire from the nanowires 2-probe resistance R_{NW_2P} was calculated from the equation (5):

$$\rho_{Eq1} = R_{NW\_2P} \times (\pi d_{NW}^2/(4\, L_{NW})) \quad (5)$$

In this equation, ρ_{Eq1}, R_{NW_2P}, d_{NW} and L_{NW} are the equivalent resistivity, 2-probe resistance, diameter and length of the FeNiCo nanowire between the two electrodes,

respectively. In order to find the error of the calculated equivalent resistivity, we had to consider the errors in the measurement of d_{NW}, L_{NW} and R_{NW_2P}.

Table 7.1. Summary of the FeNiCo and FeNiCo-Au nanowires geometries (diameter and length) and contact lengths with the electrodes and their percentages and their calculated 2-probe resistance and errors shown in the [].

	Sample #	Diameter [error] (nm)	Length between electrode pair [error] (µm)	Contact length (µm)	Contact length ratio** (%)	Resistance [error] (Ω)
FeNiCo-Au	1*	164 [±6]	7.25 [±0.2]	31.86	82	359 [±0.8]
	2	239 [±5]	10.37 [±0.7]	16.88	62	4018 [±2.1]
	3	208 [±7]	7.32 [±0.4]	26.13	78	1086 [±2.8]
	4*	195 [±6]	7.31 [±0.4]	31.07	81	3091 [±1.9]
Average		202 ± 31	8.06 ± 1.5	26.50 ± 6.89	76 ± 9	2139 ± 1704
FeNiCo	1	308 [±12]	8.55 [±0.3]	13.86	62	3972 [±7.2]
	2	203 [±4]	8.16 [±0.5]	19.70	71	7199 [±5.8]
	3***	220 [±5]	5.50 [±0.3]	16.45	75	14366 [±237.0]
	4	263 [±11]	7.83 [±0.3]	13.02	62	4693 [±8.5]
Average		258 ± 53	8.18 ± 0.36	15.50 ± 3.64	65 ± 5	5288 ± 1694

* Consist of two parallel nanowires attached together.
** Contact length ratio=(contact length)/(contact length + length between electrode pair)
*** Outlier, removed from the averaging and further analysis.

The source of error in the measurement of d_{NW} came from the variation of the nanowire diameter along the length of the nanowire and the clarity of the SEM images while for the L_{NW} measurements the errors were because of electrode edge roughness as well as the bending of the nanowire between the two electrodes. Also, the error origins in R_{NW_2P} measurement were mainly because of the connection of the potentiostat working electrodes and the micro-electrodes. For each of these parameters, the error was calculated by subtraction of the

maximum value from the average value of that parameter. Using the above process, one could calculate the error of the nanowire resistivity measurement from the equation (4):

$$\Delta\rho_{Eq1} = \sqrt{\left(\frac{\partial\rho_{NWEq1}}{\partial R_{NW\_2P}}\Delta R_{NW\_2P}\right)^2 + \left(\frac{\partial\rho_{NWEq1}}{\partial d_{NW}}\Delta d_{NW}\right)^2 + \left(\frac{\partial\rho_{NWEq1}}{\partial L_{NW}}\Delta L_{NW}\right)^2} \quad (6)$$

In which $\Delta\rho_{Eq1}$, Δd_{NW}, ΔL_{NW} and ΔR_{NW_2P} were the errors in the nanowire resistivity, diameter and length between the electrodes and resistance measurements, respectively. Equation (4) could be simplified as equation (5):

$$\Delta\rho_{Eq1} = \sqrt{\left(\frac{\pi d_{NW}^{\,2}}{4L_{NW}}\Delta R_{NW\_2P}\right)^2 + \left(R_{NW\_2P}\frac{\pi d_{NW}}{2L_{NW}}\Delta d_{NW}\right)^2 + \left(-R_{NW\_2P}\frac{\pi d_{NW}^{\,2}}{4L_{NW}^{\,2}}\Delta L_{NW}\right)^2} \quad (7)$$

The effects of bending or the surface morphology of the nanowires on the resistivity value of the nanowires were the additional sources of the uncertainties in the resistivity calculations which were not considered in the equation (7).

Using the equations (3, 7)), the equivalent resistivity value of the FeNiCo nanowires and their errors were calculated. Table 7.2 shows the results of these calculations. The equivalent resistivity value of sample 3 of the FeNiCo nanowires was an outlier comparing to the other samples of the same nanowire type, therefore this sample was removed from our future analysis. The average resistivity value was two orders of magnitude higher than the bulk resistivity of Fe, Ni, Co and Au [279]. This is because of the increased resistivity of nanowires than the bulk materials due to the scattering of the electrons from the nanowire boundaries [265] (surfaces), variation of the number of grain boundaries depending on the nanowire dimensions and possible impurities of the nanowire [280, 281].

7.3.4. First group FeNiCo-Au nanowires Au shell thickness and resistivity

For the thin FeNiCo-Au nanowire, the electron transport through the thin Au layer (<100 nm) is not similar to bulk materials and follows the Samble's model [228]. In order to find the electrical resistivity and thickness of the Au shell of the FeNiCo-Au core-shell

nanowire, one could consider this nanowire as two parallel nanowires (electrical resistors) which include the FeNiCo core covered with a thin oxide layer and the Au shell. Figure 7.5(a) shows the FeNiCo-Au nanowires core and shell segments schematics and Figure 7.5(b) shows the nanowire and FeNiCo and Au segments equivalent 2-probe resistance with their relative relationships. Figure 7.5 shows the FeNiCo and oxide core by index "NW1" and it shows the FeNiCo-Au nanowire by index "NW2" which is used in the continue of this chapter.

Table 7.2. Summary of the equivalent resistivity of the first group FeNiCo nanowires.

	Sample #	Resistivity (10^{-5} Ω.cm) [error]
ρ_{Eq1}	1	346 [±29.6]
	2	285 [±20.8]
	4	326 [±30.0]
Average		319 [±31.1]

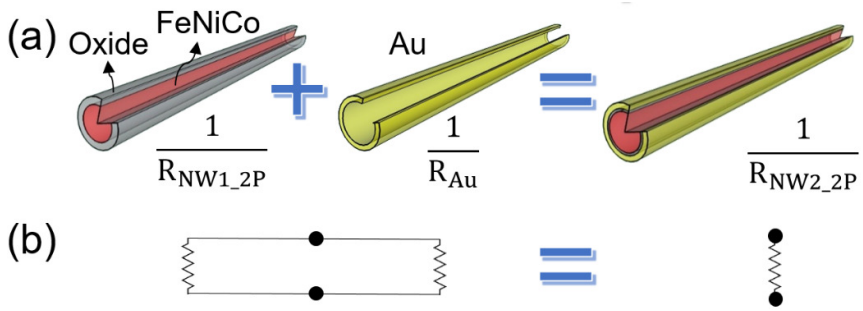

Figure 7.5. (a) Schematics of the core and shell segments of the FeNiCo-Au nanowires and their 2-probe electrical resistance relationship and (b) their equivalent electrical resistance circuit with segments as parallel resistors.

Using the equivalent resistance for parallel resistors shown in the Figure 7.5(b), equation (3) and simplifying, the resistivity of the Au shell is driven from the equation (5):

$$\rho_{Au(n)} = \pi\left(\frac{{d_{NW2}}^2 - \left(d_{NW2} - d_{Au(n-1)}\right)^2}{4}\right) \Big/ \left(\frac{L_{NW2}}{R_{NW2\_2P}} - \frac{\pi\left(d_{NW2} - d_{Au(n-1)}\right)^2}{4\rho_{Eq1}}\right) \quad (8)$$

In which, d_{NW2} and L_{NW2} are the diameter and length of the FeNiCo-Au nanowire, respectively, R_{NW2_2P} is the 2-probe resistance of the FeNiCo-Au "NW2" nanowire and ρ_{Eq1} is the equivalent resistivity of the FeNiCo and oxide core "NW1". The $d_{Au(n-1)}$ denotes the equivalent diameter (or two times of the thickness) of the Au shell which is unknown together with the $\rho_{Au(n)}$ which represents the resistivity of the Au shell. Thus, $\rho_{Au(n)}$ and $d_{Au(n-1)}$ in the Equation (8) should be defined using an iterative approach in which "n" represents the number of iteration. The iterative steps to solve the Equation (8) are as follows:

1. In the first step, we calculated the Au resistivity ($\rho_{Au(1)}$) for each sample from an initial equivalent diameter guess ($d_{Au(0)}$) for the Au layer (initial guess was 50 nm for all of the samples based on the SEM image measurements) using the equation (8).
2. Then, we calculated the Au equivalent diameter (d_{Au}) from the average values of the new resistivity ($\rho_{Au(1)}$) for all of the FeNiCo-Au nanowire samples using the Sambles model [282] which predicts the electrical resistivity of the gold nanowires by changing their diameter. Figure 7.7 shows the best curve (an exponential decay with five parameters) fitted to the replot of this model for the resistivity versus diameter [228] used for this estimation.

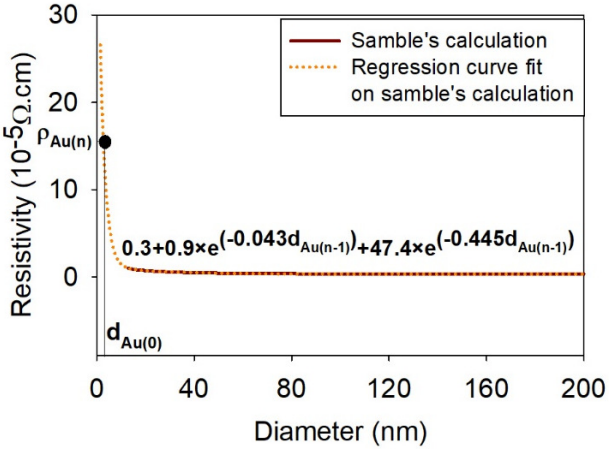

Figure 7.6. Replot of Samble's model and fitted curve formula.

3. Lastly, we repeated the first and second steps to find the values of converged equivalent diameter ($d_{Au(n-1)}$) and average resistivity ($\rho_{Au(n)}$) of the gold shell for the FeNiCo-Au nanowire samples.

Using the above procedure, the Au layer average resistivity and equivalent diameter converged within nine iterations to 4.1 10^{-5} Ω.cm and 6.2 nm, respectively. This resistivity value was similar to the one 4.63 10^{-5} Ω.cm for rectangular (40 × 33 nm) Au nanowire in literature [283]. The dimensions of the nanowire in the literature was significantly larger than the one of the Au shell measured here although the resistivity values were similar. The main reason could be attributed to the higher efficiency of the shell Au layer comparing with the Au nanowire in terms of electrical conductivity because the electrons begin to path through the perimeter of the nanowires of these dimensions [280].

7.3.5. First group FeNiCo-Au nanowires segments current transport

Having the average equivalent resistivity of the FeNiCo nanowires with oxide coating and the average resistivity and the equivalent diameter of the Au layer of the FeNiCo-Au nanowires, we calculated the FeNiCo-Au nanowires core and shell segments contribution in transferring the electrical current through the nanowire. We calculated these values from the equations (9) by assuming a 0.5V applied voltage to the two ends of the nanowires and compared them with the current passing through a hypothetical pure Au nanowire with the same dimensions:

$$I_{\text{Au shel}} = \frac{V}{\frac{4\rho_{Au}L_{NW2}}{\pi\left(d_{NW2}{}^{2} - (d_{NW2} - d_{Au})^{2}\right)}}$$

$$I_{FeNiCo} = \frac{V}{\frac{4\rho_{FeNiCo}L_{NW2}}{\pi(d_{NW2} - d_{Au})^{2}}} \qquad (9)$$

$$I_{\text{Au layer}} = \frac{V}{\frac{4\rho_{Au}L_{NW}}{\pi d_{NW}{}^{2}}}$$

In equations (9), ρ_{Au} and d_{Au} and ρ_{FeNiCo} were the average values of converged resistivity and equivalent diameter of the Au shell and the average equivalent resistivity of FeNiCo nanowires. Table 7.3 shows the summary of the currents passing through each segment of the samples 1, 3 and 4 of the FeNiCo-Au nanowires and their equivalent hypothetical pure Au nanowires. The percentage of current passing through each segment was shown for individual core-shell nanowires. A significantly higher percentage of the Au layer contribution above 80% in transferring current for all of the core-shell nanowire samples (84% average) demonstrated the key role of the Au shell in the control of the electrical transport through the FeNiCo-Au nanowires. The low standard deviation of this percentage less than 2% showed the consistency of the above controllability of Au shell. The current transport through the hypothetical pure Au nanowire were two to three orders of magnitude higher than the ones through individual FeNiCo-Au nanowires segments. This demonstrates the ability of the FeNiCo-Au nanowires to control the amount of the current transport through them by varying their composition (e.g. Au layer thickness) in comparison with the homogenous nanowires.

Table 7.3. The summary of the currents and their percentages () passing through each segment of the samples 1, 3 and 4 of the FeNiCo-Au nanowires and their equivalent hypothetical pure Au nanowires.

	Sample	Au	FeNiCo	Au
I (10^{-5}A)	1	13.2 (86%)	2.1 (14%)	2430
	3	33.3 (83%)	6.9 (17%)	7740
	4	46.8 (84%)	9.0 (16%)	10210
Average	84±1.5%	16±1.5%	100%	

7.3.6. Second group FeNiCo nanowires Au shell deposition optimization

In order to study the optimum Au shell coating conditions on FeNiCo nanowires and compare the results with pure FeNiCo nanowires, we prepared five samples with the similar process explained above. Sample (S1) was the pure FeNiCo nanowires while samples (S2) and

(S3) were the FeNiCo nanowires dipped in the $KAuCl_4$ (pH=2.8) for 30 min and 60 min, respectively. For the samples (S4) and (S5), the dipping time in the $KAuCl_4$ solution was kept as a constant while the pH of the solution was change to 2 and 1, respectively. Thus, we were able to observe the effects of changing the time and pH of the $KAuCl_4$ solution on the Au shell coating over the FeNiCo nanowires using the samples (S1) to (S5). Four single nanowire specimens were chosen from the five samples (S1) to (S5) for the electrical measurements. Electrical measurements were performed on all of these twenty specimens to calculate the 2-probe resistance and the equivalent resistivity of the nanowires with the same procedure explained before. The summary of the equivalent resistivity statistics of the samples (S1) to (S5) are presented in the Figure 7.7. The equivalent resistivity values of the (S2) were (~50%) smaller than the one for the reference sample (S1) while these values were larger for the samples (S3) to (S5) than the reference samples. This indicates a successful Au shell coating on the FeNiCo nanowires using the (S2) conditions (highest pH=2.8 and lowest dipping time=30 min). However, the dipping in the solution with conditions at the same pH=2.8 and longer time (60 min) for (S3) or lower pH=2 (S4), 1 (S5) and same time (30 min) were unsuccessful to coat a homogenous shell around the FeNiCo nanowires. This can be attributed to the fact that dipping the FeNiCo nanowires into the $KAuCl_4$ solution for long time or low pH does not help to substitute Au molecules on the surface of the nanowires. In fact, such dipping conditions may corrode the nanowires surface and result in a composition change or roughness increase over the nanowires surfaces. Therefore, the dipping condition of the (S2) was the most proper condition for coating Au shell around the FeNiCo nanowires based on the electrical measurements.

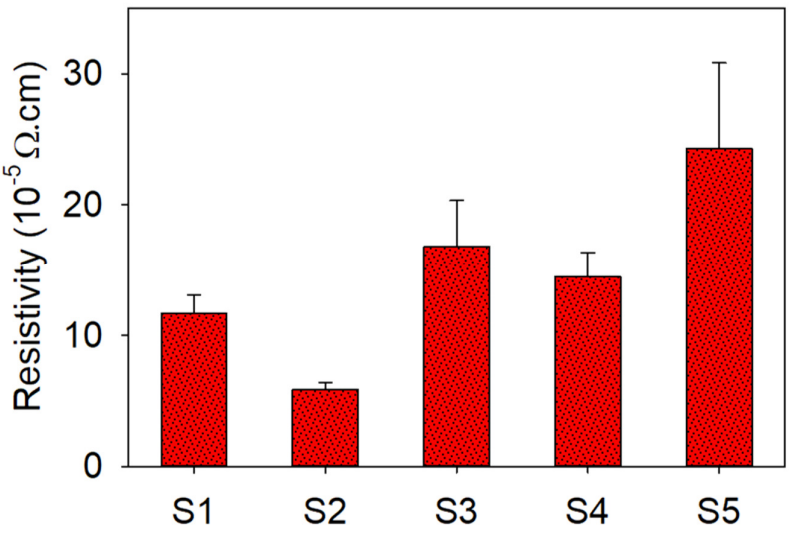

Figure 7.7. Statistic summary for the equivalent resistivity of the twenty individual nanowire specimens from the samples (S1) to (S5). The error bars show one standard deviation of the data of the four nanowire specimens of each sample (S1) to (S5).

7.3.7. Second group FeNiCo-Au nanowires segments current transport

Using the iterative approach, we calculated the approximate equivalent diameter (or two times of the thickness) and the resistivity of the Au shell for the nanowires second group FeNiCo-Au nanowires (S2). After twenty iterations, the Au shell thickness was estimated to be ~12.8 nm with the resistivity of ~1.02×10^{-5} Ω.cm. By using these values and assuming the FeNiCo-Au nanowire core and shell as serial resistors, we calculated the current passing individually through the core and shell of the nanowires and compared them with the ones for a pure Au nanowire with the same outer diameter as the one of the core-shell nanowires. Similar to the first group nanowires 0.5 V electric potential was assumed at the two ends of the nanowires. Table 7.4 shows the summary of these currents. The percentages of the currents passing through either the core or the shell of each specimen are also presented. Overall for the FeNiCo-Au nanowires, the current mostly (56% average) passed through the Au shell consistently (only 2% standard deviation). This is due to the consistent coating of the thin (~13 nm) Au shell with low resistivity (~1×10^{-5} Ω.cm) for the four FeNiCo-Au nanowire specimens of (S2) comparing to the thick (~253 nm average) FeNiCo core with high equivalent resistivity

(~12×10^{-5} Ω.cm). The currents passing through the core-shell nanowire, its core or its shell are one order of magnitude smaller than a pure Au nanowire (335×10^{-5} versus 3470×10^{-5}, respectively) with the same dimensions. The above properties enable one to control the resistivity value of the entire core-shell nanowire within a wide range by changing the thickness of the Au coating. Even though the second group FeNiCo-Au nanowires fabricated using different conditions from the first group, the higher thickness of the Au shell of the second group (~13 nm) compared to the one of the first group (~6 nm) shows the successful Au shell increment by increasing the FeNiCo nanowire dip time in the Au solution (3 min to 30 min, respectively).

Table 7.4. Summary of the current values and percentages passing through each nanowires specimen of the second group FeNiCo-Au nanowires (S2).

	Sample #	Au	FeNiCo	Au nanowire
I (10^{-5}A)	1	270 (55%)	220 (45%)	2830
	2	380 (53%)	340 (47%)	4350
	3	310 (57%)	230 (43%)	2970
	4	380 (57%)	280 (43%)	3730
Average		56±2 %	44±2%	

7.3.8. Second group FeNiCo and FeNiCo-Au nanowires morphology

Figure 7.2 shows the scanning electron micrographs (SEM) of the nanowires in bunch (top figures) and the individual nanowires (bottom figures) placed on separate microelectrodes on polymer (PMMA) substrates for the electrical measurements. The insets in the bottom figures show the magnified SEM of the single nanowires surfaces. The SEM images of the

nanowires in bunch in this figure show that increasing the nanowires exposure time to the $KAuCl_4$ solution or decreasing the pH of the solution increased the gold particles agglomerates on the nanowires. On the other side, the SEM images of the individual nanowires show an increase of the nanowires surface roughness almost only for the dipping in the $KAuCl_4$ solution with lowest pH values (S5). These results are in conjugate with the electrical measurements demonstrating successful Au coating of (S2).

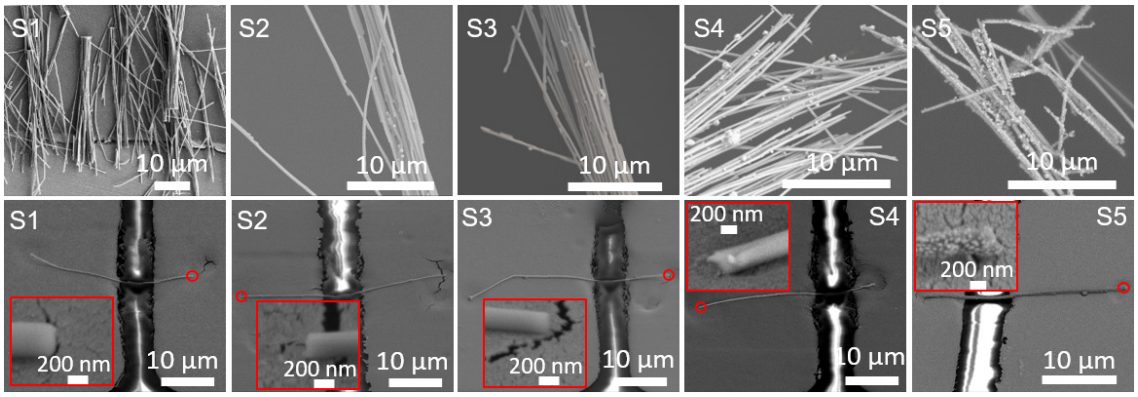

Figure 7.8. SEM of the (S1) pure FeNiCo nanowires and FeNiCo nanowires dipped in $KAuCl_4$ (S2) pH=2.8 for 30 min, (S3) pH=2.8 for 60 min, (S4) pH=2.0 for 30 min, (S5) pH=1.0 for 30 min. The top images show the nanowires in bunches while the bottom figures show the individual nanowires placed on the electrodes on plastic substrates. The insets in the bottom figures show the magnified images of the individual nanowires end points.

7.4. Conclusion

A new FeNiCo-Au core-shell nanowire with enhanced electrical, mechanical and durability properties was proposed and compared with FeNiCo nanowires. The FeNiCo core increased the mechanical strength of the nanowire while the Au shell enhanced the electrical conductivity and durability of the nanowire. An iterative approach was used to estimate the resistivity and thickness of Au shell of the FeNiCo-Au nanowires. Two groups of nanowires were tested in this study. The first group was used for the initial study of the electrical properties of the FeNiCo-Au nanowire while the second group designed to find the optimum Au deposition conditions on the FeNiCo nanowires. For the first group, the results showed a consistent and high controllability (average 84%) of the thin (~6 nm) Au layer to transfer current through the FeNiCo-Au nanowires. For the second group, more than 50% of the current

passing through the new FeNiCo-Au nanowires passed through their thin (~13 nm) shell. The rough comparison of the first group and second group FeNiCo-Au nanowires showed the increment of the Au layer on the FeNiCo nanowires by increasing their dipping time in $KAuCl_4$ solution. The presented FeNiCo-Au core-shell nanowires with excellent controllability over the electrical transport, mechanical strength and robustness would be a perfect alternative for various applications of metallic nanowires as nanoelectrodes. The technique proposed to integrate individual nanowires with external electrodes on flexible transparent polymer microchips offers a highly efficient method for the fabrication and characterization of transparent electronics [248, 249] and single nanowire sensors [284-288] with low cost. Also, the iterative approach allows the resistivity and thickness measurement of ultra-thin and long metal coatings on single nanowires with high accuracy. This is of special significance because of the very difficult fabrication and characterization techniques for the nanowires of such dimensions.

Chapter 8. Magnetic Properties Of FeNiCo-Au Nanowires.

8.1. Introduction

Magnetic nanowires attracted significant attentions in the last two decades because of their applications in several areas including magneto-optic, microwave and data storage devices and spin valve or magneto resistive sensors [289]. As a magneto-optic element, they have a higher magneto-optical response comparing to the same magnetic material in bulk because of the plasmon resonance effects in magnetic nanowires [290, 291]. In microwave devices, the magnetic nanowires are used as microwave nonreciprocal insulators because of their higher saturation magnetization than the typical bulk insulators [292, 293]. Magnetic domain-wall racetrack memories based on the arranged magnetic nanowires are produced as high performance alternative for the conventional drive storages based on magnetic disks. This is because of the low cost of storing and high speed of reading the data in domain walls (which are 10-100 per racetrack for a nanowire with 100 nm in diameter and several micrometers in length) [294, 295]. As magnetoresistive or spin valve sensors (e.g. to detect biomolecules [296]), the magnetic nanowires have higher performance and scalability thus higher sensitivity and lower power consumption than the similar traditional micron size devices [297, 298].

Core-shell magnetic nanowires offer the combined properties of several magnetic nanowires composed of a single material thus they have the ability of being used for various sensors applications [299]. In ε-Fe_3N-GaN core-shell nanowires, the combination of ferromagnetic Fe_3N core with the antiferromagnetic GaN shell properties results in an improved unidirectional anisotropy [82]. Although the GaN shell protects the core, it still goes through oxidation. Additionally, predicting the nanowire magnetic properties by applying various magnetic field strengths is more difficult than the core-shell nanowires composed of only one magnetic material [82]. Fe-Fe_3O_4 core-shell nanowire is an example that has tunable magnetic properties due to the Fe core while the Fe_3O_4 shell is desirable to be used for

biomedical purposes due to the high chemical stability and feasibility for biomedical applications [300]. However Fe-Fe_3O_4 nanowires are disable to change their magnetization at low applied magnetic fields because of their Fe core high coecivity [299]. Other alternatives for the core material such as Ni and Co with lower coercivity values make the entire fabrication process very complicated and expensive. Also an additional insulating SiO_2 layer is required for the fabrication of such core-shell nanowires with Ni core [299, 301]. GaAs-InAs core-shell nanowires with epitaxially grown InAs (high electrical conductivity) shell over the GaAs core (high electrical resistivity) show specific semiconducting properties. The current GaAs-InAs nanowires lengths are limited to 2 μm and their shell minimum thickness is around 25 nm because of the fabrication limitations [302]. Another example of functional core-shell nanowires is the Fe_2P-C with higher ferromagnetic-paramagnetic transition temperature than the Fe_2P nanowires. The downside of Fe_2P-C nanowires to be used as sensor components is the high electrical resistivity of their carbon shell [303]. The magnetic core-shell nanowires with a shell composed of the oxide of the core material such as Co-CoO enable one to control their shell thickness in the order of 4 – 30 nm although they are limited to a shell from the oxide of the same core material with a relatively low electrical conductivity [304].

The preliminary step for the nanowires placement introduced in the chapter six to fabricate the intermediate nanosensors for the nanochannel-nanopore device explained in the first chapter is the magnetic alignment of the nanowires that requires the nanowires to be magnetic. For this reason, the FeNiCo and FeNiCo-Au nanowires synthesized in the chapter 7 with high electrical and mechanical properties should also maintain their ferromagnetic properties to be used as nanosensors. Thus, a study to investigate the magnetic properties of FeNiCo-Au nanowires is required to predict their magnetic alignment efficiency before and after Au shell coating. In this chapter, we studied magnetic properties of the DC electrodeposited (second group) FeNiCo and FeNiCo-Au nanowires explained in the chapter

7. Although the magnetic behaviors of the nanowires have been previously studied [305, 306], a few researches were done to investigate the magnetic properties of the individual nanowires [307, 308].

8.2. Experimental

The process steps to connect a single nanowire to the microelectrodes on PMMA substrates are shown in the Figure 8.1. The pre-grown FeNiCo nanowires were electrodeposited into porous alumina template followed by their dipping into $KAuCl_4$ to fabricate the Au shell. The microelectrode arrays were fabricated by stencil lithography using polymer membrane. Figures 8.1(a-g) show the steps to align the nanowires on blank substrates using electromagnetic field (a, b), contact transfer of the nanowire to a PDMS substrate (c), selection of a single nanowire (d), fabrication of the microelectrodes (e), microscope alignment of the nanowire and microelectrodes (f), thermal transfer of the nanowire from the PDMS substrate to the microelectrodes on PMMA (g) and the voltammetry of the nanowire-electrodes in the presence of an electromagnet connected to a constant voltage applying a constant electromagnetic field to the nanoelectrode (h). Four nanowire samples from the DC electrodeposited (second group) FeNiCo and FeNiCo-Au nanowires were selected for the experiments. The nanoelectrode fabrication methods details were explained in the chapters 7.

8.3. Results and discussion

8.3.1. Study of the magnetic properties of the FeNiCo-Au nanowire nanoelectrodes

The magnetic properties of the FeNiCo-Au core-shell nanowires were studied and compared with the reference FeNiCo nanowires. These experiments were performed by applying a constant voltage (0.5 V) to the nanowires while measuring their current variations versus time inside a constant external applied magnetic field. Two magnetic fields strength 10 and 20 were applied to two sample nanowires of each type (FeNiCo and FeNiCo-Au) while the magnetic field 30 Oe was applied to four sample nanowires.

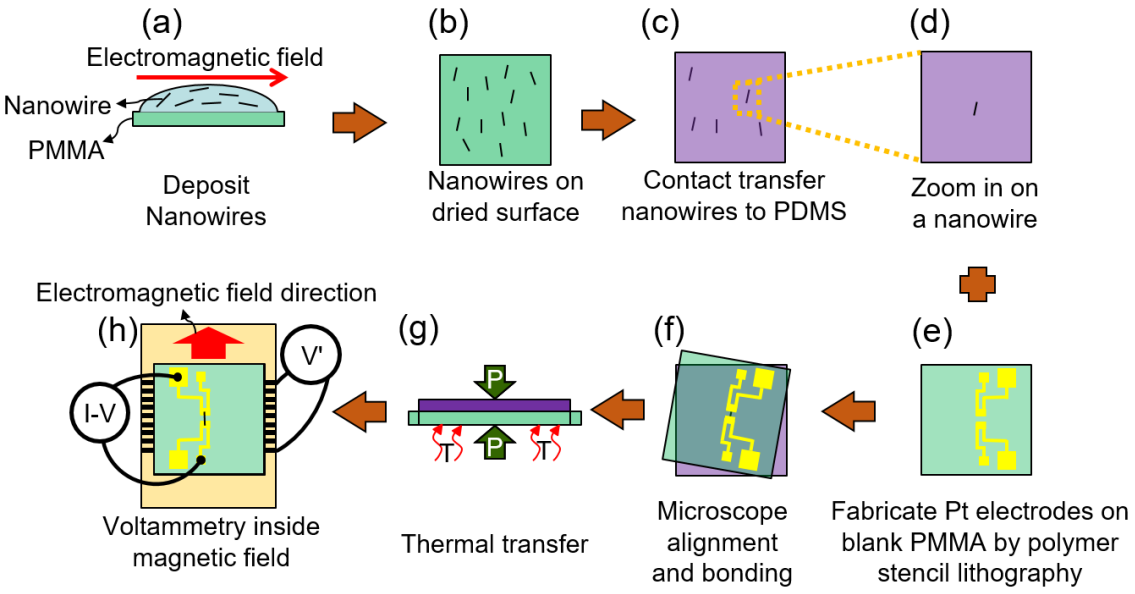

Figure 8.1. Schematics of the electromagnetic properties measurement of single nanowires

The measurements were performed on the nanowires in parallel with (to calculate the longitudinal magnetoresistance (LMR)) and perpendicular (to calculate the transverse magnetoresistance (TMR)) to the applied magnetic field direction (shown in the Figure 8.1(h)). Figure 8.2 shows the results of the current measurement versus time for one sample of FeNiCo nanowires while the nanowire was in parallel with the external magnetic field direction and their corresponding LMR values. As shown in Figure 8.2 (a), by applying the magnetic field (at t=0), the amount of the current passing through the nanowire gradually decreased to a constant level (saturation point or at t=S). The amount of current decrease and the time delay for the current to reach to the saturation point (which determines the nanowire coercivity) increase proportional to the amount of the applied magnetic field intensity. Also, the current increased almost to the initial value (neglecting the hysteresis effects) by the removal of the external magnetic field. Such behavior of increasing the nanowires resistance by applying the magnetic field is similar to the one for the previously reported nickel based magnetic nanowires at low applied magnetic fields (<1000 Oe) [309-311]. To compare the magnetic properties of the specimens, we calculated the magnetoresistance (MR) values from the I-t curves of each specimen using the equation (2) [312]:

$$MR\% = \frac{\Delta\rho}{\rho} \times 100 = \frac{\rho_s - \rho_0}{\rho_0} \times 100 = C\mu B^2 \times 100 \quad (2)$$

In this equation, ρ_0 and ρ_s are the nanowires steady state equivalent electrical resistivity (which were derived from and could be replaced by the nanowires 2-probe resistance) before and after applying the magnetic field, respectively. Also, C is a constant, μ is the electron mobility through the nanowires and B is the magnetic field intensity. The LMR and TMR of the reference FeNiCo nanowire and only LMR of the FeNiCo-Au nanowires were calculated and plotted. As an example, Figure 8.2(b) shows the corresponding LMR plot for one sample of the FeNiCo nanowires versus the magnetic field intensity calculated from the I-t curves. The positive MR corresponds to the current decrease in the nanowire when the magnetic field is applied. A parabolic curve based on the equation (2) was fitted to the MR values versus the magnetic field intensity to find the (Cμ) for all samples. The electron mobility of the nanowires is proportional to their rotational velocity under an external applied magnetic field hence proportional to their electromagnetic alignment efficiency. Thus, the significance of comparing the electron mobility (μ) of the nanowires is correlated with their higher alignment efficiency under a certain applied magnetic field.

8.3.2. LMR, TMR and electrical mobility of FeNiCo and FeNiCo-Au nanowires

Figure 8.3 shows the schematics of the LMR and TMR measurement methodology (a), the summary of the LMR and TMR values for the FeNiCo nanowires and LMR values for FeNiCo-Au nanowires (b) and their corresponding electron motilities Cμ (d). The magnitude of the LMR and TMR increased for both FeNiCo and FeNiCo-Au constantly by increasing the magnetic field intensity while their relative magnitudes remained almost constant. The LMR values of the FeNiCo-Au nanowire were lower than the one of the pure FeNiCo nanowire

especially at higher applied magnetic field intensities that was also true for the electrical mobility values.

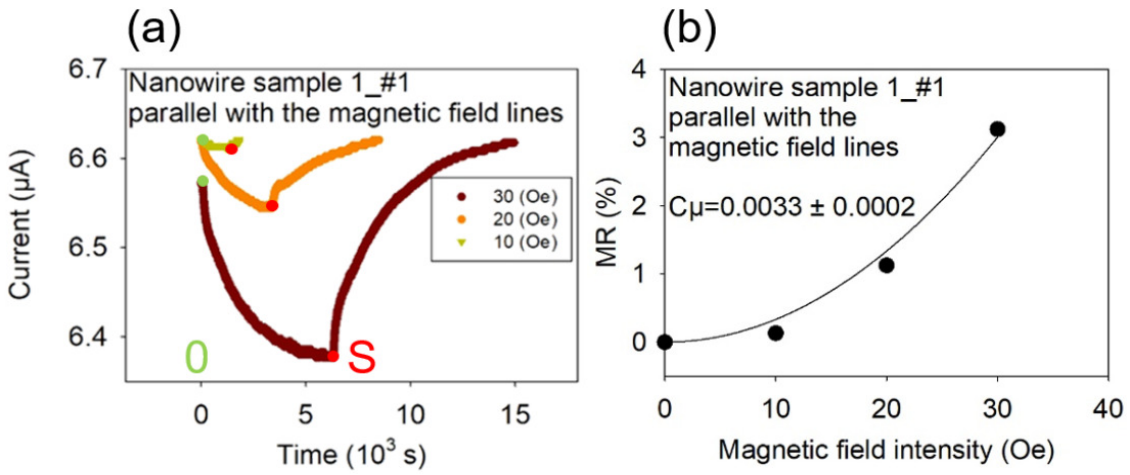

Figure 8.2. Nanowire specimen one of the (S1) (a) I-t curve for 10, 20 and 30 Oe applied magnetic field intensities when the magnetic field was applied (0) and disconnected (S) and (b) the corresponding LMR values for the applied magnetic fields and their parabolic fitted curve ($C\mu B^2$).

This can be attributed to the fact that the electrical resistivity of the Au shell of the FeNiCo-Au nanowires was almost unaffected by applying the magnetic field comparing to the one for the FeNiCo core. Since more than 50% of the current for the FeNiCo-Au nanowires passes through the Au shell (based on the electrical transport measurement data shown in the chapter 7), the LMR and TMR for the FeNiCo-Au nanowire were lower (~20% average) than the ones of the pure FeNiCo nanowire. Also the TMR and their corresponding electrical mobility values were slightly higher than the LMR and their corresponding electrical mobility values for the pure FeNiCo nanowires that is observed for the previously reported Ni based nanowires [309-311]. The lower electron mobility of FeNiCo-Au nanowires compared to the one for FeNiCo nanowires result in a higher required electromagnetic field strength to achieve the same alignment accuracy for FeNiCo-Au nanowires.

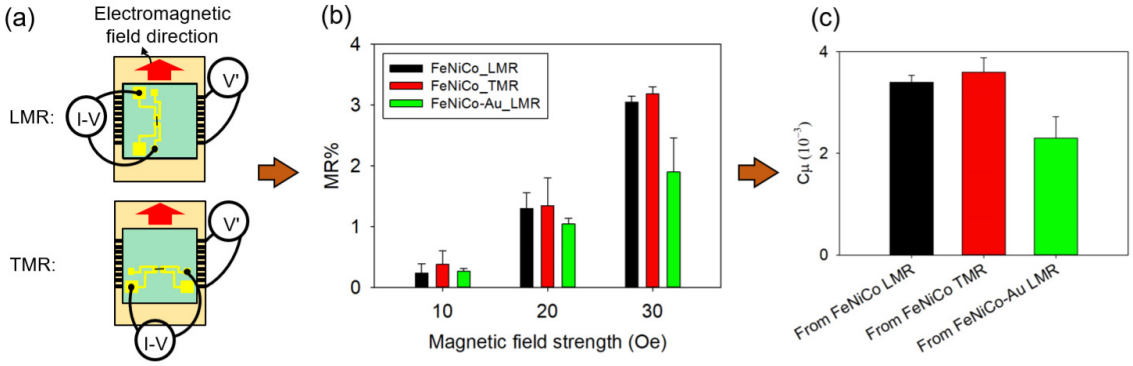

Figure 8.3. Summary of the statistics for the LMR and TMR at (a) 10 Oe (b) 20 Oe and (c) 30 Oe applied magnetic field strengths and (d) the corresponding Cμ value of the eight nanowire specimens of the (S1) and (S2)

8.4. Conclusion

The magnetic properties of a new magnetic FeNiCo-Au core-shell nanowire with unique electrical, mechanical and magnetic properties were studied and compared to those from the reference FeNiCo nanowires. The results showed that for the FeNiCo-Au nanowires the LMR and mobility values were in average ~20% lower than the ones of the FeNiCo nanowires while the LMR and TMR consistently increased by increasing the applied magnetic fields. The results showed that the electromagnetic alignment of the FeNiCo-Au nanowires is less efficient than the one of the FeNiCo nanowires because of the lower electron mobility of the FeNiCo-Au nanowires that can be compensated by applying a higher magnetic field intensity during the alignment. There is a tradeoff between the more efficient magnetic alignment of FeNiCo nanowires and resistivity control of FeNiCo-Au nanowires. Also, the nanowires long MR saturation times (high coercivity) are desirable for the applications requiring a nanoelectrode resistant to an external magnetic field. The abovementioned properties make the new FeNiCo-Au nanowires excellent candidates for nanoelectrodes and nanosensors applications.

Chapter 9. Simulation Of Nanopore Based Nanosensors For Nanoparticle Translocation

9.1. Introduction

Numerical simulation is a useful tool to understand the electrokinetics and sensing mechanisms in the development of nanopore/nanochannel fluidic sensors. In this study, we are developing a new nanochannel-based sensor utilizing time-of-flight (TOF) measurements during translocation of a nanoparticle through the nanochannel flight tube. We use the finite element (FE) simulations to support the design and operation for this new type of biosensor. Among the two testbed sensors that are shown in Chapter 1, the second test bed sensor which measures TOF using the two in-plane nanopores formed in the nanochannel flight tube is a completely new type of the sensor design. We name it as a "double nanopore-nanochannel sensor" Therefore, our simulation work focuses on this double nanopore-nanochannel sensor. We study the effects of the geometry of the in-plane a double nanopore-nanochannel sensor on the translocation of the nanoparticle by a 3D FE simulation. The amplitudes of ionic currents are compared for two shapes of the nanopores that are elliptical and triangular. In addition, the velocity distributions of the ionic solution through the nanopores are driven in 2D and 3D.

In Section 6.2, a brief summary of the relevant literature is provided. Section 9.3.1 shows the simulation methodology that we use for the simulation work. In sections 9.4 and 9.5 we discussed about the results and conclusions.

9.2. Literature review

Driving individual molecules (nanoparticle) through the nanopore by applying a voltage difference to the electrolytic fluid chambers on either side of the nanopore produces an ionic current, which changes during the translocation of the nanoparticle. The current blockage due to the nanoparticle translocation makes an observable change in the ionic current, which is useful for the study of biomolecules. Many efforts have been made to understand the fundamentals of the electrokinetic behavior of nanoparticle translocation using finite element

(FE) models [126, 137, 138, 313]. The FE model simulates the fluid flow, electric potential and ionic concentrations for the entire geometry and the vicinity of the particle and nanopore in the steady state when the nanoparticle reaches to any position. These FE simulations focus on the effects of two major factors in the translocation of the nanoparticle through the nanopore: the geometry [314-316] and surface charges [139, 142, 317-319] of the nanopore and nanoparticle.

To study the effects of the nanoparticle dimensions on the ionic current, the translocation of a rigid nanoparticle through the nanopore with a constant charge was simulated [314]. The ionic concentration inside the nanopore, the velocity of the nanoparticle and longitudinal ionic current were calculated. The results of this simulation show a proportional relationship between the current blockage magnitude and duration with the cross-sectional area and length of the nanoparticle, respectively. The theoretical results agreed with the experimental values. However, these results, which are based on the continuum model, have discrepancies from the experiment when the number of ions is very low inside the nanopore. In addition, the complex geometry of the nanopore in comparison with the continuum model can be another source of error in the simulation results [314]. In another study, the electrophoretic translocation of a nanoparticle through a converging-diverging nanopore was simulated to understand the effects of the geometry of the nanopore during the translocation [315]. The results of this work show that the local electric field is intensified inside the nanopore with such a shape, which is in contradiction with a nanopore with a uniform cross section. In addition, this simulation predicts that a pressure gradient is induced inside the nanopore and the velocity of the particle increases at the throat of the new nanopore structure. However, the disadvantage of the simulation is that the predicted behavior is not true if the surface charge density of the nanoparticle and nanopore are the same sign and magnitude. In this case, the pressure gradient reverses the motion of the nanoparticle [315].

The effects of the non-uniform surface charge of the nanopore wall on the ionic current is numerically studied for a conical shape nanopore [139-141]. The results of the simulation show that the non-uniform surface charges influence the concentration of the ions at the tip of the nanopore, which changes the ionic current. This becomes more important when the ionic concentration decreases. Although this simulation was able to predict the effects of the non-uniform surface charge of the nanopore on the ionic current, it was unable to consider the convective ionic current [139]. Another simulation studies the effect of surface charge of the nanoparticle on its translocation through a cylindrical nanopore [142]. This simulation predicts the effects of non-uniform surface charge of the nanoparticle on the local ionic concentration and electric potential. The results also predict the electrophoretic motion of the nanoparticle based on the non-uniform surface charge of the nanoparticle. Because of the electroosmotic flow surrounding the nanoparticle with non-uniform surface charge, the motion of the nanoparticle mostly becomes independent from the viscous force. The weakness of this simulation is the assumption of momentum, mass and electrostatic transport as almost steady phenomena [142].

In this study, we focused on the effects of the geometry of the nanopore on the ionic current, velocity, ionic velocity distributions in the two and three dimensions. We narrowed down our study to the two different geometries (triangular and elliptical) of the nanopore. This is similar to the previous studies about the effects of dimensions of a converging-diverging nanopore on the translocation of a nanoparticle [315]. However, the effects of the surface charge of the nanopore and nanoparticle were not considered in our simulation. Our simulation would be more close to the practical translocation experiments if we consider the effects of surface charge densities similar to the simulations for a conical nanopore [139] in the future.

9.3. Simulation methodology

9.3.1. Modeling of the sensor structure

The FE model of a double nanopore-nanochannel sensor was built in COMSOL 5.0 Multiphysics software (www.comsol.com) [320]. The cross-sectional area of the nanochannel and two nanopores fabricated by using focused ion beam (FIB) were similar to half ellipses [321, 322]. For simplicity, an axisymmetric model was used for the simulation instead of building a model with half ellipse nanopores. Equivalent circles with the same areas as the half ellipses of the nanochannel and two nanopores were used in the modelling. Table 9.1. shows the calculated radii of the equivalent circles for the nanochannel and the top and down nanopores in the modelling. Figure 9.1 shows the schematics of the nanopore-nanochannel system. The distance between the two nanopores is 60 µm and the both top and down nanopores have 30 µm distance from the inlet and outlet microchannels.

Table 9.1. Cross sectional dimensions of the nanopores and nanochannel and their equivalent circular area

	Experiment	Simulation (Axisymmetric)
Geometry	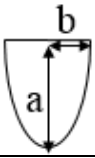	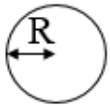
Area	πab/2	πR^2
Nanochannel	a=100nm b=50nm	R_{Ch}=50nm
Top Nanopore	a=(27/sin(52))nm b=48nm Length=100nm	R_t=28.68nm
Down Nanopore	a=(14/sin(52))nm b=46nm Length=100nm	R_b=20.21nm

9.3.2. Governing equations

The physics used in the FE model includes the fluid dynamics of water along with the ion transfer of the KCl solution. The FE model also includes the electrostatic voltage and current of the external electrical circuit connected to the ion transfer equation by applying the Poisson equation. In this section, we will discuss the abovementioned physics used in the simulation.

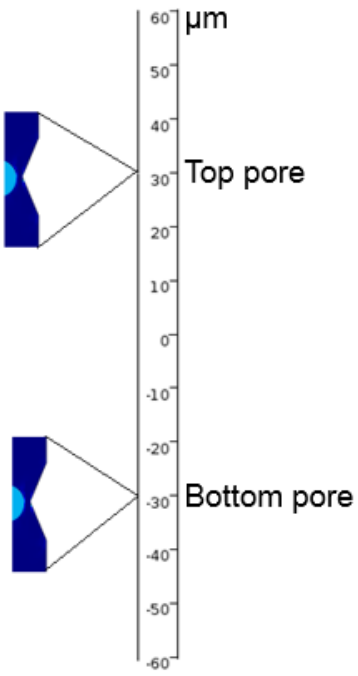

Figure 9.1. Schematics of the simulated nanopore-nanochannel system

9.3.2.1.Fluid dynamics

Equation (4) shows the Navier-Stokes equations in 3D space. The Navier-Stokes equation was used to simulate the fluid (water) flow in nanochannel with low velocities.

$$u\nabla u = \frac{1}{\rho}(-\nabla p + \eta\nabla^2 u - F(\sum_i z_i c_i)\nabla\Phi) \quad (4)$$

In which, u, ρ, ∇, p, η, Φ and F were the velocity vector, density of the fluid (water), gradient vector, pressure of the fluid, viscosity of the fluid, electric potential and Faraday's constant, respectively. In this equation, $\rho \times u\nabla u$ and ∇p represented the inertia term and external pressure applied to the ionic fluid and $\eta\nabla^2 u$ was the force induced by the viscosity of the fluid. In addition, $F(\sum_i z_i c_i)\nabla\Phi$ was the electroosmotic force applied to the fluid in which z_i and c_i were the charge of the species "i" (K or Cl), respectively [138].

9.3.2.2.Ion transfer

Equation (5) represented the Nernst-Plank equations used to simulate the ion transfers in the fluid because of the applied electric field.

$$J_i = (-D_i \nabla c_i - \frac{Fz_i}{R_{MT}T} D_i c_i \nabla \Phi + c_i u) \quad (5)$$

Where J_i and D_i were the ion flux vector and diffusion coefficient of species i. R_{MT} and T were the molar thermal resistance and the absolute temperature of the medium (KCl solution). The three terms on the right side of this equation represented the ionic flux caused by the diffusion, migration and convection of the ions. In addition, J_i, c_i, Φ and u were quantities that depend on the position of the fluid.

9.3.2.3. Constraints and constants

Equation (6) showed the last constraint, the Poisson equation.

$$\nabla^2 \Phi = -\frac{F}{\varepsilon} \sum_i z_i c_i \quad (6)$$

Where ε was the permittivity or dielectric constant of the KCl solution. The Poisson equation correlates the electric potential profile to the ionic distribution. Table 9.2 showed the values of the constants in the equations (4)-(6) used for the simulation. In which, V_{inlet} and V_{outlet} were the applied constant voltages to the inlet and outlet of the nanochannel, respectively.

9.3.2.4. Nanoparticles

We considered the nanoparticle by the wall boundary condition which was defined inside the nanochannel-nanopore structure. For the wall conditions, we chose no slip boundary which means that the velocity of the solution is equal to zero on the walls. Then we changed the location of the nanoparticle inside the nanochannel from the inlet to the outlet to simulate the translocation. Therefore, the particle was stationary at each location during the simulation. The shortest distance between the two locations of the particle was 0.05 μm in the proximity of the nanopores and 2 μm in the locations far from the nanopores.

9.3.3. Meshing

9.3.3.1. Mesh parameters

Two different in-plane (the plane parallel to the nanochannel direction) shapes for the geometry of the nanopore were modelled in the simulations. Figure 9.2 shows the sample

meshing of the down (smaller) nanopore with the two shapes. User controlled free triangular mesh was used for both of the simulations. An extremely fine mesh was used for the fluid dynamics simulations in the entire domain (nanochannel and nanopores) with maximum element size of 0.804 µm and minimum element size of 0.0024 µm and maximum element growth rate of 1.05. For the other physics in the simulation, we used a meshing with 1.2 µm maximum element size and 0.0024 µm, minimum element size with the 1.1 maximum element growth rate. In addition to the above setting, we used a corner refinement mesh for the nanopores and the particle (molecule) with the minimum angle between the boundaries of 240° and the element size scaling factor of 10^{-8}. Also two boundary layers with 0.804 µm thickness and 1.2 stretching factor were used for the meshing for the boundaries of the nanochannel and nanopores.

Table 9.2. Constants values for the double nanopore-nanochannel sensor simulation [323, 324].

Constant	Value
T	298 (K)
D_K	1.957×10^{-9} m^2/s
D_{Cl}	2.032×10^{-9} m^2/s
ε_{water}	80
η	1×10^{-3} Pa*s
ρ_{water}	1×10^{3} kg/m^3
c_0	1 mol/L
z_K	1
z_{Cl}	-1
F	96485 C/mol
R_{MT}	8.31 J/(mol*K)
V_{inlet}	1 V
V_{outlet}	0 V

9.3.3.2. Mesh convergence study

In order to check the properties of the mesh we used in our simulation, we performed a mesh convergence study on the nanoparticle translocation though a conical shape nanopore (e.g. simpler than our double nanopore-nanochannel sensor). We applied the constructive equations (9-12) to this simulation and chose the constants and boundary conditions from the reference [323]. Figure 9.3 shows the conical shape nanopore model we built in the software.

We selected the mesh setting based on references [320] and a mesh convergence study described in the next section.

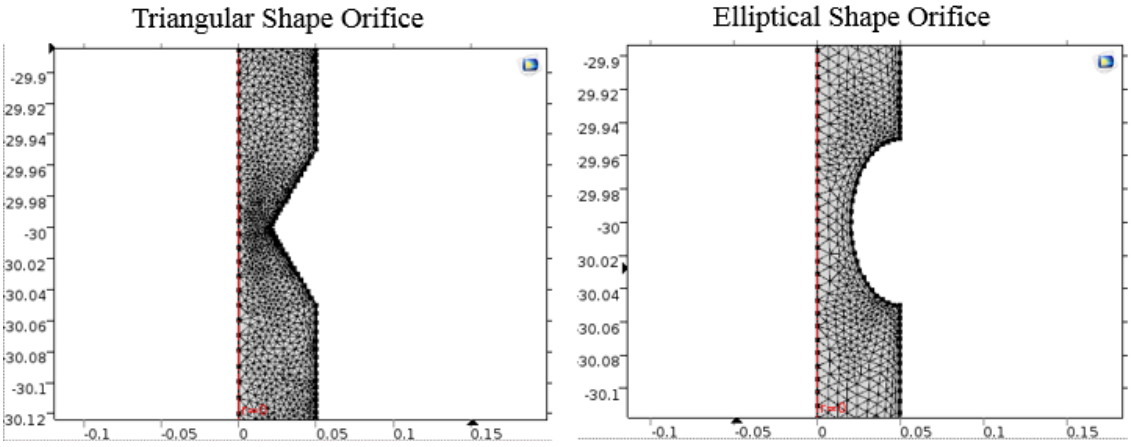

Figure 9.2. Meshing for the triangular and elliptical in-plane nanopore shapes

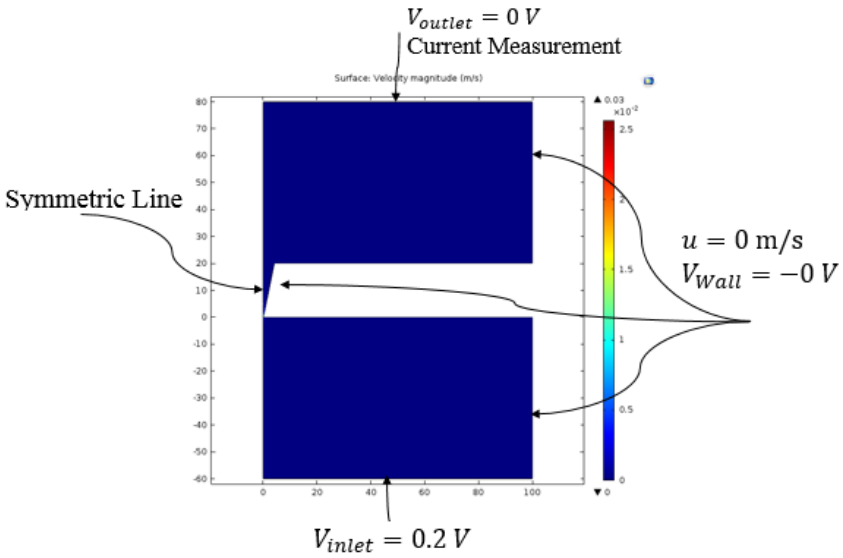

Figure 9.3. FE model of the conical shape nanopore [323].

In order to evaluate the effects of the mesh refinement on the current signal drop results, we performed three different simulations with separate mesh properties. Figure 9.4 shows the three mesh settings. The meshed models a) and b) are normal and extremely fine mesh while the meshed model c) is the extremely fine mesh with additional mesh refinements on the corners. These three mesh settings show that the mesh refinement on the corners also decreases the mesh sizes of the bulk solution in the simulation.

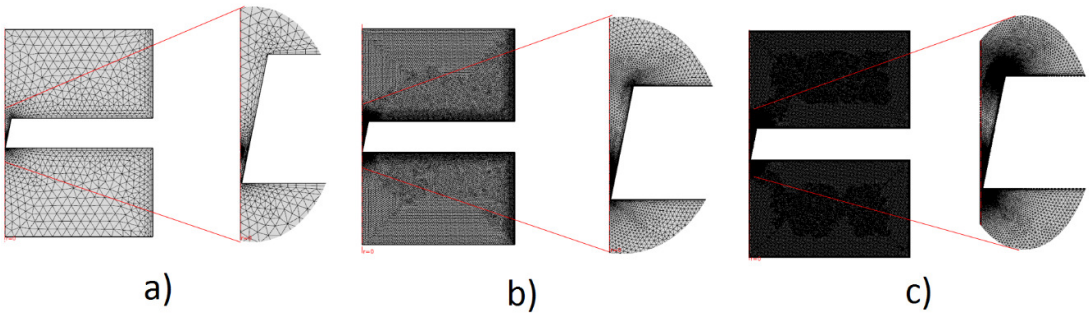

Figure 9.4. Conical shape nanopore simulation a) normal, b) extremely fine and c) modified extremely fine mesh

We run the three simulations with different mesh settings shown in the Figure 9.4 to derive the longitudinal ionic current signal during the translocation of the nanoparticle. Figure 9.5 shows the calculated ionic current drops when the nanoparticle reaches the conical nanopore. In this figure, the horizontal lines show the current base lines at which the nanoparticle is away from the nanopore region. The figure shows that the current drop signals has fluctuations near the inlet and outlet of the nanopore. The fluctuations for the normal mesh are in the order of 3 nA; however, they are less than 1 nA for the extremely fine mesh and less than 10 pA for the modified extremely fine mesh. Since the fluctuations shrink by the refinement of the mesh, they are the results of the mesh divergence. In addition, the comparison of the current drop derived from the modified extremely fine mesh with the one from the reference shows the convergence of the mesh. The setting of this mesh was applied to the double nanopore-nanochannel sensor simulation explained in the 9.3.3.1.

9.3.4. How simulation was done

Having the model, integrated physics and mesh, we can run the simulation to extract the ionic concentration and velocity distribution inside the nanochannel-nanopore at each position of the particle. We used a stationary study to solve the governing equations mentioned in section 9.3.2 simultaneously because the particle is static at each point during the simulation. By changing the particle (or the circular wall boundary condition) position, we calculated ionic

distributions and ionic current variations when the particle travels inside the nanochannel as well as the nanopores.

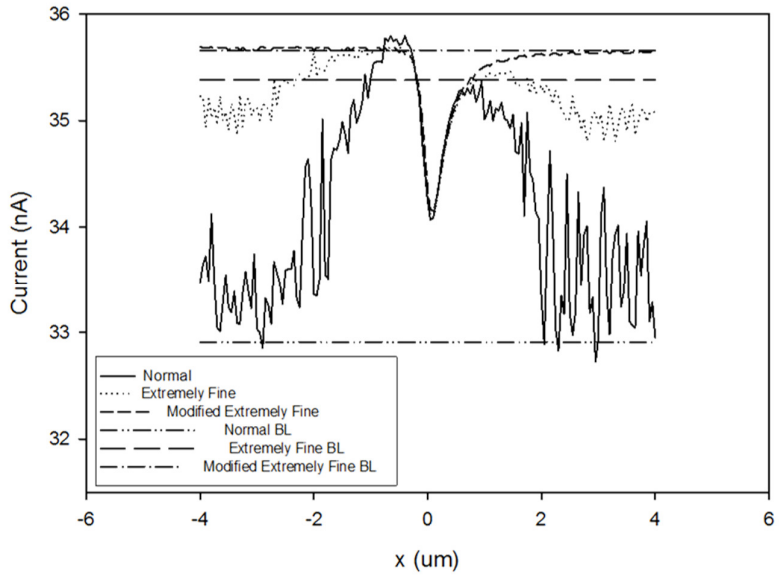

Figure 9.5. Ionic current drop signal of the three mesh settings

9.3.5. Interpretation of simulation results

The velocity profiles of the ions inside the nanochannel-nanopore structure relate to the ionic flux and ionic current inside the structure. In another words, we can estimate the local ionic current passing from the pore while changing the position of the particle. Also before running the simulation, we defined the integral of the sum of the fluxes of ions over the nanochannel outlet surface to determine the total ionic current variations. As we could predict, the ionic current variations were negligible while the particle position was far away from the nanopores. This ionic current is called the baseline current. However, the ionic current variations were higher when the particle approach to the nanopore. Thus, we have to change the particle position more slowly to record the ionic current variations in this region.

9.4. Simulation results

In this section, we derived the velocity profiles of the ions inside the KCl solution for the entire double nanopore-nanochannel sensor while there is no particle inside the channel and

the electric potential was applied to the inlet and outlet of the nanochannel. These profiles were used to indicate the difference in ions velocity distribution while using the triangular or elliptical in-plane shape for the nanopore. Then, the ionic current fluctuations versus the position of the molecule were computed to compare the ionic current baseline and the ionic current drops for the two shapes of the nanopores.

9.4.1. Ion velocity profiles without a nanoparticle

Figure 9.6 shows the velocity magnitude of the ions inside near the top and down nanopores for the two simulations. The velocity profile near the small (top) triangular nanopore has higher velocity gradients than the one for the elliptical nanopore. This is due to the sharp corners of the triangular nanopore. This is more obvious around the smaller nanopore geometry. The sharp corners might also increase the error in the simulation results. Nevertheless, the magnitude of the velocity of the ions around the nanopores for the triangular shapes is 10^2 orders larger than the one for the elliptical shape. This happens because the triangular nanopore exclude a smaller amount of ions from the solution than the elliptical nanopore.

We used a 3D axisymmetric geometry to simulate the ionic current flow in the double nanopore-nanochannel sensor for both triangular or elliptical nanopore shapes. Figure 9.7 and Figure 9.6 shows the 2D and 3D velocity profiles of the ionic solution inside the geometry. The 3D model shows clearly that the elliptical nanopore excludes more ionic solution from the nanochannel than the triangular nanopore does. Thus, the overall velocity distribution of the ionic solution inside the triangular nanopore is higher than the one inside the elliptical nanopore. The advantage of using an axisymmetric simulation such velocity profile is the ability to check the effects of the nanopore geometry on the velocity profiles. The drawback of this simulation is simplifying the actual geometry of the nanopore in the experiment to an axisymmetric model.

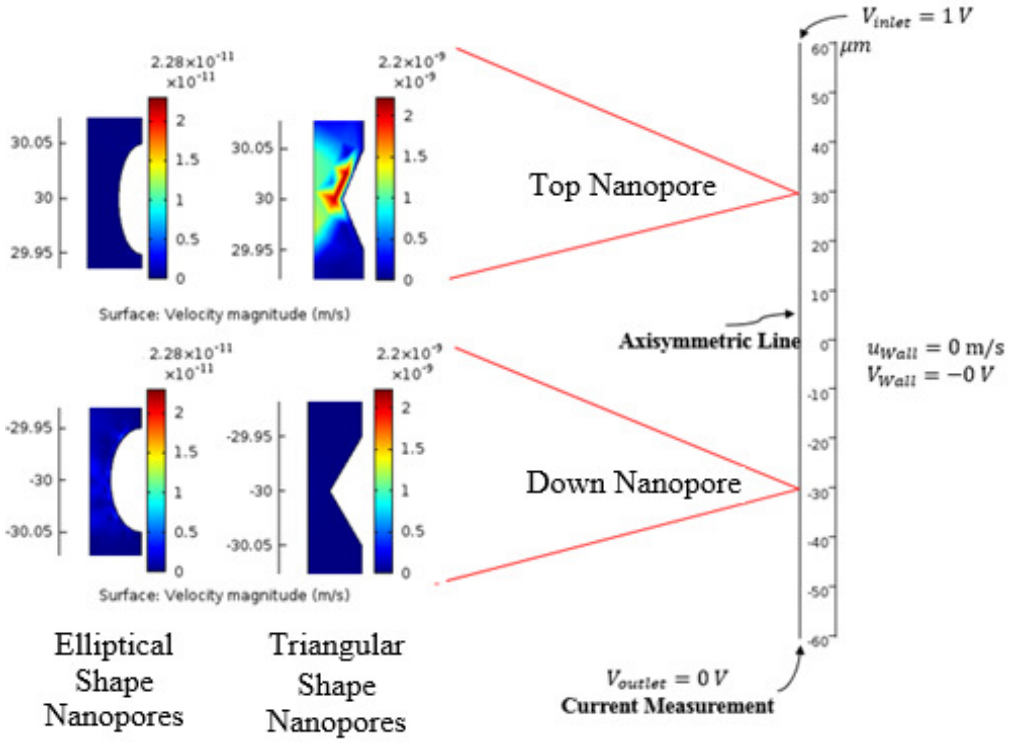

Figure 9.6. Velocity profiles of the nanochannel-nanopore simulation in two dimensions

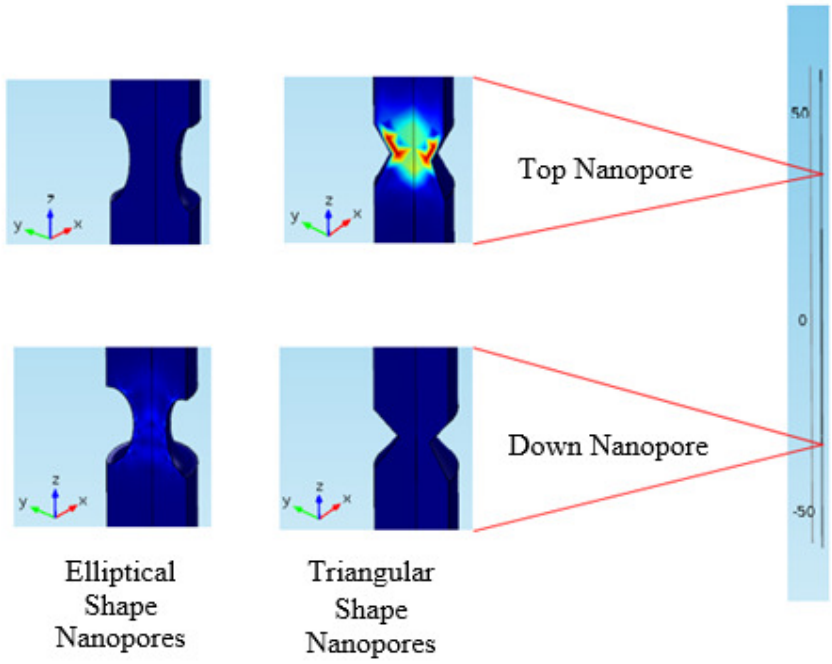

Figure 9.7. Velocity profiles of the nanochannel-nanonanopore simulation in three dimensions

9.4.1. Ion velocity profiles for a particle translocation

Figure 9.8 shows the ionic current variations during the translocation of a particle inside the nanochannel. The schematics (black and red) of double nanopore-nanochannel sensor indicate the location of the particle on the ionic current fluctuations signal. Figure 9.9 shows the ionic current drops zoomed on the top and bottom nanopores of the two simulations. The ionic current was calculated by integrating the total ionic flux of the two species (K and Cl) over the area of the nanochannel outlet (having zero electric potential). The schematics of the particle with the nanopore (blue and green) in Figure 9.9 distinguish the nanopore shape of each current drop signal. Also in both figures the ionic current from the triangular nanopore simulation was shown by a straight line while the one from the elliptical nanopore simulation was shown by a dotted line.

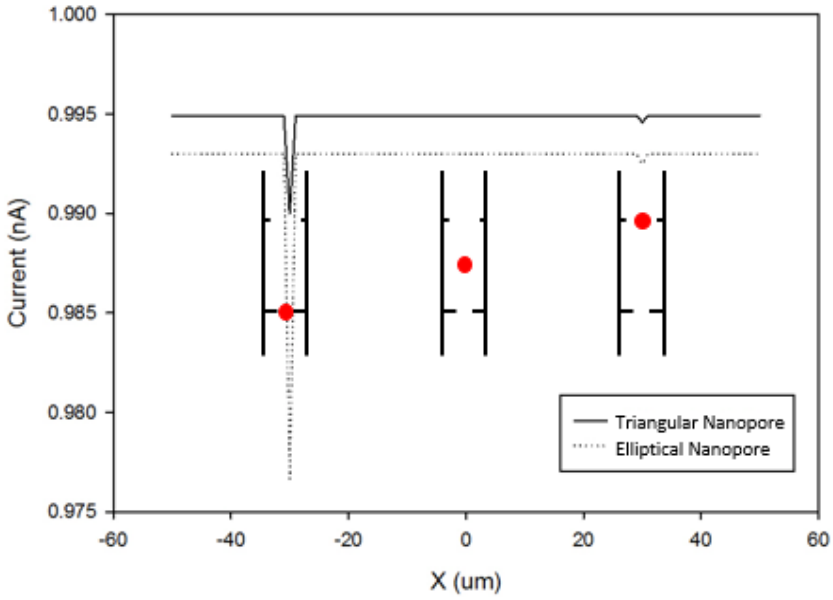

Figure 9.8. Ionic current drops during the translocation of the particle

Figure 9.8 and Figure 9.9 show that the ionic current baseline of the model with triangular nanopores is higher than the one of the elliptical nanopore model. This is because the elliptical nanopore in the later model excludes a larger amount of ionic solution from the nanochannel than the triangular nanopore in the former model does. Consequently, the double

nanopore-nanochannel sensor with the elliptical shape has a higher total resistance than the one of the triangular shape. This also explains the higher amount of current drop at the nanopore with elliptical shape when the particle reaches the nanopore. A lower velocity of the ionic flow around the elliptical shape nanopore results in a higher current drop by approaching the particle to the nanopore.

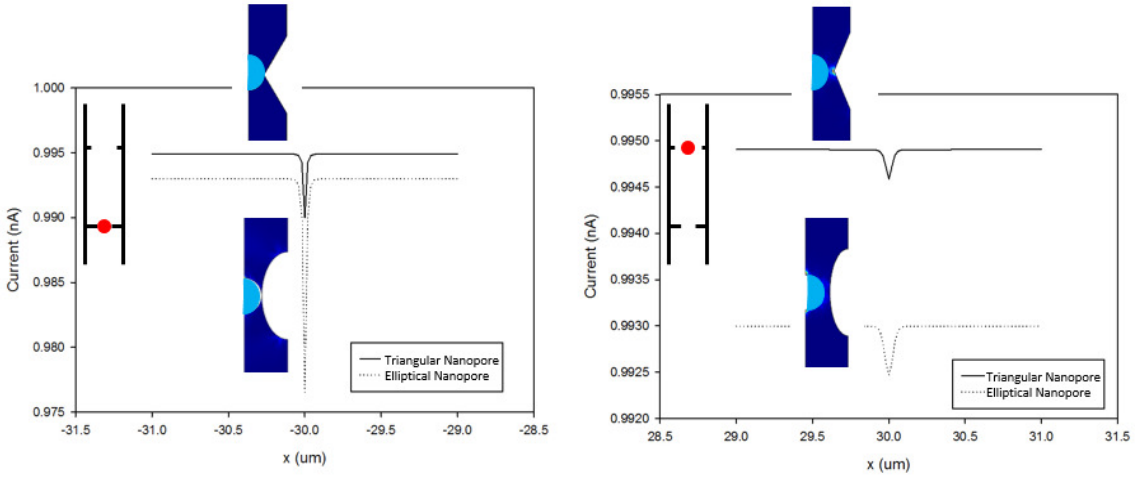

Figure 9.9. Ionic current drop at down nanopore (left) and top nanopore (right)

9.5. Conclusion

The translocation of a single particle from the double nanopore-nanochannel sensor with nanochannel structure was numerically simulated. The results of this study about the effects of the nanopore geometry on the current drop can be used to design the nanopores in the experiment. However, the experimental methods (e.g. focused ion beam (FIB)) are limited in fabricating nanopores with arbitrary shapes. In addition, further simulation studies are required to optimize the current drop signal value due to the nanoparticle translocation through each nanopore by changing the relative sizes of the nanopores and the geometry of the nanochannel.

Chapter 10. Integrate The Nanoelectrode And Nanofluidics.

10.1. Introduction

Distinguishing various DNA molecules with different physical properties is vital for applications such as diagnosis of the diseases [11] and prenatal tests [325]. In the first application, the target is to differentiate the DNA molecules that are modified because of chemical reactions caused by the disease from the normal DNA molecules. One example is the detection of the DNA methylation that can be caused by the addition of methyl groups –CH3 to cytosine-guanine sites (CpG dinucleotides). This can happen in the forms of hypermethylation and hypomethylation that correspond to the additional and inadequate methylation compared to the normal DNA. Since the methylation can modify the genes activities that can be transferred during the division of the cells, it can cause several diseases. Biological and solid state nanopores were used to detect the methyl proteins in dsDNA and ssDNA. The translocation of methylated DNA caused a current blockage different from the methylated DNA, namely, for 5-methylcytosine is higher than the unmethylated DNA. This can be contributed to the different diameter of the stretched DNA of each type that can result in different mass of each molecule type [326]. The latter can also be used to differentiate the methylated and unmethylated DNA molecules. Labeling methylated sites with protein [327] or reversible Hg+ ions [328] were also reported to enhance the discrimination between the methylated and unmethylated proteins. In the second application, the target is to differentiate between the maternal and fetal cell free DNA molecules of a pregnant human plasma. The significance of this study is to determine the fetal to maternal DNA fraction and reduce the number of false negative results when this fraction is low. Both cell free molecules have less than 200 base pairs; however, generally the fetal DNA molecules have shorter lengths than the maternal ones. Thus, for the samples with higher fetal DNA molecules, the average length of the molecules is lower than the samples with lower fetal DNA molecules. The variations in

length can be used to differentiate the two types of plasma samples taking the advantage of different translocation time through nanopore [325].

For these applications, the variations of physical properties of the DNA molecules (e.g. length, chemistry, etc.) is the key factor to discriminate the DNA molecules of each type. High sensitivity (single molecular) discriminating especially for the molecules with low concentrations is very important to determine the diseases at their early stages [11]. Among the main mechanisms to detect single molecules, electrical methods can be more easily combined with electrical components and CMOS systems from which nanopore sensors attracted many attentions [329]. In a nanopore sensor, passing a molecule from a pore that separates two reservoir containing ionic solution induce a change (event) in conductance of the nanopore that can be measured. The magnitude and duration of the event represents the properties (length, charge and conformation) of the molecules [330]. Detection of bio molecules (DNA nucleobases, biomarkers and protein complexes) using nanopore sensors requires the detection of relative location of the molecules passing through the pore [331]. The challenges of nanopore sensors to detect single molecules include fabrication limitations of the device design [332], inability to control the molecular translocation speed [333], stochastic factors [334] and the requirement for high number of events for the statistical analysis [335]. In terms of the device design, the nanopore diameter has to be selected based on the dimensions of the analyte (i.e. less than 5 nm for 2 nm diameter DNA, above 10 nm for antibodies attached to DNA and so forth) [336]. Fabrication of such small nanopores is a very challenging task. On the other side, the thinner pores have higher spatial resolution that is in conflict with their higher noise level and lower translocation dwell time [332]. Assuming the translocation time for a 10 kbp DNA (i.e. 3.4 μm long) attached to a 10 nm antibody around 1ms, therefore, the total time for the antibody to stay inside the pore is approximately 3 μs [333]. Detecting a fast event like this with errors in current around hundreds of picoamps is almost impossible. Using nanopore

materials with low dielectric factors or changing the electrolyte material from KCl to LiCl are recommended to reduce the translocation speed [337]. Characterization of single molecules and biomarkers (e.g. antibodies) on the DNA molecules requires knowing the speed of the translocation. However, the speed of the translocation varies due to the existence of random oscillations [334]. For the statistical analysis, hundreds of events are required to obtain valid information. Increasing the concentration of the solution can increase the frequency of the events but it can result in clogging and multiple events. Using the right electrolyte solution [337] and surface modification [335] can be used to decrease the translocation speed thus increase the number of meaningful events.

In this chapter, we completed the integration of nanochannel-nanopores sensor with an intermediate nanoelectrode fabricated on a plastic substrate introduced in the first chapter to enhance the single molecular detection accuracy of the nanopore sensors by measuring the time of flight (TOF) of the molecule between the two nanopores. The nanochannel directs the molecule between the two nanopores while the intermediate nanoelectrode is used to measure separately the ionic current passing from each nanopore. In terms of device design, the double nanopore sensor with double electrical circuits increases the chance to detect the meaningful events by correlating the signals from each nanopore separately. The lower dielectric loss factor of the plastic materials than the silicon-based materials helps reducing the translocation speed. In terms of the device fabrication, the transverse nanoelectrode should be in the nanochannel fluidics while it is connected to the external power supply through microelectrodes. The micro-/nanoelectrodes should be embedded inside the nanochannel substrate and cover sheet to prevent leakage from the nanofluidic devices after bonding. Here we introduced a new optimized fabrication condition for the embedded nanosensor and their integration with the nanofluidic devices. The dimensions of the nanochannel and nanopores and the electrical resistance of the nanoelectrode should be determined before and after cover bonding the

nanofluidics. Also, the molecule translocation through each pore should be demonstrated using the current drops from the separate electrical channels.

10.2. Experimental

10.2.1. Fabrication and preparation process of the micro-/nanoelectrodes on double nanopores-nanochannel for electrical measurement

Figure 1 shows the schematic process steps to install the micro-/nanoelectrodes on the micro-/nanochannel and nanopores to fabricate the sensor device with an intermediate nanoelectrode. Two microchannel patterns with 10 µm depth similar to the ones shown in Figure 1(a) were fabricated on silicon wafer using the conventional photolithography and wet etching on silicon/silicon nitride wafer. The micro-/nanochannel patterns from the silicon substrate were copied into Poly Urethane Acrylate (PUA) on Polycarbonates (PC) substrates using Ultraviolet (UV) lithography and then copied from the PUA molds into Poly methyl methacrylate (PMMA) substrates using Nano Imprint Lithography (NIL, Obducat). Four 1 mm holes were drilled into the access reservoirs of the microchannels using a micro-drill (MicroMark). Figure 1(a) and the inset show the schematics of the microchannel and nanochannel on the PMMA substrates, respectively. In order to fabricate and align the microelectrode pair with the nanochannel on the PMMA substrates, stencil lithography using SU8 membranes was used. A 2 µm SU8 membrane was fabricated on a 250 nm Dextran layer on a silicon wafer using photolithography and was transferred and aligned on the nanochannel using a thermal release tape. Figure 1(b) shows the schematics of the membrane on the PMMA substrate and the inset shows the tips of the microelectrode pair pattern on the stencil membrane. A thin layer ~24 nm of Pt was deposited on the stencil membranes using sputtering followed by lift off the stencil membranes. After fabricating the microelectrodes, optical microscope alignment was used to place an FeNiCo nanowire with 200 nm diameter and more than 50 µm length from a blank Polydimethylsiloxane (PDMS) substrate to the microelectrodes by thermal imprinting (35 bar, 90°C and 5 min). The details of the fabrication of the

microelectrodes using SU8 stencil membranes, synthesis of the nanowires, the nanowires alignment and their thermal imprinting on the microelectrodes using the optical microscope were explained in our previous works.

Figure 1(c) shows the schematics of the assembled device with open micro-/nanochannel and the inset shows the configuration of the nanowire, microelectrode, nanochannel and nanopores on the PMMA substrate. The open micro-/nanochannel with nanoelectrode was covered by 0.1 mm Cyclic Olefin Copolymer (COC) (TOPAS 8007) sheets using the thermal bonding between the COC and PMMA. Figure 1(d) shows the complete device with COC sheets covered the microchannel reservoirs while left the access points of the microelectrodes open. Figure 1(e) shows the complete device from the back in which reservoirs provided the electrical access to the microchannels and the nanochannel while microelectrodes connected the nanoelectrode on the nanochannel the outside world. The micro-/nanochannel was filled with 1M KCl solution and Ag/AgCl wires were used to connect the microchannel reservoirs to a commercial Axon patch clamp (Molecular Devices Inc.) Separate electrical channels were used to apply voltage between the microchannel inlet and nanoelectrode (I-V1 in figure 1(d)) and the microchannel outlet and nanoelectrode (I-V2 in figure 1(d)) while their currents were measured independently. Thus, the electrical channels could independently drive current (or molecule) into the first and second nanopores by applying separate voltages.

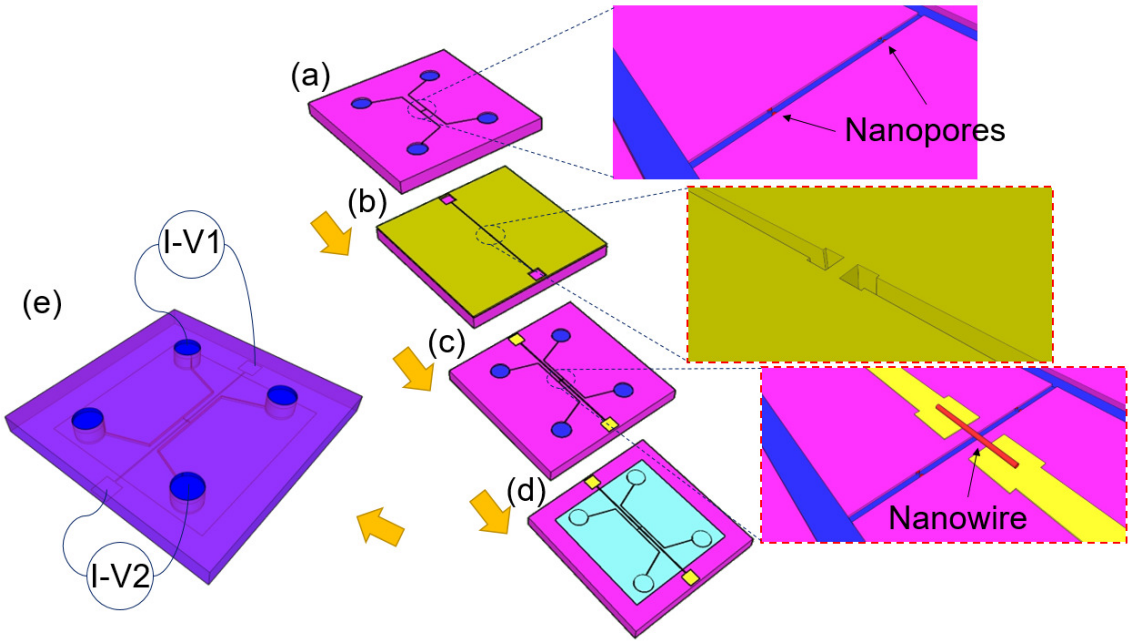

Figure. 10.1. Fabrication and installation process for the nanoelectrode sensor on the nanochannel-nanopores structure on plastic substrate: (a) imprinting the micro-/nanochannel into PMMA substrates and insert holes into the microchannels reservoirs, (b) alignment of the microelectrode pair pattern on the stencil mask between the two nanopores on the nanochannel, (c) sputtering, Pt, lift-off the mask and alignment and placement of a single nanowire to the microelectrode pair, (d) covering the open micro-/nanochannel with COC sheets using thermal bonding and (e) Insert KCl solution into the nanochannel through the reservoirs and perform the electrical measurement using separate channels (I-V1 and I-V2).

10.2.2. Optimization of the nanochannel-nanopores thermal pressing and bonding conditions to embed the micro-/nanoelectrodes in the substrate and cover sheet

The microelectrode and nanowire shown in the inset of Figure 1(c) were partially embedded in the PMMA substrate because of the thermal imprint using the blank PDMS substrates used to transfer the nanowires thermally to the microelectrodes. The partially embedded nanoelectrode prevents the complete bonding between the PMMA substrate and COC cover sheet especially close to the microelectrode pair and nanowire. This causes leakage of the KCl solution from the nanochannel after the complete assembly of the device. In order to prevent this issue, we studied the maximum possible temperature and pressure that can be used to bond the micro/-nanochannel PMMA substrate to the COC cover sheet without blocking the nanochannel. Thus, we used these maximum bonding conditions in the same bonding time (15 min for all samples) to push the microelectrode and nanowire into the COC

cover sheet as well as the PMMA substrate and prevent leakage. Since the majority of the nanochannel (~80%) was not surrounded by the microelectrodes and for simplicity, we used the pure micro-/nanochannel without the electrodes for this study. For each applied bonding temperature and pressure, four samples were prepared and the electrical resistance of the nanochannel from each sample was measured. Since the diameter of the nanochannel and nanopores were reduced because of the applied pressures and temperatures at each step, the diameter of the nanochannel and nanopores were calculated using the electrical measurements.

Figure 10. 2 shows the results of electrical resistance of the nanochannel-nanopores (a), equivalent total resistance schematics of the nanochannel and nanopores (b) and the subsequent nanochannel and nanopores diameter calculated from their equivalent total resistance (c). Figure 10. 2(a) shows the measured resistance of the nanochannel-nanopores versus the applied substrate preparation and bonding condition. The first condition was used as a reference with the minimum applied bonding temperature and pressure (5 bar and 70°C for 15 min) and without thermal imprinting of the PMMA substrate using blank PDMS substrates. The thermal pressing by flat PDMS (TPFP) was added before the bonding process for the other conditions to better simulate the nanochannel size alteration after the placing the nanoelectrode on the nanochannel substrate. The applied pressures varied from 5 bar to 20 bar by keeping the temperature constant at 70°C. Applying a pressure below 5 bar was not possible using the NIL while the PMMA substrates and COC cover sheets could not bond to each other below 70°C applied bonding temperature. Above 70°C, we applied 80°C bonding temperature and 5 bar bonding pressure which caused blocking of the all of the nanochannels since 80°C is the glass transition temperature of the COC cover sheets. Above 20 bar, we applied 30 bar pressure and 70°C for bonding which caused partially detachment of the COC cover sheets from the PMMA substrates especially around the microchannels and their reservoirs. Applying 40 bar pressure and 70°C for bonding caused the detachment of the COC cover sheet in the majority of the

substrate surface which prevented us from the electrical measurements. The detachment of the cover sheet at higher pressures was due to the insertion of the COC cover sheet into the reservoirs holes and micro-/nanochannels that caused the detachment of the bonding in their surrounding area. Overall the increment of the electrical resistance of the nanochannel-nanopores by increasing the bonding pressure up to 20 bar denoted the decrease of the nanochannel and nanopores dimensions.

In order to calculate the diameter of the nanochannel and nanopores at each step, the diameter of the two nanopores were assumed to be the same at each bonding condition. Also, the diameter reduction of the nanochannel and nanopores was assumed to be the same at each bonding condition. Therefore, for the first condition (5 bar, 70°C), the diameter of the nanochannel was measured from the scanning electron micrograph (SEM) of the nanochannel and the diameter of the nanopores was calculated from the electrical measurement from the nanochannel-nanopores. For these calculations, the nanochannel and nanopores were assumed as parallel resistors shown in the Figure 10.2 (b) in schematics, for which the resistivity formula could be written similar to the Equation (1):

$$R_T = \frac{V}{I} = \sum R_i$$
$$R_i = \frac{4 \times \rho_{1M\ KCl} L_i}{\pi d_i^2} \quad (1)$$

In which, R_T is the total resistance of the nanochannel-nanopores and R_i is the resistance of either nanochannel or nanopore. Also, $\rho_{1M\ KCl}$, V and I are the resistivity of 1M KCl solution, applied voltage and measured current from the nanochannel-nanopores, respectively. Also I = NC (Nanochannel), NP (Nanopore), L is length and d is diameter of the nanochannel or nanopore. For all other (than first) conditions, the diameter of the nanochannel and nanopores were calculated by calculating their diameter reduction using the electrical measurements and deducting from the initial values of their diameters. Figure 10.2 (c) shows the calculated

diameters from the electrical measurements at each applied bonding condition. The results show that the maximum diameter reductions both for the nanochannel (8.8%) and the nanopores (85.0%) happened at the step with thermal pressing with flat PDMS (TPFP) and the bonding pressure at 5 bar. While the diameter of the nanopores were reduced by 63.9% and 5.4% by increasing the bonding pressure to 10 bar and 20 bar, respectively, the diameter of the nanochannel was reduced less than 1% by increasing the bonding pressure. This is expected since the diameter of the nanopores were significantly smaller than the nanochannel therefore the electrical resistance of the device was mainly controlled by the dimensions of the nanopores. Since by applying the maximum pressure of 20 bar the nanochannels were still conductive, we used this pressure for the bonding process of the final device.

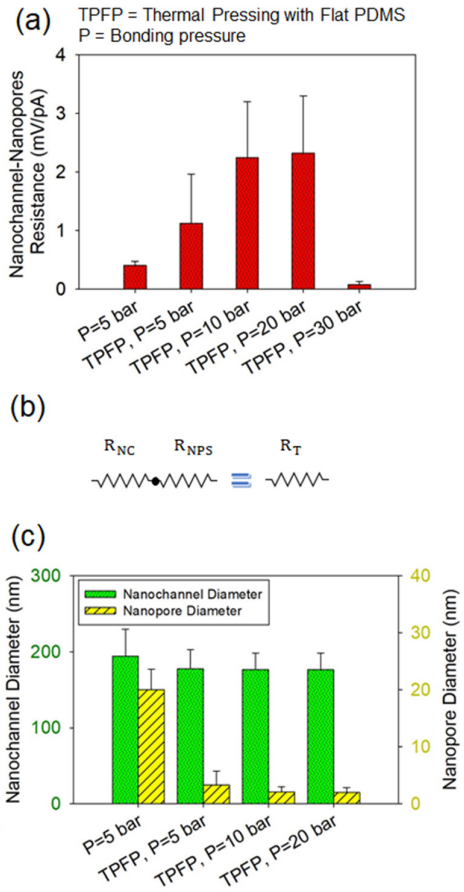

Figure. 10.2. Summary of the measured nanochannel and nanopore (a) measured electrical resistance by inserting 1M KCl solution, (b) equivalent resistance serial circuit of the nanochannel and nanopore and (c) diameters of the nanochannel and nanopores at each bonding condition. The green and yellow bars show the calculated diameter of the nanochannel and nanopores, respectively.

10.3. Results and discussion

10.3.1. Optical and fluorescent micrographs of the micro-/nanoelectrodes on the nanochannel-nanopores

Figure 10.3 shows the optical micrographs of the open ((a), (b)) and bonded ((c), (d)) micro-/nanochannel for two samples for which the first sample only had the microelectrode pair ((a), (c)) and the second sample had microelectrode pair together with the nanowire (b), (d). The bonding condition used for the first sample was (5 bar and 70°C) without TPFP while the bonding condition used for the second sample was (20 bar and 70°C) with TPFP. In comparison with the open nanochannel that has been imprinted thermally by a flat PDMS substrate (Figure 10.3 (b)), the nanochannel without thermal imprinting (Figure 10.3 (a)) had a higher contrast which could be due to the diameter reduction of the nanochannel after the thermal imprinting. Figure 10.3 (c) shows that for the first bonding condition (Figure 10.2 (a, c)) or (5 bar and 70°C) without TPFP the cover sheet had significant detachment close to the microelectrode pair as well as in the gap between the electrode pair. Conversely, Figure 10.3 (d) shows that the bonding condition (Figure 10.2 (a, c)) or (20 bar and 70°C) with TPFP resulted in a good bonding of the cover sheet to the nanochannel substrate including the areas around the microelectrode pair and the nanowire.

In order to better study the bonding and leakage from the nanochannel after the bonding of the cover sheet using the last bonding condition shown in Figure 10.2 (a, c) (20 bar and 70°C) with thermal imprinting of the nanochannel using flat PDMS substrates, we inserted fluorescent dye into the nanochannel. Figure 10.4 (a-c) show the results of this study for the nanochannel inlet and outlet ((a), (c)) and the middle of the nanochannel (b) between the microelectrode below the nanowire (shown by the red arrow). Overall, no leakage was observed from the nanochannel by observing the fluorescent micrographs.

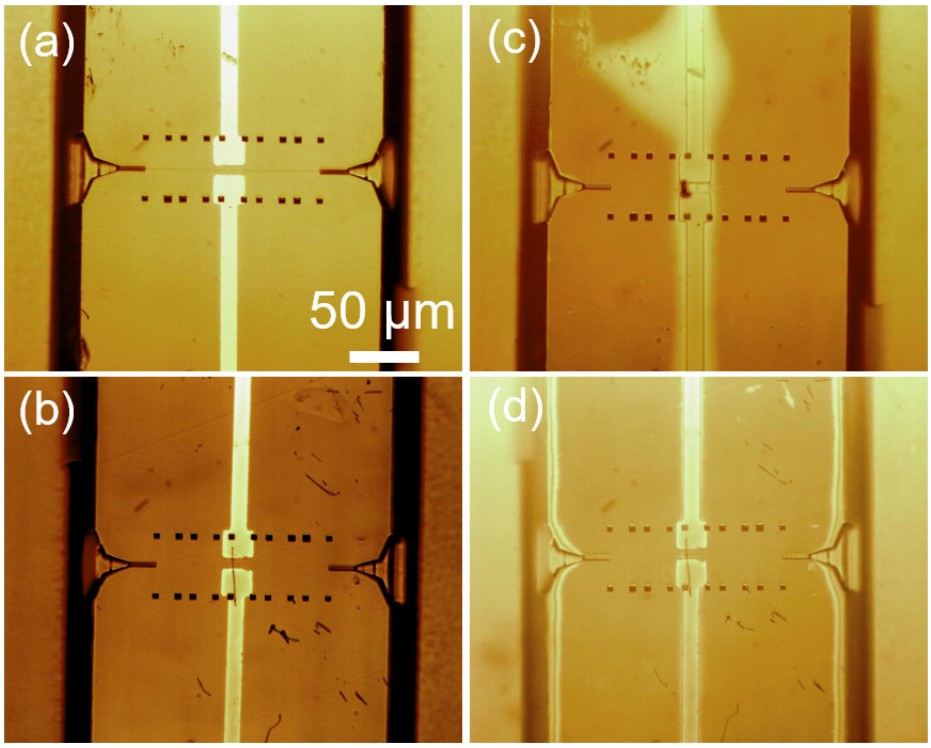

Figure. 10.3. Optical micrographs of the micro-/nanoelectrodes on (a) open and (b) covered nanochannel-nanopores. (a, c) show the results of the first sample only with microelectrode pair before and after bonding of the cover sheet, respectively and (b, d) show the results of the second sample with microelectrode pair and nanowire before and after bonding of the cover sheet, respectively.

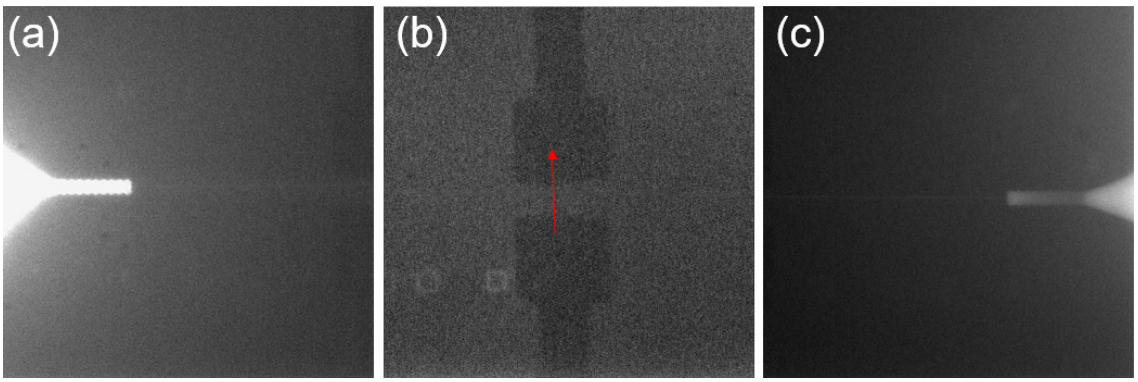

Figure. 10.4. Fluorescent micrographs of the complete device with microelectrode and nanowire after filling the fluorescent dye showing the (a, c) nanochannel inlet and outlet and (b) the nanochannel between the microelectrode pair. The red arrow indicates the location of the nanowire in the fluorescent image.

10.3.2. Comparison of nanochannel-nanopores resistance before and after placing the micro-/nanoelectrodes

Table 10.1 shows the measured nanochannel-nanopores electrical resistance of the pure samples without micro-/nanoelectrode and with micro-/nanoelectrode versus the first and last

bonding conditions shown in the Figure 10.2 (c). Similar to the samples without nanoelectrodes, four samples with micro-/nanoelectrodes were used for these measurements. The success rate of the nanowires transfers to these samples were 100 ± 1%. The nanochannel-nanopores samples in the presence of the microelectrodes at 5 bar bonding pressure without thermal imprinting showed a significantly lower electrical resistance than pure nanochannel-nanopores samples due to the detachment of the COC cover sheet from the nanochannel PMMA substrate shown in Figure 10.3 (c). In contrast, the nanochannel-nanopores samples in the presence of the microelectrode pair and nanowire represented a higher electrical resistance because of the partially blockage of the nanochannel during the thermal transfer of the nanowire.

Table. 10.1. Summary of the nanochannel-nanopores measured electrical resistance values for the blank samples and for the samples with micro-/nanoelectrodes bonded with the first and last conditions shown in the Figure 10.2 (a, c).

TI = Thermal Imprinting P = Bonding pressure	Integration conditions	Without electrodes	With electrodes
Nanochannel-nanopores resistance R (mV/pA)	No TI, P=5 bar	0.40 [±0.07]	0.05 [±0.02]
	TI, P=30 bar	2.32 [±0.98]	2.92 [±0.56]

10.3.3. Micro-/Nanoelectrodes resistance, nanowire resistivity and nanowire-nanochannel interface contact resistance

Figure 10.5 (a-c) show the schematics of the nanoelectrode chip assembled with the nanofluidics before and after bonding the cover sheet and their corresponding electrical measurement results. The 2-probe resistance of the microelectrodes and nanowire was measured using a DY2300 series potentiostat by measuring the current from the contact pads of the microelectrode pair before and after placing the cover sheet shown in the Figure 10.6 (a, b), respectively. Four samples were used for each measurement. Using the resistance values before placing the cover sheet and the calculated resistance of the microelectrodes from

previous studies on the microelectrodes properties, we calculated the 2-probe resistance of the nanowires. Figure 10.5 (c) shows the results of the microelectrodes and nanowire 2-probe resistance values before and after bonding the chips in red and the nanowires 2-probe resistance values in blue. Since the microelectrode pair is very thin (24 nm) and narrow (10 µm), the resistance of the microelectrode pair was two orders of magnitude higher than the nanowire. Also, the bonding introduced defects in the microelectrodes which increased the resistance of the microelectrodes.

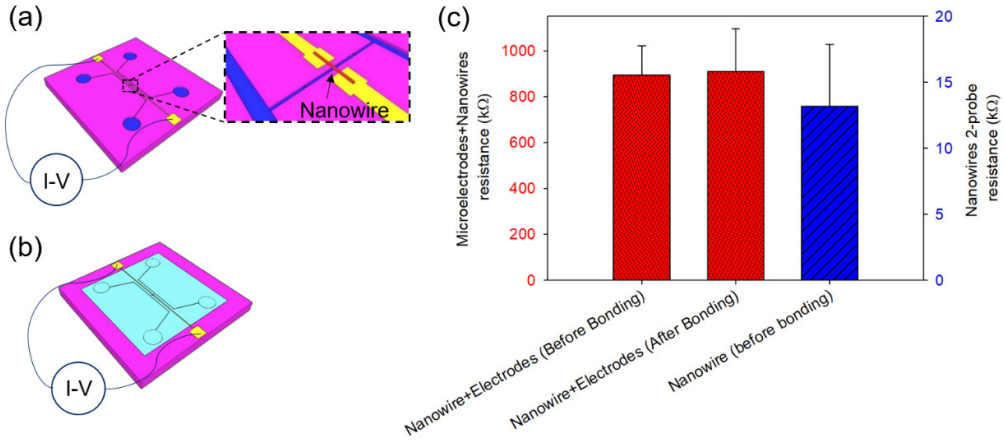

Figure. 10.5. The schematics of the micro-/nanoelectrode integrated with the nanofluidics (a) before bonding and (b) after the chip and (c) the summary of the microelectrode pair + nanowire measured electrical resistance values before and after bonding (green bars) and the calculated nanowire resistance (the blue bar).

Since we excluded the resistance values of the microelectrodes by assuming that their dimensions were constant while the thickness of the sputtered Pt varied for different samples, these caused errors in the calculation of the nanowires 2-probe resistance values. Using the derived microelectrode and nanowires resistances and the currents measured through the microelectrode, nanowire and nanochannel, the contact resistance between the nanoelectrodes and nanochannel interface was calculated 5.67±0.896GΩ. This value was orders of magnitudes higher that the resistance values of the nanowires and microelectrodes which was attributed to the small contact area between nanowire and nanochannel.

10.4. λ-DNA translocation results from individual pores

In order to demonstrate the functionality of the device in detection of translocation events from each nanopore separately using the transverse nanoelectrode, we used λ-DNA translocation through the nanochannel and nanopore and measured the current drops from each nanopore using the transverse nanoelectrode. Figure 5(b) shows the assembled device in the presence of the KCl solution inside the reservoirs and the micro-/nanochannels. Two pieces of copper tape were attached to the access points of the microelectrodes shown in the figure 1(d) and figure 1(e) to provide access to the microelectrodes from the backside of the device. Since each microchannel was connected to two reservoirs, each could be used to connect the device to the patch clamp for the subsequent electrical measurement.

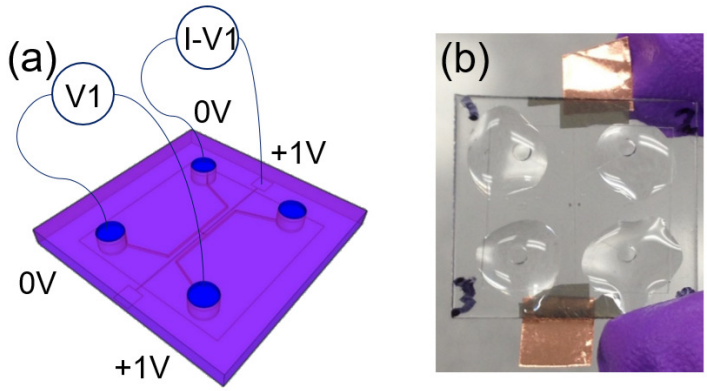

Figure. 10.6. The assembled chip (a) schematics and (b) actual filled with 1M KCl solution. The circuits V1 and I-V1 in the (a) represent the constant voltage applied by the power supply and constant voltage while measuring current using the patch clamp, respectively.

The negatively charged λ-DNA molecules were added to the 1M KCl solution and inserted from the 0 V side of the nanochannel. The applied current V1 was kept constant between the nanochannel inlet and outlet using a commercial power supply while the current was recorded using a commercial patch clamp between the nanoelectrode and nanochannel inlet and outlet at different times (not simultaneously). Using a single channel patch clamp and a power supply, the translocation of λ-DNA was measured from each pore (not simultaneously) to test the functionality of the device and the two separate channels. Figure 10.7 shows the

single events from translocation of the molecule from each pore showing the functionality of the two electrical channels connected to the pores to detect the translocation events.

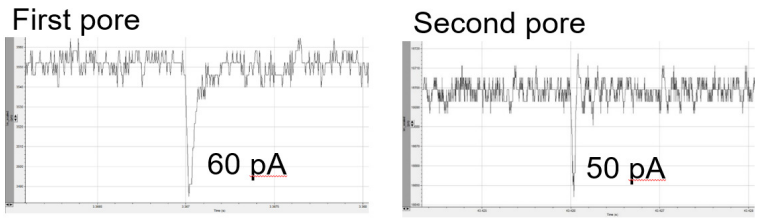

Figure. 10.7. Current drops from the first and second nanopores.

10.5. Conclusion

A new high throughput technique was introduced to integrate a high precision nanochannel double nanopore sensor device on plastic substrates with an intermediate nanoelectrode for the characterization of biomolecules. The device enabled the user to drive the molecules inside the nanochannel-nanopores and measure the ionic current drops independently while the molecule passed through the first nanopore or the second nanopore and measure the time of flight of the molecule between the two nanopores. This eliminates the errors in measuring the time of flight of the molecules because of the overlap issues of the current drop signals. The introduced technique caused reducing the nanopore and nanochannel diameter by ~80% and ~9%, respectively, that could be used as an advantage of the method to detect smaller molecules. The optical, electrical and fluorescent tests were implemented on the device to test the device assembly, conductivity and leakage. The device also enabled the user to measure the resistance and resistivity of the nanoelectrode as well as the contact resistance between the solid electrode and fluid medium. The functionality of the nanoelectrode was demonstrated by detecting the translocation of the λ-DNA molecules using the nanoelectrode separately from each nanopore. To our knowledge, this is the very first device on plastic substrates able to conduct molecules into a single nanochannel with two nanopores connected

to two independent electrical channels and can revolute the biosensing and micro-/nanoelectronics industry.

Chapter 11. Future Work

11.1. Nanogap insert into nanoelectrodes

In principal, one can insert a nanogap into the nanowire at the intersection between the nanowire and nanochannel before or after placing the nanowire on the nanochannel. By doing this and using the proper diameter of the nanowire in comparison with the nanochannel a nanowire based nanopore can be developed which enables the users to control the nanopore dimension by changing the nanogap size. Similar to the device developed here, two independent electric channels are used to detect the translocation of the molecules passing the first and second nanowire based nanopore.

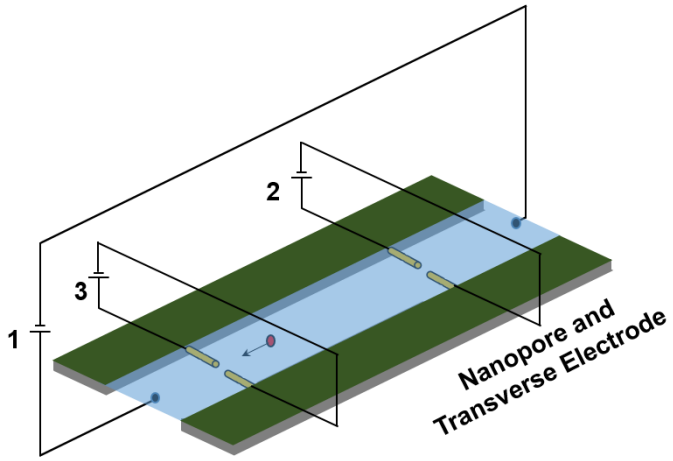

Figure 11.1. Schematics of the double nanowire based nanopore sensor with transverse electrode.

Figure 10.1 shows the schematics of the "double nanowire based nanopore sensor". The fabrication process of this device is very similar to the on introduced in the chapter 9 except for placing two nanowires on a nanochannel without nanopores. The main challenge to fabricate this device comparing to the one developed here is inserting the nanogap into the nanowire. From the methods introduced in the chapter 2, using chemical etching of the multi-segment nanowire at the location of the nanochannel is the most applicable technique for the fabrication of this device.

11.2. Using multichannel patch clamps

Nanoelectrode based sensors including nanochannel-nanopores with transverse nanoelectrode and nanowire based nanopores provide the ability to drive the molecule to the nanopores while measuring the translocation events from multiple electrical circuits. Thus, high precision patch clamps with multiple electrical channel are required to independently connect to the electrical circuits of the nanoelectrode based nanopores. The challenge of using such patch clamps is the synchronization between two or more channels in real time while measuring the events from different nanopores. This is the necessary task to correlate the translocation events recorded from different channels at the same time.

References

1. Akeson, M., et al., *Characterization of individual polymer molecules based on monomer-interface interactions*. 2007, Google Patents.

2. Rosenstein, J.K., et al., *Integrated nanopore sensing platform with sub-microsecond temporal resolution.* Nature methods, 2012. **9**(5): p. 487-492.

3. Nelson, T., B. Zhang, and O.V. Prezhdo, *Detection of nucleic acids with graphene nanopores: ab initio characterization of a novel sequencing device.* Nano letters, 2010. **10**(9): p. 3237-3242.

4. Branton, D., et al., *The potential and challenges of nanopore sequencing.* Nature biotechnology, 2008. **26**(10): p. 1146-1153.

5. Clarke, J., et al., *Continuous base identification for single-molecule nanopore DNA sequencing.* Nature nanotechnology, 2009. **4**(4): p. 265-270.

6. Ayub, M., et al., *Nanopore-based identification of individual nucleotides for direct RNA sequencing.* Nano letters, 2013. **13**(12): p. 6144-6150.

7. Nivala, J., D.B. Marks, and M. Akeson, *Unfoldase-mediated protein translocation through an [alpha]-hemolysin nanopore.* Nature biotechnology, 2013. **31**(3): p. 247-250.

8. Rodriguez-Larrea, D. and H. Bayley, *Multistep protein unfolding during nanopore translocation.* Nature nanotechnology, 2013. **8**(4): p. 288-295.

9. Ivankin, A., et al., *Label-free optical detection of biomolecular translocation through nanopore arrays.* ACS nano, 2014. **8**(10): p. 10774-10781.

10. Arnaut, V., M. Langecker, and F.C. Simmel, *Nanopore Force Spectroscopy of Aptamer–Ligand Complexes.* Biophysical journal, 2013. **105**(5): p. 1199-1207.

11. Taleat, Z., et al., *Detection strategies for methylated and hypermethylated DNA.* TrAC Trends in Analytical Chemistry, 2015. **66**: p. 80-89.

12. Japrung, D., et al., *Single-molecule studies of intrinsically disordered proteins using solid-state nanopores.* Analytical chemistry, 2013. **85**(4): p. 2449-2456.

13. Steinbock, L. and A. Radenovic, *The emergence of nanopores in next-generation sequencing.* Nanotechnology, 2015. **26**(7): p. 074003.

14. Stoloff, D.H. and M. Wanunu, *Recent trends in nanopores for biotechnology.* Current opinion in biotechnology, 2013. **24**(4): p. 699-704.

15. Yusko, E.C., et al., *Controlling protein translocation through nanopores with bio-inspired fluid walls.* Nature nanotechnology, 2011. **6**(4): p. 253.

16. Liu, K., et al., *Atomically thin molybdenum disulfide nanopores with high sensitivity for DNA translocation.* ACS nano, 2014. **8**(3): p. 2504-2511.

17. Zwolak, M. and M. Di Ventra, *Colloquium: Physical approaches to DNA sequencing and detection.* Reviews of Modern Physics, 2008. **80**(1): p. 141.

18. Dekker, C., *Solid-state nanopores.* Nature nanotechnology, 2007. **2**(4): p. 209-215.

19. Tsutsui, M., et al., *Single-molecule sensing electrode embedded in-plane nanopore.* Scientific reports, 2011. **1**.

20. Tsutsui, M., et al., *Single-molecule sensing electrode embedded in-plane nanopore.* Scientific reports, 2011. **1**: p. 46.

21. Lagerqvist, J., M. Zwolak, and M. Di Ventra, *Fast DNA sequencing via transverse electronic transport.* Nano letters, 2006. **6**(4): p. 779-782.

22. Kawaguchi, C., et al., *Electrical detection of single pollen allergen particles using electrode-embedded microchannels.* Journal of Physics: Condensed Matter, 2012. **24**(16): p. 164202.

23. Yokota, K., M. Tsutsui, and M. Taniguchi, *Electrode-embedded nanopores for label-free single-molecule sequencing by electric currents.* RSC Advances, 2014. **4**(31): p. 15886-15899.

24. Langecker, M., et al., *Electrophoretic time-of-flight measurements of single DNA molecules with two stacked nanopores.* Nano letters, 2011. **11**(11): p. 5002-5007.

25. Fanzio, P., et al., *DNA detection with a polymeric nanochannel device.* Lab on a Chip, 2011. **11**(17): p. 2961-2966.

26. Harms, Z.D., et al., *Nanofluidic devices with two pores in series for resistive-pulse sensing of single virus capsids.* Analytical chemistry, 2011. **83**(24): p. 9573-9578.

27. Ivanov, A.P., et al., *DNA tunneling detector embedded in a nanopore.* Nano letters, 2010. **11**(1): p. 279-285.

28. Barako, M.T., et al., *Thermal conduction in vertically aligned copper nanowire arrays and composites.* ACS applied materials & interfaces, 2015. **7**(34): p. 19251-19259.

29. Kang, S., et al., *Capillary printing of highly aligned silver nanowire transparent electrodes for high-performance optoelectronic devices.* Nano letters, 2015. **15**(12): p. 7933-7942.

30. Moutet, P., et al., *Directed Assembly of Single Colloidal Gold Nanowires by AFM Nanoxerography.* Langmuir, 2015. **31**(14): p. 4106-4112.

31. Merkoçi, A., *Nanoparticles-based strategies for DNA, protein and cell sensors.* Biosensors and Bioelectronics, 2010. **26**(4): p. 1164-1177.

32. Van Der Pol, E., et al., *Optical and non-optical methods for detection and characterization of microparticles and exosomes.* Journal of Thrombosis and Haemostasis, 2010. **8**(12): p. 2596-2607.

33. Wang, J., *Nanoparticle-based electrochemical DNA detection.* Analytica Chimica Acta, 2003. **500**(1): p. 247-257.

34. Gupta, P.K., *Single-molecule DNA sequencing technologies for future genomics research.* Trends in biotechnology, 2008. **26**(11): p. 602-611.

35. Bisht, S.S. and A.K. Panda, *DNA Sequencing: Methods and Applications*, in *Advances in Biotechnology*. 2014, Springer. p. 11-23.

36. Shokralla, S., et al., *Next-generation sequencing technologies for environmental DNA research.* Molecular ecology, 2012. **21**(8): p. 1794-1805.

37. Loman, N.J., et al., *High-throughput bacterial genome sequencing: an embarrassment of choice, a world of opportunity.* Nature Reviews Microbiology, 2012. **10**(9): p. 599-606.

38. Metzker, M.L., *Emerging technologies in DNA sequencing.* Genome research, 2005. **15**(12): p. 1767-1776.

39. Venter, J.C., *Multiple personal genomes await.* Nature, 2010. **464**(7289): p. 676-677.

40. Aksyonov, S.A., et al., *Multiplexed DNA sequencing-by-synthesis.* Analytical biochemistry, 2006. **348**(1): p. 127-138.

41. Venkatesan, B.M. and R. Bashir, *Nanopore sensors for nucleic acid analysis.* Nature nanotechnology, 2011. **6**(10): p. 615-624.

42. Scheicher, R.H., A. Grigoriev, and R. Ahuja, *DNA sequencing with nanopores from an ab initio perspective.* Journal of Materials Science, 2012. **47**(21): p. 7439-7446.

43. Tang, Z., et al., *Fabrications, Applications and Challenges of Solid-state Nanopores: A Mini Review.* 2016.

44. Li, J., D. Yu, and Q. Zhao, *Solid-state nanopore-based DNA single molecule detection and sequencing.* Microchimica Acta, 2015: p. 1-13.

45. Jiang, Y. and W. Guo, *Nanopore-based sensing and analysis: beyond the resistive-pulse method.* Science Bulletin, 2015. **60**(5): p. 491-502.

46. Kowalczyk, S.W., T.R. Blosser, and C. Dekker, *Biomimetic nanopores: learning from and about nature.* Trends in biotechnology, 2011. **29**(12): p. 607-614.

47. Feng, Y., et al., *Nanopore-based fourth-generation DNA sequencing technology.* Genomics, proteomics & bioinformatics, 2015. **13**(1): p. 4-16.

48. Astier, Y., O. Braha, and H. Bayley, *Toward single molecule DNA sequencing: direct identification of ribonucleoside and deoxyribonucleoside 5'-monophosphates by using an engineered protein nanopore equipped with a molecular adapter.* Journal of the American Chemical Society, 2006. **128**(5): p. 1705-1710.

49. Carminati, M., et al., *Design and characterization of a current sensing platform for silicon-based nanopores with integrated tunneling nanoelectrodes.* Analog Integrated Circuits and Signal Processing, 2013. **77**(3): p. 333-343.

50. Benner, S., et al., *Sequence-specific detection of individual DNA polymerase complexes in real time using a nanopore.* Nature nanotechnology, 2007. **2**(11): p. 718-724.

51. Cockroft, S.L., et al., *A single-molecule nanopore device detects DNA polymerase activity with single-nucleotide resolution.* Journal of the American Chemical Society, 2008. **130**(3): p. 818-820.

52. Lieberman, K.R., et al., *Processive replication of single DNA molecules in a nanopore catalyzed by phi29 DNA polymerase.* Journal of the American Chemical Society, 2010. **132**(50): p. 17961-17972.

53. Olasagasti, F., et al., *Replication of individual DNA molecules under electronic control using a protein nanopore.* Nature nanotechnology, 2010. **5**(11): p. 798-806.

54. Rincon-Restrepo, M., et al., *Controlled translocation of individual DNA molecules through protein nanopores with engineered molecular brakes.* Nano letters, 2011. **11**(2): p. 746-750.

55. Deamer, D., *Nanopore analysis of nucleic acids bound to exonucleases and polymerases.* Annual review of biophysics, 2010. **39**: p. 79-90.

56. Postma, H.W.C., *Rapid sequencing of individual DNA molecules in graphene nanogaps.* Nano letters, 2010. **10**(2): p. 420-425.

57. Healy, K., et al., *Fabrication and characterization of nanopores with insulated transverse nanoelectrodes for DNA sensing in salt solution.* Electrophoresis, 2012. **33**(23): p. 3488-3496.

58. Ohshiro, T. and Y. Umezawa, *Complementary base-pair-facilitated electron tunneling for electrically pinpointing complementary nucleobases.* Proceedings of the National Academy of Sciences of the United States of America, 2006. **103**(1): p. 10-14.

59. Lagerqvist, J., M. Zwolak, and M. Di Ventra, *Influence of the environment and probes on rapid DNA sequencing via transverse electronic transport.* Biophysical journal, 2007. **93**(7): p. 2384-2390.

60. Pedone, D., et al., *Fabrication and electrical characterization of a pore–cavity–pore device.* Journal of Physics: Condensed Matter, 2010. **22**(45): p. 454115.

61. Pedone, D., et al., *A Pore− Cavity− Pore Device to Trap and Investigate Single Nanoparticles and DNA Molecules in a Femtoliter Compartment: Confined Diffusion and Narrow Escape.* Nano letters, 2011. **11**(4): p. 1561-1567.

62. Haque, F., et al., *Solid-state and biological nanopore for real-time sensing of single chemical and sequencing of DNA.* Nano Today, 2013. **8**(1): p. 56-74.

63. de la Escosura-Muñiz, A. and A. Merkoçi, *Nanochannels for electrical biosensing.* TrAC Trends in Analytical Chemistry, 2016. **79**: p. 134-150.

64. Storm, A., et al., *Fabrication of solid-state nanopores with single-nanometre precision.* Nature materials, 2003. **2**(8): p. 537-540.

65. Guo, L.J., X. Cheng, and C.-F. Chou, *Fabrication of size-controllable nanofluidic channels by nanoimprinting and its application for DNA stretching.* Nano letters, 2004. **4**(1): p. 69-73.

66. Fanget, A., et al., *Nanopore integrated nanogaps for DNA detection.* Nano letters, 2013. **14**(1): p. 244-249.

67. Amirsadeghi, A., *Developing Defect-tolerant Demolding Process in Nanoimprint Lithography*. 2013, University of Tehran.

68. Björk, M., et al., *Silicon nanowire tunneling field-effect transistors.* Applied Physics Letters, 2008. **92**(19): p. 3504.

69. Sun, Y., et al., *Uniform silver nanowires synthesis by reducing AgNO3 with ethylene glycol in the presence of seeds and poly (vinyl pyrrolidone).* Chemistry of Materials, 2002. **14**(11): p. 4736-4745.

70. Deng, S., et al., *Reduced graphene oxide conjugated Cu2O nanowire mesocrystals for high-performance NO2 gas sensor.* Journal of the American Chemical Society, 2012. **134**(10): p. 4905-4917.

71. Lee, E.P., et al., *Growing Pt nanowires as a densely packed array on metal gauze.* Journal of the American chemical Society, 2007. **129**(35): p. 10634-10635.

72. Boughey, F.L., et al., *Vertically aligned zinc oxide nanowires electrodeposited within porous polycarbonate templates for vibrational energy harvesting.* Nanotechnology, 2016. **27**(28): p. 28LT02.

73. Gui, Z., et al., *Co-electrodeposition of RuO 2–MnO 2 nanowires and the contribution of RuO 2 to the capacitance increase.* Physical Chemistry Chemical Physics, 2015. **17**(23): p. 15173-15180.

74. Yalçın, O., et al., *A comparison of the magnetic properties of Ni and Co nanowires deposited in different templates and on different substrates.* Journal of Magnetism and Magnetic Materials, 2015. **373**: p. 207-212.

75. Long, Y.-Z., et al., *Recent advances in large-scale assembly of semiconducting inorganic nanowires and nanofibers for electronics, sensors and photovoltaics.* Chemical Society Reviews, 2012. **41**(12): p. 4560-4580.

76. Sarkar, J., G.G. Khan, and A. Basumallick, *Nanowires: properties, applications and synthesis via porous anodic aluminium oxide template.* Bulletin of Materials Science, 2007. **30**(3): p. 271-290.

77. Hu, L., et al., *Scalable coating and properties of transparent, flexible, silver nanowire electrodes.* ACS nano, 2010. **4**(5): p. 2955-2963.

78. Wu, H., et al., *Electrospun metal nanofiber webs as high-performance transparent electrode.* Nano letters, 2010. **10**(10): p. 4242-4248.

79. Xia, X., et al., *High-quality metal oxide core/shell nanowire arrays on conductive substrates for electrochemical energy storage.* ACS nano, 2012. **6**(6): p. 5531-5538.

80. Koenigsmann, C., et al., *Enhanced electrocatalytic performance of processed, ultrathin, supported Pd–Pt core–shell nanowire catalysts for the oxygen reduction reaction.* Journal of the American Chemical Society, 2011. **133**(25): p. 9783-9795.

81. Zhang, G., W. Wang, and X. Li, *Enhanced thermoelectric properties of core/shell heterostructure nanowire composites.* Advanced Materials, 2008. **20**(19): p. 3654-3656.

82. Gajbhiye, N. and S. Bhattacharyya, *Magnetic properties of ε-Fe3N–GaN core–shell nanowires.* Nanotechnology, 2005. **16**(10): p. 2012.

83. Kim, H.W., et al., *Fabrication and magnetic properties of In 2 O 3/NiMnGa core–shell nanowires.* Thin Solid Films, 2013. **546**: p. 219-225.

84. Ma, J., K. Wang, and M. Zhan, *Growth mechanism and electrical and magnetic properties of Ag–Fe3O4 core–shell nanowires.* ACS applied materials & interfaces, 2015. **7**(29): p. 16027-16039.

85. Huang, Y., et al., *Directed assembly of one-dimensional nanostructures into functional networks.* Science, 2001. **291**(5504): p. 630-633.

86. McAlpine, M.C., et al., *High-performance nanowire electronics and photonics on glass and plastic substrates.* Nano Letters, 2003. **3**(11): p. 1531-1535.

87. McAlpine, M.C., R.S. Friedman, and C.M. Lieber, *Nanoimprint lithography for hybrid plastic electronics.* Nano Letters, 2003. **3**(4): p. 443-445.

88. Duan, X., et al., *High-performance thin-film transistors using semiconductor nanowires and nanoribbons.* Nature, 2003. **425**(6955): p. 274-278.

89. Hangarter, C.M. and N.V. Myung, *Magnetic alignment of nanowires.* Chemistry of materials, 2005. **17**(6): p. 1320-1324.

90. Liu, M., et al., *Self-assembled magnetic nanowire arrays.* Applied Physics Letters, 2007. **90**(10): p. 103105.

91. Rheem, Y., et al., *Site-specific magnetic assembly of nanowires for sensor arrays fabrication.* Nanotechnology, IEEE Transactions on, 2008. **7**(3): p. 251-255.

92. Bartenwerfer, M. and S. Fatikow. *Robotic nanowire handling for prototypic NEMS devices*. in *Robotics and Automation (ICRA), 2013 IEEE International Conference on*. 2013. IEEE.

93. Ropp, C., et al., *Manipulating quantum dots to nanometer precision by control of flow.* Nano letters, 2010. **10**(7): p. 2525-2530.

94. Probst, R., et al., *Flow control of small objects on chip: manipulating live cells, quantum dots, and nanowires.* Control Systems, IEEE, 2012. **32**(2): p. 26-53.

95. Mathai, P.P., et al., *Simultaneous positioning and orientation of single nano-wires using flow control.* RSC Advances, 2013. **3**(8): p. 2677-2682.

96. Donolato, M., et al., *On-Chip Manipulation of Protein-Coated Magnetic Beads via Domain-Wall Conduits.* Advanced materials, 2010. **22**(24): p. 2706-2710.

97. Ooi, C. and B.B. Yellen, *Field gradients can control the alignment of nanorods.* Langmuir, 2008. **24**(16): p. 8514-8521.

98. Hangarter, C.M., et al., *Hierarchical magnetic assembly of nanowires.* Nanotechnology, 2007. **18**(20): p. 205305.

99. Yoo, B., et al., *Magnetically assembled 30 nm diameter nickel nanowire with ferromagnetic electrodes.* Nanotechnology, 2006. **17**(10): p. 2512.

100. Kim, Y.-H., et al., *Advanced Methodologies for Manipulating Nanoscale Features in Focused Ion Beam.* Applied Microscopy, 2015. **45**(4): p. 208-213.

101. Ye, X., et al., *Automated pick-place of silicon nanowires.* Automation Science and Engineering, IEEE Transactions on, 2013. **10**(3): p. 554-561.

102. Bartenwerfer, M. and S. Fatikow. *Robotic dual-tip assembly for nanowire handling and integration*. in *Nanotechnology (IEEE-NANO), 2015 IEEE 15th International Conference on*. 2015. IEEE.

103. Zhou, C., et al. *Closed-loop controlled nanoprobing inside SEM*. in *Nanotechnology (IEEE-NANO), 2014 IEEE 14th International Conference on*. 2014. IEEE.

104. Li, D., et al., *SEM Image-Based 3-D Nanomanipulation Information Extraction and Closed-Loop Probe Control.* Nanotechnology, IEEE Transactions on, 2014. **13**(6): p. 1194-1203.

105. Cagliani, A., et al., *Manipulation and in situ transmission electron microscope characterization of sub-100 nm nanostructures using a microfabricated nanogripper.* Journal of Micromechanics and Microengineering, 2010. **20**(3): p. 035009.

106. Carlson, K., et al., *A carbon nanofibre scanning probe assembled using an electrothermal microgripper.* Nanotechnology, 2007. **18**(34): p. 345501.

107. Nagase, T., T. Kubota, and S. Mashiko, *Fabrication of nano-gap electrodes for measuring electrical properties of organic molecules using a focused ion beam.* Thin Solid Films, 2003. **438**: p. 374-377.

108. Djukic, D. and J. Van Ruitenbeek, *Shot noise measurements on a single molecule.* Nano letters, 2006. **6**(4): p. 789-793.

109. Lörtscher, E., et al., *Reversible and Controllable Switching of a Single-Molecule Junction.* Small, 2006. **2**(8-9): p. 973-977.

110. Nagase, T., et al., *Maskless fabrication of nanoelectrode structures with nanogaps by using Ga focused ion beams.* Microelectronic engineering, 2005. **78**: p. 253-259.

111. Nagase, T., et al., *Direct fabrication of nano-gap electrodes by focused ion beam etching.* Thin Solid Films, 2006. **499**(1): p. 279-284.

112. Banholzer, M.J., et al., *Rationally designed nanostructures for surface-enhanced Raman spectroscopy.* Chemical Society Reviews, 2008. **37**(5): p. 885-897.

113. Blom, T., et al., *Fabrication and characterization of highly reproducible, high resistance nanogaps made by focused ion beam milling.* Nanotechnology, 2007. **18**(28): p. 285301.

114. Qin, L., et al., *On-wire lithography.* Science, 2005. **309**(5731): p. 113-115.

115. Chen, X., et al., *Chemical fabrication of heterometallic nanogaps for molecular transport junctions.* Nano letters, 2009. **9**(12): p. 3974-3979.

116. Huang, X.J., A.M. O'Mahony, and R.G. Compton, *Microelectrode arrays for electrochemistry: Approaches to fabrication.* Small, 2009. **5**(7): p. 776-788.

117. Bergonzo, P., et al., *3D shaped mechanically flexible diamond microelectrode arrays for eye implant applications: The MEDINAS project.* Irbm, 2011. **32**(2): p. 91-94.

118. Johnstone, A.F., et al., *Microelectrode arrays: a physiologically based neurotoxicity testing platform for the 21st century.* Neurotoxicology, 2010. **31**(4): p. 331-350.

119. Qin, D., Y. Xia, and G.M. Whitesides, *Soft lithography for micro-and nanoscale patterning.* Nature protocols, 2010. **5**(3): p. 491-502.

120. Lin, Y., et al., *Carbon-ring microelectrode arrays for electrochemical imaging of single cell exocytosis: fabrication and characterization.* Analytical chemistry, 2012. **84**(6): p. 2949-2954.

121. Fuchsberger, K., et al., *Multiwalled Carbon-Nanotube-Functionalized Microelectrode Arrays Fabricated by Microcontact Printing: Platform for Studying Chemical and Electrical Neuronal Signaling.* Small, 2011. **7**(4): p. 524-530.

122. Ordeig, O., et al., *On-chip electric field driven electrochemical detection using a poly (dimethylsiloxane) microchannel with gold microband electrodes.* Analytical chemistry, 2008. **80**(10): p. 3622-3632.

123. Baaken, G., et al., *Planar microelectrode-cavity array for high-resolution and parallel electrical recording of membrane ionic currents.* Lab on a Chip, 2008. **8**(6): p. 938-944.

124. Hu, X., et al., *Fabrication of gold microelectrodes on polystyrene sheets by UV-directed electroless plating and its application in electrochemical detection.* Journal of Electroanalytical Chemistry, 2010. **638**(1): p. 21-27.

125. Kong, Y., et al., *Fabrication of a gold microelectrode for amperometric detection on a polycarbonate electrophoresis chip by photodirected electroless plating.* Electrophoresis, 2006. **27**(14): p. 2940-2950.

126. Qian, S. and Y. Ai, *Electrokinetic particle transport in micro-/nanofluidics: direct numerical simulation analysis*. Vol. 153. 2012: CRC Press.

127. Daiguji, H., P. Yang, and A. Majumdar, *Ion transport in nanofluidic channels.* Nano Letters, 2004. **4**(1): p. 137-142.

128. Xue, S., N. Hu, and S. Qian, *Tuning surface charge property by floating gate field effect transistor.* Journal of colloid and interface science, 2012. **365**(1): p. 326-328.

129. Masliyah, J.H. and S. Bhattacharjee, *Electrokinetic and colloid transport phenomena*. 2006: John Wiley & Sons.

130. Tohver, V., et al., *Nanoparticle halos: A new colloid stabilization mechanism.* Proceedings of the National Academy of Sciences, 2001. **98**(16): p. 8950-8954.

131. Karnik, R., et al., *Electrostatic control of ions and molecules in nanofluidic transistors.* Nano letters, 2005. **5**(5): p. 943-948.

132. Qian, S. and H.H. Bau, *Theoretical investigation of electro-osmotic flows and chaotic stirring in rectangular cavities.* Applied mathematical modelling, 2005. **29**(8): p. 726-753.

133. Qian, S. and H.H. Bau, *A chaotic electroosmotic stirrer.* Analytical Chemistry, 2002. **74**(15): p. 3616-3625.

134. Lee, G.B., et al., *Dispersion control in microfluidic chips by localized zeta potential variation using the field effect.* Electrophoresis, 2004. **25**(12): p. 1879-1887.

135. Sniadecki, N.J., et al., *Induced pressure pumping in polymer microchannels via field-effect flow control.* Analytical chemistry, 2004. **76**(7): p. 1942-1947.

136. Hu, N., Y. Ai, and S. Qian, *Field effect control of electrokinetic transport in micro/nanofluidics.* Sensors and Actuators B: Chemical, 2012. **161**(1): p. 1150-1167.

137. Ai, Y., et al., *Field effect regulation of DNA translocation through a nanopore.* Analytical chemistry, 2010. **82**(19): p. 8217-8225.

138. German, S.R., et al., *Controlling nanoparticle dynamics in conical nanopores.* The Journal of Physical Chemistry C, 2012. **117**(1): p. 703-711.

139. Qian, S., et al., *Effect of linear surface-charge non-uniformities on the electrokinetic ionic-current rectification in conical nanopores.* Journal of colloid and interface science, 2009. **329**(2): p. 376-383.

140. Liu, Q., et al., *Asymmetric properties of ion transport in a charged conical nanopore.* Physical Review E, 2007. **75**(5): p. 051201.

141. Lan, W.-J., et al., *Effect of surface charge on the resistive pulse waveshape during particle translocation through glass nanopores.* The Journal of Physical Chemistry C, 2014. **118**(5): p. 2726-2734.

142. Qian, S., et al., *Electrophoretic motion of a spherical particle with a symmetric nonuniform surface charge distribution in a nanotube.* Langmuir, 2008. **24**(10): p. 5332-5340.

143. Dorfman, K.D., *DNA electrophoresis in microfabricated devices.* Reviews of Modern Physics, 2010. **82**(4): p. 2903.

144. Esfandiari, L., et al., *Sequence-specific DNA detection at 10 fM by electromechanical signal transduction.* Analytical chemistry, 2014. **86**(19): p. 9638-9643.

145. Grieshaber, D., et al., *Electrochemical biosensors-sensor principles and architectures.* Sensors, 2008. **8**(3): p. 1400-1458.

146. Sandler, J., et al., *Development of a dispersion process for carbon nanotubes in an epoxy matrix and the resulting electrical properties.* Polymer, 1999. **40**(21): p. 5967-5971.

147. Filas, R.W., et al., *Article comprising aligned nanowires*. 2004, Google Patents.

148. Colli, A., et al., *Thermal and chemical vapor deposition of Si nanowires: Shape control, dispersion, and electrical properties.* Journal of Applied Physics, 2007. **102**(3): p. 034302.

149. Biggs, S. and P. Mulvaney, *Surfactant and polymer adsorption: Atomic Force Microscopy measurements.* Surfactant Adsorption and Surface Solubilization, 1995. **615**: p. 255-266.

150. Tian, M., et al., *Stable high areal capacity lithium-ion battery anodes based on three-dimensional Ni–Sn nanowire networks.* Journal of Power Sources, 2012. **211**: p. 46-51.

151. Choi, C., et al., *Strongly superhydrophobic silicon nanowires by supercritical CO2 drying.* Electronic Materials Letters, 2010. **6**(2): p. 59-64.

152. Fan, H.J., P. Werner, and M. Zacharias, *Semiconductor nanowires: from self-organization to patterned growth.* small, 2006. **2**(6): p. 700-717.

153. Reisner, W., J.N. Pedersen, and R.H. Austin, *DNA confinement in nanochannels: physics and biological applications.* Reports on Progress in Physics, 2012. **75**(10): p. 106601.

154. Guo, Y., et al., *Real-time biomolecular binding detection using a sensitive photonic crystal biosensor.* Analytical chemistry, 2010. **82**(12): p. 5211-5218.

155. Reich, D., et al., *Biological applications of multifunctional magnetic nanowires.* Journal of Applied Physics, 2003. **93**(10): p. 7275-7280.

156. Hultgren, A., et al., *Cell manipulation using magnetic nanowires.* Journal of Applied Physics, 2003. **93**(10): p. 7554-7556.

157. Marson, R.L., et al., *Nickel nanowires for planer microwave circuit applications and characterization.* Journal of Vacuum Science & Technology B: Microelectronics and

Nanometer Structures Processing, Measurement, and Phenomena, 2007. **25**(6): p. 2619-2623.

158. Gray, B.L., *A review of magnetic composite polymers applied to microfluidic devices.* Journal of The Electrochemical Society, 2014. **161**(2): p. B3173-B3183.

159. Gencoglu, A. and A.R. Minerick, *Electrochemical detection techniques in micro-and nanofluidic devices.* Microfluidics and nanofluidics, 2014. **17**(5): p. 781-807.

160. Sharma, M., et al., *New opportunities in microwave electronics with ferromagnetic nanowires.* Journal of Applied Physics, 2014. **115**(17): p. 17A518.

161. Van Kerckhoven, V., L. Piraux, and I. Huynen, *Substrate integrated waveguide isolator based on ferromagnetic nanowires in porous alumina template.* Applied Physics Letters, 2014. **105**(18): p. 183107.

162. Bauer, U., S. Emori, and G.S. Beach, *Voltage-controlled domain wall traps in ferromagnetic nanowires.* Nature nanotechnology, 2013. **8**(6): p. 411-416.

163. Spiegel, J. and I. Huynen. *Microwave properties of ferromagnetic nanowires and applications to tunable devices*. in *Solid State Phenomena*. 2009. Trans Tech Publ.

164. Ji, J., et al., *One-Dimensional Nano-Interconnection Formation.* Small, 2013. **9**(18): p. 3014-3029.

165. Zhang, C., et al., *Facile One-Step Growth and Patterning of Aligned Squaraine Nanowires via Evaporation-Induced Self-Assembly.* Advanced Materials, 2008. **20**(9): p. 1716-1720.

166. Huang, J., et al., *One-Step Patterning of Aligned Nanowire Arrays by Programmed Dip Coating.* Angewandte Chemie International Edition, 2007. **46**(14): p. 2414-2417.

167. Bao, R., et al., *Large-Scale Controllable Patterning Growth of Aligned Organic Nanowires through Evaporation-Induced Self-Assembly.* Chemistry-A European Journal, 2012. **18**(3): p. 975-980.

168. Talapin, D.V., et al., *Alignment, electronic properties, doping, and on-chip growth of colloidal PbSe nanowires.* The Journal of Physical Chemistry C, 2007. **111**(35): p. 13244-13249.

169. Dai, H., et al., *Ordering Ag nanowire arrays by spontaneous spreading of volatile droplet on solid surface.* Scientific reports, 2014. **4**: p. 6742.

170. Cheng, W. and M. Niederberger, *Evaporation-Induced Self-Assembly of Ultrathin Tungsten Oxide Nanowires over a Large Scale for Ultraviolet Photodetector.* Langmuir, 2016. **32**(10): p. 2474-2481.

171. Bao, R.-R., et al., *Self-assembly and hierarchical patterning of aligned organic nanowire arrays by solvent evaporation on substrates with patterned wettability.* ACS applied materials & interfaces, 2013. **5**(12): p. 5757-5762.

172. Jeon, Y.J., et al., *Pattern analysis of aligned nanowires in a microchannel.* Measurement Science and Technology, 2013. **24**(3): p. 035303.

173. Yang, B.-R., et al., *Microchannel wetting for controllable patterning and alignment of silver nanowire with high resolution.* ACS applied materials & interfaces, 2015. **7**(38): p. 21433-21441.

174. Lim, J.K., et al., *Alignment strategies for the assembly of nanowires with submicron diameters.* Small, 2010. **6**(16): p. 1736-1740.

175. Yan, Z., et al., *Three-dimensional optical trapping and manipulation of single silver nanowires.* Nano letters, 2012. **12**(10): p. 5155-5161.

176. Pauzauskie, P.J., et al., *Optical trapping and integration of semiconductor nanowire assemblies in water.* Nature materials, 2006. **5**(2): p. 97-101.

177. Agarwal, R., et al., *Manipulation and assembly of nanowires with holographic optical traps.* Optics Express, 2005. **13**(22): p. 8906-8912.

178. Zhou, R., et al., *CdSe nanowires with illumination-enhanced conductivity: Induced dipoles, dielectrophoretic assembly, and field-sensitive emission.* Journal of applied physics, 2007. **101**(7): p. 073704.

179. Wang, M.C., et al., *Electrokinetic assembly of selenium and silver nanowires into macroscopic fibers.* ACS nano, 2010. **4**(5): p. 2607-2614.

180. Venkatesh, R., et al., *Directed Assembly of Ultrathin Gold Nanowires over Large Area by Dielectrophoresis.* Langmuir, 2015. **31**(33): p. 9246-9252.

181. Ahmed, W., et al., *Quantitative analysis of gold nanorod alignment after electric field-assisted deposition.* Nano letters, 2009. **9**(11): p. 3786-3794.

182. Smith, P.A., et al., *Electric-field assisted assembly and alignment of metallic nanowires.* Applied Physics Letters, 2000. **77**(9): p. 1399-1401.

183. Li, N., et al., *Preparation of aligned Fe 3 O 4@ Ag-nanowire/poly (vinyl alcohol) nanocomposite films via a low magnetic field.* Composites Part A: Applied Science and Manufacturing, 2015. **77**: p. 87-95.

184. Salem, A.K., et al., *Receptor-Mediated Self-Assembly of Multi-Component Magnetic Nanowires.* Advanced Materials, 2004. **16**(3): p. 268-271.

185. Myung, S., et al., *Large-Scale "Surface-Programmed Assembly" of Pristine Vanadium Oxide Nanowire-Based Devices.* Advanced Materials, 2005. **17**(19): p. 2361-2364.

186. Kang, J., et al., *Massive assembly of ZnO nanowire-based integrated devices.* Nanotechnology, 2008. **19**(9): p. 095303.

187. Chen, M. and P.C. Searson, *The Dynamics of Nanowire Self-Assembly.* Advanced Materials, 2005. **17**(22): p. 2765-2768.

188. Gao, F., et al., *Patterning of self-assembled monolayers by phase-shifting mask and its applications in large-scale assembly of nanowires.* Applied Physics Letters, 2015. **106**(4): p. 041605.

189. Xiong, X., et al., *Building highly organized single-walled-carbon-nanotube networks using template-guided fluidic assembly.* Small, 2007. **3**(12): p. 2006-2010.

190. Bang, J., et al., *Assembly and Densification of Nanowire Arrays via Shrinkage.* Nano letters, 2014. **14**(6): p. 3304-3308.

191. Xu, F., et al., *Strain-release assembly of nanowires on stretchable substrates.* ACS nano, 2011. **5**(2): p. 1556-1563.

192. Deng, H., et al., *Growth, patterning and alignment of organolead iodide perovskite nanowires for optoelectronic devices.* Nanoscale, 2015. **7**(9): p. 4163-4170.

193. Dong, J., N.M. Abukhdeir, and I.A. Goldthorpe, *Simple assembly of long nanowires through substrate stretching.* Nanotechnology, 2015. **26**(48): p. 485302.

194. Freer, E.M., et al., *High-yield self-limiting single-nanowire assembly with dielectrophoresis.* Nature nanotechnology, 2010. **5**(7): p. 525-530.

195. Zhou, X., et al., *Capillary force-driven, large-area alignment of multi-segmented nanowires.* ACS nano, 2014. **8**(2): p. 1511-1516.

196. Liu, J.-W., H.-W. Liang, and S.-H. Yu, *Macroscopic-scale assembled nanowire thin films and their functionalities.* Chemical reviews, 2012. **112**(8): p. 4770-4799.

197. Wang, M.C. and B.D. Gates, *Directed assembly of nanowires.* Materials today, 2009. **12**(5): p. 34-43.

198. Yuan, J., Y. Xu, and A.H. Müller, *One-dimensional magnetic inorganic–organic hybrid nanomaterials.* Chemical Society Reviews, 2011. **40**(2): p. 640-655.

199. Zhang, S.-Y., M.D. Regulacio, and M.-Y. Han, *Self-assembly of colloidal one-dimensional nanocrystals.* Chemical Society Reviews, 2014. **43**(7): p. 2301-2323.

200. Su, B., Y. Wu, and L. Jiang, *The art of aligning one-dimensional (1D) nanostructures.* Chemical Society Reviews, 2012. **41**(23): p. 7832-7856.

201. Rao, C., et al., *Inorganic nanowires.* Progress in Solid State Chemistry, 2003. **31**(1): p. 5-147.

202. Geng, X., W. Liang, and E.J. Podlaha, *Editors' Choice—A Methodology to Electrochemically Fabricate Fe-Ni-Co Nanotips.* Journal of The Electrochemical Society, 2017. **164**(4): p. D218-D224.

203. Beheshti, M., et al. *Reduction of nanowire agglomeration via an intermediate membrane in nanowires preparation for nanosensors application*. in *ASME 2015 International Mechanical Engineering Congress and Exposition*. 2015. American Society of Mechanical Engineers.

204. Pourbaix, M., *Atlas of electrochemical equilibria in aqueous solutions.* 1974.

205. Sun, L., K. Keshoju, and H. Xing, *Magnetic field mediated nanowire alignment in liquids for nanocomposite synthesis.* Nanotechnology, 2008. **19**(40): p. 405603.

206. Keshoju, K., H. Xing, and L. Sun, *Magnetic field driven nanowire rotation in suspension.* Applied Physics Letters, 2007. **91**(12): p. 123114.

207. Antsov, M., et al., *Analysis of static friction and elastic forces in a nanowire bent on a flat surface: a comparative study.* Tribology International, 2014. **72**: p. 31-34.

208. Soci, C., et al., *ZnO nanowire UV photodetectors with high internal gain.* Nano letters, 2007. **7**(4): p. 1003-1009.

209. Jie, J., et al., *Photoconductive characteristics of single-crystal CdS nanoribbons.* Nano letters, 2006. **6**(9): p. 1887-1892.

210. Fan, Z., et al., *Large-scale, heterogeneous integration of nanowire arrays for image sensor circuitry.* Proceedings of the National Academy of Sciences, 2008. **105**(32): p. 11066-11070.

211. Ford, A.C., et al., *Synthesis, contact printing, and device characterization of Ni-catalyzed, crystalline InAs nanowires.* Nano Research, 2008. **1**(1): p. 32-39.

212. Ford, A.C., et al., *Diameter-dependent electron mobility of InAs nanowires.* Nano Letters, 2008. **9**(1): p. 360-365.

213. Cheng, T., et al., *Stretchable Thin-Film Electrodes for Flexible Electronics with High Deformability and Stretchability.* Advanced Materials, 2015. **27**(22): p. 3349-3376.

214. Liu, J., et al., *A three-layer PMMA electrophoresis microchip with Pt microelectrodes insulated by a thin film for contactless conductivity detection.* Lab on a Chip, 2011. **11**(5): p. 969-973.

215. Brkljača, R., J.M. White, and S. Urban, *Phytochemical investigation of the constituents derived from the Australian plant Macropidia fuliginosa.* Journal of natural products, 2015. **78**(7): p. 1600-1608.

216. Vazquez-Mena, O., et al., *Resistless nanofabrication by stencil lithography: A review.* Microelectronic Engineering, 2015. **132**: p. 236-254.

217. Vazquez-Mena, O., et al., *Analysis of the blurring in stencil lithography.* Nanotechnology, 2009. **20**(41): p. 415303.

218. Sidler, K., et al., *Organic thin film transistors on flexible polyimide substrates fabricated by full-wafer stencil lithography.* Sensors and Actuators A: Physical, 2010. **162**(2): p. 155-159.

219. Du, K., et al., *Stencil lithography for scalable micro-and nanomanufacturing.* Micromachines, 2017. **8**(4): p. 131.

220. Sidler, K., et al., *Compliant membranes improve resolution in full-wafer micro/nanostencil lithography.* Nanoscale, 2012. **4**(3): p. 773-778.

221. Hwang, S.-W., et al., *A physically transient form of silicon electronics.* Science, 2012. **337**(6102): p. 1640-1644.

222. Liu, Y., et al. *3-D nanofabrication using nanostructured photoresist film as free-standing appliqué*. in *Micro Electro Mechanical Systems (MEMS), 2012 IEEE 25th International Conference on*. 2012. IEEE.

223. Park, J.Y., et al., *Study of cellular behaviors on concave and convex microstructures fabricated from elastic PDMS membranes.* Lab on a Chip, 2009. **9**(14): p. 2043-2049.

224. Shimizu, K., H. Fujita, and E. Nagamori, *Micropatterning of single myotubes on a thermoresponsive culture surface using elastic stencil membranes for single-cell analysis.* Journal of bioscience and bioengineering, 2010. **109**(2): p. 174-178.

225. Lee, D. and S. Yang, *On-Chip Parylene-C Microstencil for Simple-to-Use Patterning of Proteins and Cells on Polydimethylsiloxane.* ACS applied materials & interfaces, 2013. **5**(7): p. 2658-2668.

226. Ji, D., et al., *A novel method for photolithographic polymer shadow masking: toward high-resolution high-performance top-contact organic field effect transistors.* Chemical Communications, 2014. **50**(61): p. 8328-8330.

227. Yun, H., et al., *Stencil nano lithography based on a nanoscale polymer shadow mask: Towards organic nanoelectronics.* Scientific reports, 2015. **5**: p. 10220.

228. Ye, S., et al., *Metal nanowire networks: the next generation of transparent conductors.* Advanced Materials, 2014. **26**(39): p. 6670-6687.

229. Rojo, M.M., et al., *Review on measurement techniques of transport properties of nanowires.* Nanoscale, 2013. **5**(23): p. 11526-11544.

230. Allen, J.E., et al., *Nonuniform nanowire doping profiles revealed by quantitative scanning photocurrent microscopy.* Advanced Materials, 2009. **21**(30): p. 3067-3072.

231. Suzuki, H., et al., *Electrical conductivity measurement of silicon wire prepared by CVD.* Chemical Physics Letters, 2009. **468**(4): p. 211-215.

232. Elawayeb, M., et al., *Electrical properties of individual NiFe/Pt multilayer nanowires measured in situ in a scanning electron microscope.* Journal of Applied Physics, 2012. **111**(3): p. 034306.

233. Bernal, R.A., et al., *In Situ Electron Microscopy Four-Point Electromechanical Characterization of Freestanding Metallic and Semiconducting Nanowires.* small, 2014. **10**(4): p. 725-733.

234. Völklein, F., et al., *Microchips for the Investigation of Thermal and Electrical Properties of Individual Nanowires.* Journal of electronic materials, 2010. **39**(9): p. 1950-1956.

235. Zhou, J., et al., *Thermoelectric properties of individual electrodeposited bismuth telluride nanowires.* Applied Physics Letters, 2005. **87**(13): p. 133109.

236. Seol, J.H., et al., *Measurement and analysis of thermopower and electrical conductivity of an indium antimonide nanowire from a vapor-liquid-solid method.* Journal of applied physics, 2007. **101**(2): p. 023706.

237. Long, Y., et al., *Electrical conductivity studies on individual conjugated polymer nanowires: two-probe and four-probe results.* Nanoscale research letters, 2009. **5**(1): p. 237.

238. Cronin, S.B., et al., *Making electrical contacts to nanowires with a thick oxide coating.* Nanotechnology, 2002. **13**(5): p. 653.

239. Fan, Z., et al., *Structures and electrical properties of Ag-tetracyanoquinodimethane organometallic nanowires.* IEEE transactions on nanotechnology, 2005. **4**(2): p. 238-241.

240. Chang, M.T., et al., *Magnetic and Electrical Characterizations of Half-Metallic Fe3O4 Nanowires.* Advanced Materials, 2007. **19**(17): p. 2290-2294.

241. Schmitt, A.L., et al., *Metallic single-crystal CoSi nanowires via chemical vapor deposition of single-source precursor.* The Journal of Physical Chemistry B, 2006. **110**(37): p. 18142-18146.

242. Liang, W., et al., *Thermoelectric properties of p-type PbSe nanowires.* Nano Research, 2009. **2**(5): p. 394-399.

243. Lew, K.-K., et al., *Structural and electrical properties of trimethylboron-doped silicon nanowires.* Applied Physics Letters, 2004. **85**(15): p. 3101-3103.

244. Duan, X., et al., *Indium phosphide nanowires as building blocks for nanoscale electronic and optoelectronic devices.* Nature, 2001. **409**(6816): p. 66-69.

245. Shi, L., et al., *Measuring thermal and thermoelectric properties of one-dimensional nanostructures using a microfabricated device.* Journal of heat transfer, 2003. **125**(5): p. 881-888.

246. Hochbaum, A.I., et al., *Enhanced thermoelectric performance of rough silicon nanowires.* Nature, 2008. **451**(7175): p. 163-167.

247. www.mechonics.de. *Miniature XYZ positioners with piezo electric inertial drive*. 2014.

248. Kunnari, E., et al., *Environmental evaluation of new technology: printed electronics case study.* Journal of Cleaner Production, 2009. **17**(9): p. 791-799.

249. Hu, L., H. Wu, and Y. Cui, *Metal nanogrids, nanowires, and nanofibers for transparent electrodes.* MRS bulletin, 2011. **36**(10): p. 760-765.

250. Silver, A.F.M., et al., *MINERAL COMMODITY SUMMARIES 2013.*

251. Na, S.I., et al., *Efficient and Flexible ITO-Free Organic Solar Cells Using Highly Conductive Polymer Anodes.* Advanced Materials, 2008. **20**(21): p. 4061-4067.

252. Hecht, D.S., et al., *High conductivity transparent carbon nanotube films deposited from superacid.* Nanotechnology, 2011. **22**(7): p. 075201.

253. Bae, S., et al., *Roll-to-roll production of 30-inch graphene films for transparent electrodes.* Nature nanotechnology, 2010. **5**(8): p. 574-578.

254. Ye, S., et al., *A rapid synthesis of high aspect ratio copper nanowires for high-performance transparent conducting films.* Chemical Communications, 2014. **50**(20): p. 2562-2564.

255. Xu, F. and Y. Zhu, *Highly conductive and stretchable silver nanowire conductors.* Advanced materials, 2012. **24**(37): p. 5117-5122.

256. Ahn, Y., et al., *Highly conductive and flexible silver nanowire-based microelectrodes on biocompatible hydrogel.* ACS applied materials & interfaces, 2014. **6**(21): p. 18401-18407.

257. Lee, D., et al., *High-performance flexible transparent conductive film based on graphene/AgNW/graphene sandwich structure.* Carbon, 2015. **81**: p. 439-446.

258. Sachse, C., et al., *ITO-Free, Small-Molecule Organic Solar Cells on Spray-Coated Copper-Nanowire-Based Transparent Electrodes.* Advanced Energy Materials, 2014. **4**(2).

259. Zhang, D., et al., *Synthesis of ultralong copper nanowires for high-performance transparent electrodes.* Journal of the American Chemical Society, 2012. **134**(35): p. 14283-14286.

260. Stewart, I.E., et al., *Solution-processed copper–nickel nanowire anodes for organic solar cells.* Nanoscale, 2014. **6**(11): p. 5980-5988.

261. Sun, Y., et al., *Ag nanowires coated with Ag/Pd alloy sheaths and their use as substrates for reversible absorption and desorption of hydrogen.* Journal of the American Chemical Society, 2004. **126**(19): p. 5940-5941.

262. Ahn, Y., et al., *Copper nanowire–graphene core–shell nanostructure for highly stable transparent conducting electrodes.* ACS nano, 2015. **9**(3): p. 3125-3133.

263. Hsu, P.-C., et al., *Passivation coating on electrospun copper nanofibers for stable transparent electrodes.* Acs Nano, 2012. **6**(6): p. 5150-5156.

264. Koleśnik, M.M., et al., *Resolving In Situ Specific-Contact, Current-Crowding, and Channel Resistivity in Nanowire Devices: A Case Study with Silver Nanowires.* Small, 2011. **7**(20): p. 2873-2877.

265. Graham, R.L., et al., *Resistivity dominated by surface scattering in sub-50 nm Cu wires.* Applied Physics Letters, 2010. **96**(4): p. 042116.

266. Critchley, K., et al., *Near-Bulk Conductivity of Gold Nanowires as Nanoscale Interconnects and the Role of Atomically Smooth Interface.* Advanced Materials, 2010. **22**(21): p. 2338-2342.

267. Asthana, A., et al., *In situ observation of size-scale effects on the mechanical properties of ZnO nanowires.* Nanotechnology, 2011. **22**(26): p. 265712.

268. Gall, K., J. Diao, and M.L. Dunn, *The strength of gold nanowires.* Nano Letters, 2004. **4**(12): p. 2431-2436.

269. Stan, G., et al., *Diameter-dependent radial and tangential elastic moduli of ZnO nanowires.* Nano Letters, 2007. **7**(12): p. 3691-3697.

270. Wu, B., A. Heidelberg, and J.J. Boland, *Mechanical properties of ultrahigh-strength gold nanowires.* Nature materials, 2005. **4**(7): p. 525.

271. Kim, H., S.A. Soper, and E.J. Podlaha-Murphy, *Pulse Electrodeposition of Multi-Segmented Super Invar/Au Nanowires.* ECS Transactions, 2013. **53**(11): p. 9-14.

272. Li, X., F. Gao, and Z. Gu, *Nanowire joining methods.* Open Surface Science Journal, 2011. **3**: p. 91-104.

273. Léonard, F. and A.A. Talin, *Electrical contacts to one-and two-dimensional nanomaterials.* Nature nanotechnology, 2011. **6**(12): p. 773.

274. Sourribes, M., et al., *Minimization of the contact resistance between InAs nanowires and metallic contacts.* Nanotechnology, 2013. **24**(4): p. 045703.

275. Lan, C., D.N. Zakharov, and R.G. Reifenberger, *Determining the optimal contact length for a metal/multiwalled carbon nanotube interconnect.* Applied Physics Letters, 2008. **92**(21): p. 213112.

276. Mohney, S., et al., *Measuring the specific contact resistance of contacts to semiconductor nanowires.* Solid-state electronics, 2005. **49**(2): p. 227-232.

277. Lan, C., et al., *Measurement of metal/carbon nanotube contact resistance by adjusting contact length using laser ablation.* Nanotechnology, 2008. **19**(12): p. 125703.

278. Walton, A., et al., *Four-probe electrical transport measurements on individual metallic nanowires.* Nanotechnology, 2007. **18**(6): p. 065204.

279. Helmenstine, A.M. *Table of Electrical Resistivity and Conductivity*. 2017 June 30 2017]; Available from: https://www.thoughtco.com/table-of-electrical-resistivity-conductivity-608499.

280. Bid, A., A. Bora, and A. Raychaudhuri, *Temperature dependence of the resistance of metallic nanowires of diameter⩾ 15 nm: Applicability of Bloch-Grüneisen theorem.* Physical Review B, 2006. **74**(3): p. 035426.

281. Chen, Y.-J., J.-H. Hsu, and H.-N. Lin, *Fabrication of metal nanowires by atomic force microscopy nanoscratching and lift-off process.* Nanotechnology, 2005. **16**(8): p. 1112.

282. Sambles, J., K. Elsom, and T. Preist, *The resistivity of thin wires.* Journal of Physics F: Metal Physics, 1982. **12**(6): p. 1169.

283. Xiang, C., et al., *Lithographically patterned nanowire electrodeposition: A method for patterning electrically continuous metal nanowires on dielectrics.* Acs Nano, 2008. **2**(9): p. 1939-1949.

284. Liao, L., et al., *The sensitivity of gas sensor based on single ZnO nanowire modulated by helium ion radiation.* Applied Physics Letters, 2007. **91**(17): p. 173110.

285. Choi, J. and J. Kim, *Highly sensitive hydrogen sensor based on suspended, functionalized single tungsten nanowire bridge.* Sensors and Actuators B: Chemical, 2009. **136**(1): p. 92-98.

286. Patolsky, F. and C.M. Lieber, *Nanowire nanosensors.* Materials today, 2005. **8**(4): p. 20-28.

287. Toriyama, T., Y. Tanimoto, and S. Sugiyama, *Single crystal silicon nano-wire piezoresistors for mechanical sensors.* Journal of microelectromechanical systems, 2002. **11**(5): p. 605-611.

288. Wang, Z., et al., *Nanowire-Based Sensors for Biological and Medical Applications.* IEEE transactions on nanobioscience, 2016. **15**(3): p. 186-199.

289. Tabasum, M.R., et al., *Magnetic Force Microscopy Characterization of Magnetic Nanowires and Nanotubes*, in *Magnetic Characterization Techniques for Nanomaterials*. 2017, Springer. p. 157-190.

290. González-Díaz, J.B., et al., *Enhanced Magneto-Optics and Size Effects in Ferromagnetic Nanowire Arrays.* Advanced Materials, 2007. **19**(18): p. 2643-2647.

291. Melle, S., et al., *Magneto-optical properties of nickel nanowire arrays.* Applied physics letters, 2003. **83**(22): p. 4547-4549.

292. Kuanr, B.K., et al., *Nonreciprocal microwave devices based on magnetic nanowires.* Applied Physics Letters, 2009. **94**(20): p. 202505.

293. Ramírez-Villegas, R., et al., *Configurable Microwave Filter for Signal Processing Based on Arrays of Bistable Magnetic Nanowires.* IEEE Transactions on Microwave Theory and Techniques, 2017. **65**(1): p. 72-77.

294. Parkin, S.S., M. Hayashi, and L. Thomas, *Magnetic domain-wall racetrack memory.* Science, 2008. **320**(5873): p. 190-194.

295. Parkin, S. and S.-H. Yang, *Memory on the racetrack.* Nature nanotechnology, 2015. **10**(3): p. 195-198.

296. Fernandes, A.C., et al., *Lab-on-chip cytometry based on magnetoresistive sensors for bacteria detection in milk.* Sensors, 2014. **14**(8): p. 15496-15524.

297. Li, S., et al., *Large, Tunable Magnetoresistance in Nonmagnetic III–V Nanowires.* Nano letters, 2015. **15**(12): p. 8026-8031.

298. Mourachkine, A., et al., *Template nanowires for spintronics applications: nanomagnet microwave resonators functioning in zero applied magnetic field.* Nano letters, 2008. **8**(11): p. 3683-3687.

299. Ivanov, Y.P., et al., *Tunable magnetic nanowires for biomedical and harsh environment applications.* Scientific reports, 2016. **6**: p. 24189.

300. Yassine, O., et al., *Isolation of cells for selective treatment and analysis using a magnetic microfluidic chip.* Biomicrofluidics, 2014. **8**(3): p. 034114.

301. Chong, Y.T., et al., *Multilayered core/shell nanowires displaying two distinct magnetic switching events.* Advanced Materials, 2010. **22**(22): p. 2435-2439.

302. Gül, Ö., et al., *Flux periodic magnetoconductance oscillations in GaAs/InAs core/shell nanowires.* Physical Review B, 2014. **89**(4): p. 045417.

303. Wang, J., et al., *Magnetic Fe 2 P nanowires and Fe 2 P@ C core@ shell nanocables.* Nano Research, 2010. **3**(3): p. 211-221.

304. Salazar-Alvarez, G., et al., *Tunable high-field magnetization in strongly exchange-coupled freestanding Co/CoO core/shell coaxial nanowires.* ACS applied materials & interfaces, 2016. **8**(34): p. 22477-22483.

305. Zhang, J., et al., *Nanoscale characterisation and magnetic properties of Co 81 Cu 19/Cu multilayer nanowires.* Journal of Materials Chemistry C, 2015. **3**(1): p. 85-93.

306. Da Col, S., et al., *Observation of Bloch-point domain walls in cylindrical magnetic nanowires.* Physical Review B, 2014. **89**(18): p. 180405.

307. Vila, L., et al., *Magnetic vortices in nanowires with transverse easy axis.* Physical Review B, 2009. **79**(17): p. 172410.

308. Bryan, M.T., et al., *Transverse and vortex domain wall structure in magnetic nanowires with uniaxial in-plane anisotropy.* Journal of Physics: Condensed Matter, 2011. **24**(2): p. 024205.

309. Rheem, Y., et al., *Electro-and magneto-transport properties of a single CoNi nanowire.* Nanotechnology, 2007. **18**(12): p. 125204.

310. Rheem, Y., et al., *Magnetotransport studies of a single nickel nanowire.* Nanotechnology, 2006. **18**(1): p. 015202.

311. Rheem, Y., et al., *Synthesis and magnetotransport studies of single nickel-rich NiFe nanowire.* Journal of Physics D: Applied Physics, 2007. **40**(23): p. 7267.

312. Grosz, A., M.J. Haji-Sheikh, and S.C. Mukhopadhyay, *High sensitivity magnetometers*. 2017: Springer.

313. Ai, Y. and S. Qian, *Electrokinetic particle translocation through a nanopore.* Physical Chemistry Chemical Physics, 2011. **13**(9): p. 4060-4071.

314. Liu, H., S. Qian, and H.H. Bau, *The effect of translocating cylindrical particles on the ionic current through a nanopore.* Biophysical journal, 2007. **92**(4): p. 1164-1177.

315. Qian, S., A. Wang, and J.K. Afonien, *Electrophoretic motion of a spherical particle in a converging–diverging nanotube.* Journal of colloid and interface science, 2006. **303**(2): p. 579-592.

316. Chen, L. and A. Conlisk, *DNA nanowire translocation phenomena in nanopores.* Biomedical microdevices, 2010. **12**(2): p. 235-245.

317. Hsu, J.-P., M.-H. Ku, and C.-Y. Kao, *Electrophoresis of a spherical particle along the axis of a cylindrical pore: effect of electroosmotic flow.* Journal of colloid and interface science, 2004. **276**(1): p. 248-254.

318. Qian, S. and S.W. Joo, *Analysis of self-electrophoretic motion of a spherical particle in a nanotube: effect of nonuniform surface charge density.* Langmuir, 2008. **24**(9): p. 4778-4784.

319. Hsu, J.-P., Z.-S. Chen, and S. Tseng, *Effect of electroosmotic flow on the electrophoresis of a membrane-coated sphere along the axis of a cylindrical pore.* The Journal of Physical Chemistry B, 2009. **113**(21): p. 7701-7708.

320. Guide, C.M.U.s., *Version 5.0-1. COMSOL, Inc., Burlington, Massachusetts, USA*. 2014.

321. Cannon Jr, D.M., et al., *Fabrication of single nanofluidic channels in poly (methylmethacrylate) films via focused-ion beam milling for use as molecular gates.* Applied physics letters, 2004. **85**(7): p. 1241-1243.

322. Rollings, R.C., D.S. McNabb, and J. Li, *DNA characterization with ion beam-sculpted silicon nitride nanopores.* Nanopore-Based Technology, 2012: p. 79-97.

323. Lan, W.-J., et al., *Pressure-driven nanoparticle transport across glass membranes containing a conical-shaped nanopore.* The Journal of Physical Chemistry C, 2011. **115**(38): p. 18445-18452.

324. Kawahara, K. and C. Tanford, *Viscosity and density of aqueous solutions of urea and guanidine hydrochloride.* Journal of Biological Chemistry, 1966. **241**(13): p. 3228-3232.

325. Stephanie, C.Y., et al., *Size-based molecular diagnostics using plasma DNA for noninvasive prenatal testing.* Proceedings of the National Academy of Sciences, 2014. **111**(23): p. 8583-8588.

326. Laszlo, A.H., et al., *Detection and mapping of 5-methylcytosine and 5-hydroxymethylcytosine with nanopore MspA.* Proceedings of the National Academy of Sciences, 2013. **110**(47): p. 18904-18909.

327. Shim, J., et al., *Detection and quantification of methylation in DNA using solid-state nanopores.* Scientific reports, 2013. **3**.

328. Kang, I., et al., *Designing DNA interstrand lock for locus-specific methylation detection in a nanopore.* Scientific reports, 2013. **3**.

329. Choi, Y., et al., *Dissecting single-molecule signal transduction in carbon nanotube circuits with protein engineering.* Nano letters, 2013. **13**(2): p. 625-631.

330. Cecchini, M.P., et al., *Rapid ultrasensitive single particle surface-enhanced raman spectroscopy using metallic nanopores.* Nano letters, 2013. **13**(10): p. 4602-4609.

331. Ying, Y.-L., C. Cao, and Y.-T. Long, *Single molecule analysis by biological nanopore sensors.* Analyst, 2014. **139**(16): p. 3826-3835.

332. Edel, J.B. and T. Albrecht, *Engineered nanopores for bioanalytical applications*. 2013: William Andrew.

333. Lee, M.-H., et al., *A low-noise solid-state nanopore platform based on a highly insulating substrate.* Scientific reports, 2014. **4**.

334. Plesa, C., et al., *Velocity of DNA during translocation through a solid-state nanopore.* Nano Lett, 2015. **15**(1): p. 732-737.

335. Yusko, E.C., et al., *Controlling protein translocation through nanopores with bio-inspired fluid walls.* Nature nanotechnology, 2011. **6**(4): p. 253-260.

336. Lan, W.-J., et al., *Effect of surface charge on the resistive pulse waveshape during particle translocation through glass nanopores.* 2014.

337. Kowalczyk, S.W., et al., *Slowing down DNA translocation through a nanopore in lithium chloride.* Nano letters, 2012. **12**(2): p. 1038-1044.

Vita

Mohammadsadegh Beheshti was born in Tehran, Iran. He obtained his B.S. degree from Iran University of Science and Technology in Mechanical Engineering in 2009. He acquired his M.S. degree from Iran University of Science and Technology in Mechanical Engineering in 2011. In Summer 2013 he joined Professor Sunggook Park's research group in the Mechanical Engineering Department in Louisiana State University. He received a Mechanical Engineering Department Scholarship in recognition of his outstanding academic achievements in January, 2014. He obtained his Graduate Certificate in Materials Science and Engineering in 2016. He is expected to earn the degree of Doctor of Philosophy in the Mechanical Engineering in May, 2018.